THE UNIVERSITY OF CHICAGO

DESIGN FROM DISORDER: VAPOR-DEPOSITED GLASSES, ORGANIC PHOTOVOLTAICS, AND NEGATIVE POISSON'S RATIO MATERIALS

A DISSERTATION SUBMITTED TO
THE FACULTY OF THE INSTITUTE FOR MOLECULAR ENGINEERING
IN CANDIDACY FOR THE DEGREE OF
DOCTOR OF PHILOSOPHY

BY
DANIEL ROBERT REID

CHICAGO, ILLINOIS
JUNE 2018

For my family

TABLE OF CONTENTS

LIST OF FIGURES

LIST OF TABLES

ACKNOWLEDGMENTS

No one completes a Ph.D. alone, and this Ph.D. is certainly no exception. First, I would like to thank my advisor, Juan de Pablo. Were I to take one message from all of my interactions with Juan, it would be that you should never be afraid to venture into a new field, no matter how unfamiliar. Upon entering the graduate program at The Institute for Molecular Engineering, I was under the naïve impression that a Ph.D. candidate more or less picks a topic and works on said topic for roughly five years. Juan quickly dispelling this misconception by introducing me to such disparate topics as organic photovoltaics and mechanical metamaterials. While this was daunting at first, Juan's relentless optimism and encouragement helped me to find my footing. As the years passed, Juan never ceased to both introduce me to new and fascinating topics, and to help me along in my active research topics. Juan's tireless work helped me, I believe, to become a well-rounded scientist, who, following Juan's example, is comfortable working in any number of areas. If the goal of a Ph.D. program is to put students in a position to find topics which genuinely interest them, Juan by all accounts has helped me succeed enormously in this regard. Juan's eagerness, clarity of thought, and skill in presentation will, I hope, continue to influence me as I progress as a scientist.

I would also like to thank the collaborator who I worked most closely with, Sidney Nagel. Though I mainly worked with Sid and his group designing metamaterials, his influence reached far beyond that. To be quite frank, I had never met someone who had taken more than a passing interest in coffee stains before I met Sid, and it was a bit baffling at first. Eventually, I began to appreciate how his keen interest in the finest of details often led to new understanding, and every once in a while, to something really exceptional. Sid, to me, is an example of the highest level of scientific integrity, running a no-nonsense operation where understanding is the true currency. Sid's thoughtful, intuitive way of working helped me to bring rigor and clarity to my work, which I appreciate greatly.

I would also like to thank two of the lab members who took an interest in guiding my work, and without whom things would simply have not gone as smoothly: Nicholas Jackson, and Ivan Lyubimov.

In my time at The University of Chicago I had the fortune to work and collaborate with many outstanding people, whose contributions, support, and friendship will be missed. Listed in no particular order: Alec Bowen, Lucas Antony, Josh Lequieu, Michael Webb, Daman Khaira, Grant Garner, Marat Andreev, Cody Bezik, Whitney Fowler, Jiyuan Li, Youngri Su, Su-mi Hur, Jian Qin, Arnout Boelens, Tyler Roberts, Weiwei Chu, Ye Zhou, Johnny Alfaro-Perez, Josh Moller, Emre Sevgen, Ashley Guo, Yamil Colón, Phil Rauschner, Viviana Palacio-Betancur Brian Keene, Gustavo Vasquez Montoyo, Kirk Swanson, Julian Helfferich, Nidhi Pashine, Hadi Rameziani Dakhel, Rui Zhang, Daniel Hexner, Thomas Videbaek, Mengfei He, Khá-Î Tô, Chloe Lindeman, Andrzej Latka, Irmgard Bischofberger, Matthew Goldey, Ryan Nieuwendaal, Chad Snyder, Dean DeLongchamp, Lee Richter, Alexander Bourque, and of course, John Otto and Thomas Kuntz.

Lastly I would like to thank my family for their support, counsel, and interest throughout this process.

ABSTRACT

In recent decades, simulation has become an indispensable element of materials design. The simulation of disordered materials presents unique challenges due to the large configuration space available and pathway dependence of material properties. In this dissertation, a wide variety of complex disordered materials are studied and designed. To begin, we explore disordered metamaterials, and create design rules for these materials to be tuned to show a negative Poisson's ratio. Such materials show promise in areas such as impact mitigation, filtration and as structural elements. These materials are anisotropic, however, meaning that their properties depend on the direction in which they are strained. We address this and other issues by introducing new optimization schemes which yield isotropic materials with Poisson's ratios approaching the lower mechanical limit. These optimized materials also show enhanced resistance to shear. We then transition to a study of highly stable glasses formed by a process of physical vapor deposition. Under particular conditions, physical vapor deposition of glass-forming molecules allows for films to be formed which are as stable as liquid-cooled glass films which have been aged for many years. However, a clear structural understanding of how these highly stable vapor-deposited glasses relate to their liquid-cooled counterparts is lacking. Here, we use a model glass-forming system to explore this problem. We then address two challenging topics in the area of organic photovoltaics: solution processing and solid-state film analysis. We introduce novel techniques to determine solubility in organic photovoltaic polymers, a necessary prerequisite for solution processing. The techniques allow for polymers to be rapidly designed and screened for solubility, and provides physical understanding of the origins of their solubility. Turning to solid-state film analysis, we introduce techniques to investigate interfacial properties of the ubiquitous bulk heterojunction, as well as microphase purity. Finally, we introduce a GPU-based molecular dynamics engine, DASH, which provides high performance and several new features within a flexible Python framework.

CHAPTER 1

INTRODUCTION

In Chapter 2 we investigate methods by which one can design materials with unusual mechanical properties such as a negative Poisson's ratio. Recent theoretical work suggests that systematic pruning of disordered networks consisting of nodes connected by springs can lead to materials that exhibit a host of unusual mechanical properties. In particular, global properties such as the Poisson's ratio or local responses related to deformation can be precisely altered. Tunable mechanical responses would be useful in areas ranging from impact mitigation to robotics and, more generally, for creation of metamaterials with engineered properties. However, experimental attempts to create auxetic materials based on pruning-based theoretical ideas have not been successful. Here we introduce a new and more realistic model of the networks, which incorporates angle-bending forces and the appropriate experimental boundary conditions. A sequential pruning strategy of select bonds in this model is then devised and implemented that enables engineering of specific mechanical behaviors upon deformation, both in the linear and non-linear regimes. In particular, it is shown that the Poisson's ratio can be tuned to arbitrary values. The model and concepts discussed here are validated by preparing physical realizations of the networks designed in this manner, which are produced by laser cutting two-dimensional sheets and are found to behave as predicted. Furthermore, by relying on optimization algorithms, we exploit the networks' susceptibility to tuning to design networks that posses a distribution of stiffer and more compliant bonds, and whose auxetic behavior is even greater than that of homogeneous networks. Taken together, the findings reported here serve to establish that pruned networks represent a promising platform for the creation of novel mechanical metamaterials.

While the materials developed in Chapter 2 are auxetic, they are also anisotropic, meaning that they show a negative Poisson's ratio when subject to deformations in certain directions, but not others. This property is in general not desirable. In Chapter 3, we build upon the

work in Chapter 2, designing materials which are not only more auxetic, but isotropic as well. In this work, we design in-silico isotropic auxetic structures derived from disordered networks which show Poisson's ratios as low as -0.98, are isotropic, and show a significantly enhanced shear modulus. The designed materials are successfully fabricated in experiment. The techniques demonstrated can be generalized to three dimensions. Using artificial neural networks, we identify unique structural features of these materials, shedding light on the complex structures which lead to auxetic behavior. This work provides theoretical and experimental design strategies for creating a new class of highly auxetic isotropic metamaterials.

In Chapter 4, we transition to a study of highly stable glass films. Glass films prepared by a process of physical vapor deposition have been shown to have thermodynamic and kinetic stability comparable to those of ordinary glasses aged for thousands of years. A central question in the study of vapor-deposited glasses, particularly in light of new knowledge regarding anisotropy in these materials, is whether the ultra-stable glassy films formed by vapor deposition are ever equivalent to those obtained by liquid cooling. We present a computational study of vapor deposition for a two-dimensional glass forming liquid using a methodology which closely mimics experiment. We find that for the model considered here, structures that arise in vapor-deposited materials are statistically identical to those observed in ordinary glasses, provided the two are compared at the same inherent structure energy. We also find that newly deposited hot molecules produce cascades of hot particles that propagate far into the film, possibly influencing the relaxation of the material.

In Chapter 5, we introduce a method for screening complex conjugated polymers for solubility. In organic semiconductors, solution-phase polymer structure and aggregation has a strong influence on device morphology and performance. Thus, understanding solubility of relevant polymers is crucial to the rational design new organic semiconductor materials and devices. Using a combination of atomistic molecular dynamics and free energy sampling

algorithms, we examine the aggregation behavior and solubility of the polymer PTB7, and study how polymer architecture can be modified to control aggregation. We demonstrate that free energy sampling can be used to effectively screen polymer solubility in a variety of solvents, but solubility parameters are not predictive. We then study the aggregation of several variants of PTB7 oligomers including those with linear (octyl), branched (2-ethylhexyl), and cleaved (methyl) side-chains, in a selection of explicit solvents and additives. Energetic analysis of these aggregates demonstrates that while sidechains do disrupt polymer backbone stacking, solvent exclusion is a critical factor controlling polymer solubility.

In Chapter 6, we develop NMR-informed simulation techniques for investigating organic electronics thin-film morphology. In organic electronics, robust relationships are needed between processing and structure. The development of such relationships is hindered by a dearth of materials characterization techniques which can study the structure of such materials at the molecular level. In this work, we introduce a technique which combines rotational-echo double-resonance NMR measurements with molecular simulation to develop a molecular-level understanding of organic electronic interfacial and microphase structure. The technique yields a one-to-one mapping between experimental measurements and simulated structures for metrics studied here. Using this technique, we examine the interfacial structure of the P3HT/PC61BM bulk heterojunction. In addition, we determine the free energy of phase separation of the P3HT/PC61BM blend, providing a powerful vehicle for understanding where devices lie in the thermodynamic landscape. Taken together, the techniques introduced here provide valuable tools for understanding complex microstructures, and can be applied to any material which can include atoms with a non-zero nuclear spin.

In Chapter 7, we introduce molecular simulation package which has proven instrumental in doing much of the previously described work. In recent years, a variety of particle simulation software packages have been developed, which are capable of simulating a wide range of atomistic and coarse-grained systems. With the advent of powerful graphics processing

units (GPUs), such software has been augmented to take advantage of this new hardware, leading to great acceleration of simulations. Here, we introduce DASH, a high-performance GPU-implemented molecular dynamics engine. DASH introduces several novel features, including efficient coupling to the free energy sampling package SSAGES, a highly efficient implementation of ring polymer molecular dynamics (RPMD) for capturing quantum nuclear effects, and a scheme for efficient and flexible runtime processing of data. The standard and unique feature sets of DASH combine to provide a valuable tool for scientific computational research.

CHAPTER 2

AUXETIC METAMATERIALS FROM DISORDERED NETWORKS

2.1 Introduction

When one stretches a material along one axis, intuition suggests that the material will contract in the orthogonal lateral directions. For most natural and synthetic materials, this intuition is confirmed by experiment. This behavior is quantified by the Poisson's ratio, ν, which for a deformed material is defined as the negative ratio of the material's lateral strain to its axial strain. In linear elastic theory for an isotropic sample, the Poisson's ratio is a monotonic function of the ratio of the material's shear modulus, G, to its bulk modulus, B. In two dimensions $\nu \to 1$ as $G/B \to 0$. In this limit, the material is 'incompressible', meaning that its volume does not change during this axial compression. In the limit $G/B \to \infty$, $\nu \to -1$. In the range where ν is negative, materials become wider as they are stretched, and thinner as they are compressed. Such materials, termed 'auxetics', show promise in applications that require structural elements[2, 3, 4], impact absorbers [5, 6], filters[7, 8], fabrics[9, 10], or other, tailor-made mechanical responses. Many auxetic materials are metamaterials, or materials constructed from building blocks with designed functionality. Metameterials represent a growing area of research in soft matter physics [11].

Auxetic materials have been formed through a variety of preparation protocols. Under special processing conditions, polymer foams and fibers, for example, can exhibit negative Poisson's ratios[12, 13, 14, 15, 5]. Auxetic foams, in particular, can be formed through a process of heating and sintering fine particles of ultra-high molecular weight polyethylene [12, 16], leading to structures of nodes connected by thin fibrils which collapse isotropically when compressed. Such structures are termed "re-entrant", and are a common motif in auxetic materials [12, 17]. When compressed uniaxially, these nodes and fibrils undergo

complex rearrangements that give rise to their auxetic behavior. As materials approach the lower limit of the Poisson's ratio, their hardness, or resistance to a small indentation, is predicted to increase rapidly[18]. This prediction is confirmed in the case of ultra-high molecular weight polyethylene, where the hardness of the auxetic material far exceeds that of a non-auxetic but otherwise equivalent foam [5].

The node and fibril structures common in auxetic polymer foams can be thought of as networks consisting of nodes connected by bonds. A central, common feature of past efforts to design auxetic materials in both theory and experiment, however, has been a reliance on regular, ordered lattices. Such lattices include the double arrowhead structure[19, 9], star honeycomb structures [20], re-entrant honeycombs[21, 22], and others[23]. Building on recent theoretical arguments[1, 24, 25], in this work we focus on disordered, random networks.

In the linear regime, the bulk modulus, B, or the shear modulus, G, of a network are proportional to the sum of the potential energies that are stored in each bond when the network is compressed or sheared. The decrease in B or G when the i^{th} bond is removed is denoted ΔB_i or ΔG_i, respectively. In a simple crystalline network, every bond responds in nearly the same manner to a global deformation. In contrast, in amorphous networks the response of individual bonds to a global deformation can span many orders of magnitude [1, 25].

Furthermore, there is little correlation between the value of ΔB_i and ΔG_i of a bond, i [25]. This suggests that, by selective removal or "pruning" of bonds with large or small values of ΔG_i or ΔB_i, the ratio G/B can be manipulated to reach a desired value; this would lead to disordered, "amorphous" materials with intriguing mechanical properties. Recent work has shown that similar pruning strategies could be used to design allosteric behavior into a network (where a deformation at a local source can produce a desired response at a distant target site). This behavior was demonstrated in experiments [26]. Creating auxetic materials, however, is more challenging and success in creating experimental prototypes has

been elusive. More specifically, simple models were used to design pruned networks with negative Poisson's ratio but, when prepared in the laboratory, they failed to exhibit auxetic behavior. This state of affairs has led to the question of whether pruning based approaches for design of auxetic materials are fundamentally flawed, or whether it is indeed possible to engineer truly auxetic laboratory materials by relying on more sophisticated models.

Here we address that question by introducing a mechanical model of disordered networks that incorporates the effects of angle-bending in a novel way. The model is minimally complex, and it is parameterized by comparison to experimental data for simple, random disordered networks. By adopting a pruning strategy that identifies and removes select bonds from these networks, it is shown that it is possible to reach Poisson's ratios as low as $\nu = -0.8$. The two-dimensional pruned networks designed in this manner are then prepared in the laboratory from rubber sheets that have been laser-cut according to the simulated models. They are found to behave as predicted. Structural analysis shows that highly auxetic networks are marked by an abundance of concave polygons. When networks are compressed uniaxially, these concave polygons shrink in all dimensions. Collectively, the local deformations of these concave polygons yield global auxetic behavior. These structures also give rise to a sub-linear stress-strain behavior, which is an important characteristic of impact-mitigating materials. We also investigate the effect of angle-bending stiffness, a parameter which plays a dominant role in ensuring agreement between simulation and experiment. This parameter also dramatically affects a materials' ability to be made auxetic, both in simulation and experiment. Networks comprised of bonds with angle-bending forces that are orders of magnitude weaker than those relevant to our experimental realizations can easily be tuned to show $\nu = -1$, while networks with much stiffer angle-bending forces cannot be tuned at all. Such changes are explained by the distributions and correlations of ΔG_i and ΔB_i. We conclude our discussion by designing highly auxetic materials through a materials optimization strategy. Specifically, by selectively manipulating the mechanical

characteristics of a few select bonds, it is shown that value of the Poisson's ratio can be further reduced from $\nu = -0.8$ to -0.9. The improved networks designed in this manner can then be successfully produced in the laboratory.

2.2 Models

2.2.1 Simulation Model

In order to have well-defined starting configurations, we base our networks on jammed packings of frictionless spheres at zero temperature[27]. We note however that the results are not necessarily confined to this choice of starting conditions. Spherical particles are initially placed at random positions within the simulation area. Particles i and j experience harmonic repulsions:

$$V(r_{ij}) = \frac{\epsilon}{2}(1 - \frac{r_{ij}}{\sigma_{ij}})^2 \Theta\left(1 - \frac{r_{ij}}{\sigma_{ij}}\right) \tag{2.1}$$

where r_{ij} is the center-to-center distance, σ_{ij} is the sum of the radii of particles i and j, and $\Theta(x)$ is the Heaviside step function. $\epsilon = 1$ sets the energy scale. The energy is minimized to produce zero-temperature, mechanically stable configurations. Particles are randomly assigned one of four evenly spaced radii (namely 0.6, 0.74, 0.87 and 1.0), leading to an amorphous packing when compressed isotropically. In all calculations, the contacts of particles which are in contact with fewer than three adjacent particles are not counted towards the total Z, as these would not contribute to the modulus of a jammed system. Such particles are removed before bonds are formed.

Two particles are considered to be in contact when $r_{ij} < \sigma_{ij}$. The average number of contacts or bonds per particle, Z, plays a central role in a host of network characteristics [27, 28, 29]. To set the value of Z, we create harmonic repulsive walls at the simulation box edges, whose positions are adjusted and the configuration relaxed until the required number

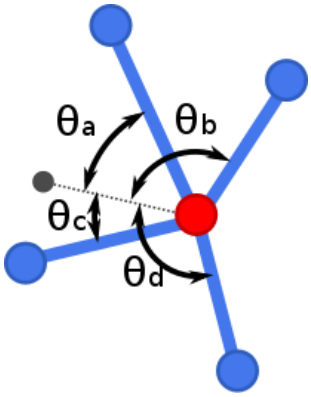

Figure 2.1: Schematic describing how angular restraints are applied for the node shown in red. A director, shown in grey, is attached to each node with a harmonic bond potential. Harmonic angles potentials are added between each pair of bonded nodes and the director, as indicated by the angles θ_{a-d}. The director is positioned such that θ_{a-d} are as far from 0° and 180° as possible. This scheme is applied at each node.

of particle contacts is achieved. Unstretched bonds of length r_{ij}^0 are then placed between the centers of pairs of contacting particles i and j and the soft-sphere potential is removed. The energy due to bond compression is thus:

$$V_c(r_{ij}) = \frac{1}{2r_{ij}^0}(r_{ij} - r_{ij}^0)^2 \ . \tag{2.2}$$

In order to include angle-bending constraints, we introduce a unit vector, $\vec{s}_i$, at each node i of the network, as shown in Figure 2.1. A bond connecting nodes i and j, makes an angle $\theta_{ji\vec{s}_i}$ with the vector $\vec{s}_i$. When the system is relaxed, this angle adopts its equilibrium value, $\theta^0_{hi\vec{s}_i}$. The energy cost to change an angle is quadratic:

$$V_b(\theta_{ij\vec{s}_i}) = \frac{k_{ang}}{2}(\theta_{ji\vec{s}_i} - \theta^0_{ji\vec{s}_i})^2 \tag{2.3}$$

where k_{ang} sets the energy scale for the angle-bending potential. During energy minimization, to obtain the ground state where the system is in mechanical equilibrium, the direction of $\vec{s}$ on each site is allowed to vary in order to minimize the total angular energy of a node. The coefficient k_{ang} is determined by comparing the response of model networks to those

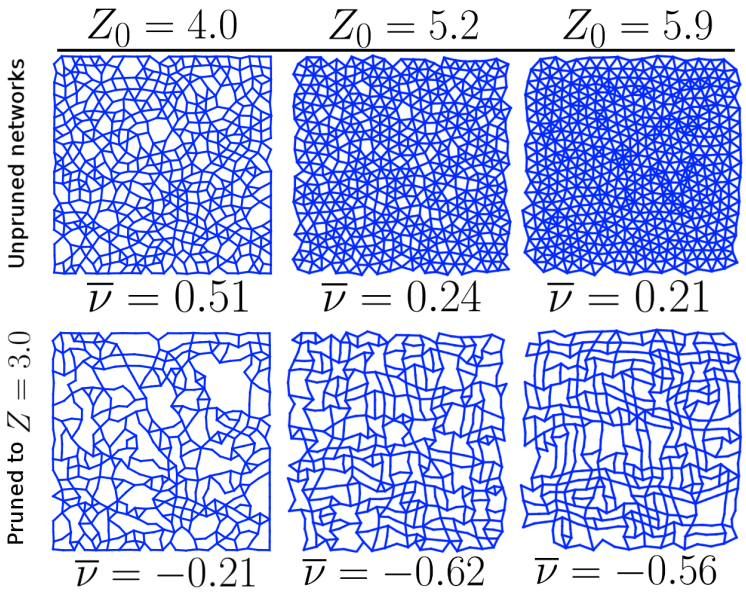

Figure 2.2: Examples of typical 500-node networks before and after pruning with $Z_0 = 4.0, 5.2, 5.9$. The top row shows unpruned networks, while the bottom row shows networks which have been pruned to $Z = 3.0$. Unpruned networks show decreasing ν as Z_0 increases while pruned networks show a minimum ν at $Z_0 = 5.2$. This minimum ν at $Z_0 = 5.2$ corresponds to a high fraction of re-entrant nodes which can collapse inwards as the system is compressed.

prepared in experiments and depends on the material and shape of the bonds, as described in Methods.

The total energy of a network under stress is the sum of two terms: a compressive component given by Eq. 2.2 and a bending component, given by Eq. 2.3. Note that the compressive strength is scaled by $1/r_{ij}^0$ as would occur in a physical mechanical strut of constant thickness.

Figure 2.2 shows representative realizations of two-dimensional disordered networks consisting of nodes connected by bonds, before and after pruning.

In two dimensions, there are two independent shear moduli - one associated with simple shear and one with pure shear. The modulus associated with simple shear influences the value of ν that is measured when the material is deformed by pulling or pushing from opposite

corners. The modulus associated with pure shear relates to the value of ν measured when the material is uniaxially compressed or expanded in x or y, as shown in Appendix. In this study we focus primarily on algorithms that only influence the modulus associated with pure shear since this can be more easily measured in our experiments. However we also show that isotropic auxetic networks can be created using similar algorithms as discussed in detail in Appendix. Such materials are auxetic with respect to any uniaxial deformation. G and B are measured as described in Methods.

2.3 Results

2.3.1 Bond Response Distributions

In an amorphous network the distributions of ΔB_i and ΔG_i, $P(\Delta B_i)$ and $P(\Delta G_i)$ can span many orders of magnitude. That is, when some bonds are removed, G or B may decrease significantly, while when others are removed, there may only be a negligible decrease. Our pruning procedure targets bonds that contribute little to the shear modulus but contributing strongly to the bulk modulus. It is therefore important that $P(\Delta B_i)$ and $P(\Delta G_i)$ be broad and extend to small values [1, 25].

A second crucial condition for successful pruning is that ΔB_i and ΔG_i be uncorrelated. Based on these two features, one can selectively remove bonds from a disordered network in order to drive B, G, and thus ν, to a desired target value [1, 24].

Panels a) and b) of Fig. 2.3 show the probability distributions $P(\Delta B_i)$ and $P(\Delta G_i)$ for unpruned networks. Results are shown for networks with Z_0 (Z of the network before pruning) between 4.0 and 5.9, with $k_{ang} = 0.01$. The value of k_{ang} is set as the value which best reproduces the deformation observed in experiment, as described in Methods. As Z_0 increases, both $P(\Delta B_i)$ and $P(\Delta G_i)$ become narrower. This suggests that networks with

lower coordination numbers are more amenable to pruning. A peak in $P(\Delta B_i)$ becomes apparent for $Z_0 = 5.9$.

In order to facilitate effective pruning, bond response distributions must not only be broad, but uncorrelated. Panel (c) of Fig. 2.3 shows the Pearson correlation coefficient for ΔG_i and ΔB_i across a range of Z_0 values. While distributions are significantly uncorrelated between $Z_0 = 4.0$ and 5.2, the level of correlation increases thereafter. As we will see, networks pruned from $Z_0 = 5.2$ lead to the lowest value of ν.

2.3.2 Pruning

For the iterative pruning strategy adopted here, at each iteration the lowest ΔG_i bond is removed. Given the low correlation between ΔG_i and ΔB_i, pruning the lowest ΔG_i bonds tends to increase G/B and decrease ν. At each iteration, ΔG for a bond is measured by performing a trial removal of that bond, and by measuring the resulting shear modulus, thereby resulting in n_{bond} measurements of G. Each measurement of G requires on the order of seconds or minutes of CPU time, depending on network size - creating a large auxetic network can therefore be computationally demanding. The calculation of ΔG_i can be parallelized with one core per ΔG_i measurement. We use the parallel workflow management software Swift/T to parallelize this process across several hundred CPU cores, thereby accelerating network creation [30].

Fig. 2.4 shows Poisson's ratios, ν, for networks having different values of Z_0. Each data set represents an average of 50 independent pruned networks of 500 nodes each.

The Poisson's ratio is determined by introducing a small strain of magnitude $\epsilon_y = 1 \times 10^{-4}$ in the y dimension of the network, allowing the system to relax to an average force tolerance of 1×10^{-13}, and then measuring the resulting lateral deformation. Note that while simple bead-spring networks (those ignoring angle bending) lose rigidity below $Z = 4$, the angular

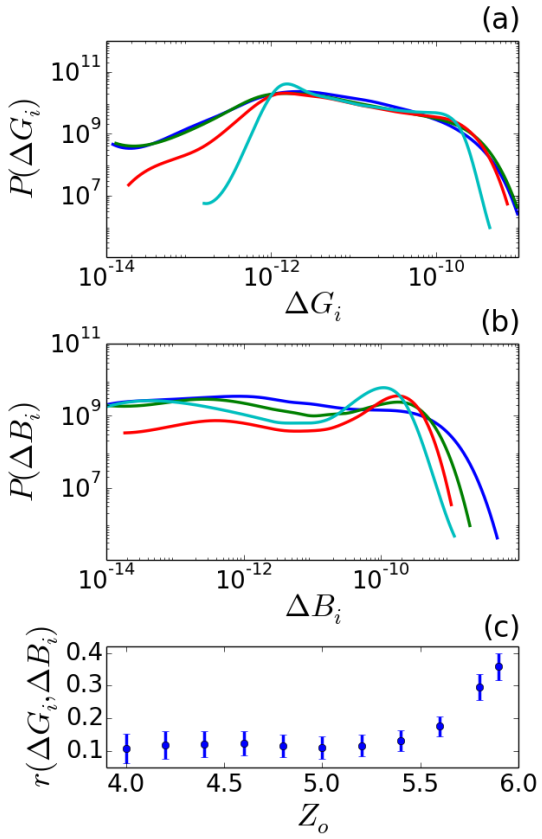

Figure 2.3: Probability distributions and correlations of ΔG_i and ΔB_i for unpruned 500-node networks with different Z_0. Panel (a) shows probability distributions of ΔG_i, while Panel (b) shows those for ΔB_i. Strains for both deformations are $\epsilon_y = 1 \times 10^{-4}$. Data sets as ($Z$, color) are (4.0, blue), (4.8, green), (5.2, red), and (5.9, cyan). Each data set is taken from 100 independent 500 node networks. The bond bending strength is $k_{ang} = 0.01$, a value which is experimentally realizable. As the coordination number increases, distributions narrow significantly, reducing networks' propensity to be pruned. Panel (c) shows the correlation between ΔG_i and ΔB_i for networks over a range of initial Z values. Standard deviation of r values across 100 independent configurations are shown.

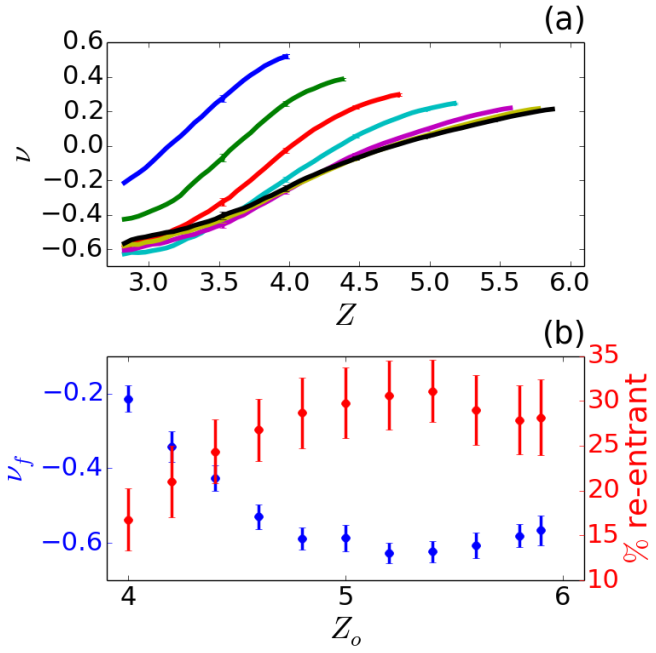

Figure 2.4: Poisson's ratios resulting from pruning 500-node networks with different values of Z_0 shown in (a) with resulting structural and mechanical properties shown in (b). Data are taken from 50 independent 500 node networks. In (a), ninety-five percent confidence intervals are shown. To prune, we remove the lowest ΔG bond at each iteration. Networks are pruned until $Z = 2.8$, at which point they become so sparse that ν fluctuates wildly with further pruning. In (b), the blue data set shows the Poisson's ratio reached at $Z = 3.0$ with respect to Z_0, with 95% confidence intervals shown. A minimum ν is observed at $Z_0 = 5.2$. Plotted in red is the fraction of nodes which are classified as re-entrant. The data shows that the most auxetic networks show the greatest degree of re-entrant behavior, suggesting a structural origin to ν.

restraints in the model introduced here lead to rigid networks to a much lower values of Z . As discussed below, $\epsilon_y = 1 \times 10^{-4}$ is well within the linear regime.

Several interesting features are apparent in the pruning progression shown in Fig. 2.4. First, even before there is any pruning, the Poisson's ratio of the networks decreases from 0.51 at $Z_0 = 4.0$ to 0.21 at $Z_0 = 5.9$, revealing a wide variation of $\Delta\nu = 0.3$. A decrease in ν with increasing coordination has been observed previously in network systems[31]. Second, the initial slope of the Poisson's ratio curve as a function of pruning decreases from $d\nu/dZ = 0.47$ to 0.14 between $Z_0 = 4.0$ and $Z_0 = 5.9$ (as calculated by the average slope over the first

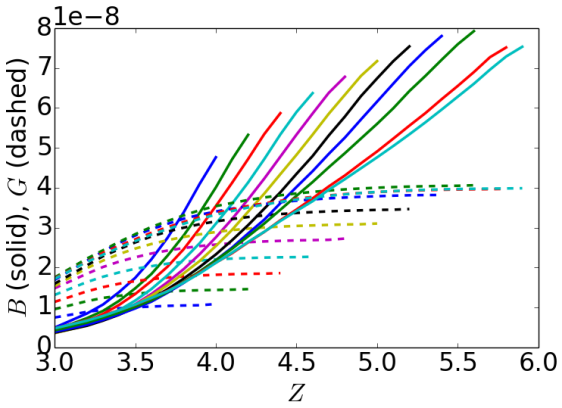

Figure 2.5: Bulk and shear moduli of networks as low ΔG bonds are pruned. Initially, the bulk moduli decrease while the shear moduli remain constant, resulting in the increasing magnitude of the slope of ν observed in Fig. 2.4. After significant pruning, G begins to decrease. Near $Z = 3.0$, G/B plateaus and ν reaches its minimum.

$\Delta Z = 0.1$ pruning). The smaller value of $d\nu/dZ$ at higher Z_0 is consistent with the narrower distribution functions and higher correlations observed, as shown in Fig. 2.3. However, a higher Z_0 also implies that there are simply more bonds available for pruning. These factors conspire to produce the lowest pruned networks when $Z_0 = 5.2$. This also corresponds to the highest Z_0 before the correlation of ΔG_i and ΔB_i begins to increase, as seen in Fig. 2.3c. Networks with $Z_0 = 5.2$ show a minimum average of $\nu = -0.62$. The lowest ν value achieved for an individual network, however, is $\nu = -0.79$.

To explore further how ν changes with pruning, we examine G and B of networks as they are pruned, as shown in Fig. 2.5. In two dimensions, linear elastic theory states $\nu = (1 - G/B)/(1 + G/B)$. By pruning the lowest ΔG bonds, our aim is to maintain a high value of G while reducing B. During pruning, initially B drops and G remains nearly constant, resulting in the steepening slope of ν seen in Fig. 2.4. At some value of Z along the pruning process, G begins to decrease more rapidly, and the slope of ν decreases in magnitude until ν reaches its minimum. This accelerated decrease of G can be attributed to the fact that few low ΔG_i bonds remain once pruning has progressed sufficiently.

2.3.3 Structural features

Fully pruned networks ($Z = 3.0$) show a range of ν values that depends on their corresponding Z_0, suggesting that there exist underlying structural differences between these pruned networks. Fig. 2.2 shows representative networks with $Z_0 = 4.0, 5.2, 5.9$ before and after pruning to $Z = 3.0$. One can appreciate that these structures are in fact quite different from each other, despite having similar numbers of nodes and bonds. To quantify these structural differences, we calculate the percent of nodes which are "re-entrant" in pruned networks, as shown in Panel (b) of Fig. 2.4. Here, a re-entrant node is defined as one having an angle between adjacent bonds that is greater than 180°. As can be seen in Fig. 2.2, re-entrant nodes manifest as concave angles in polygons within the network. Such polygons tend to collapse inwards at re-entrant nodes when compressed. A sufficient number of such polygons could lead to globally auxetic behavior. As can be seen in Fig. 2.4 (b), more auxetic networks exhibit a higher percentage of re-entrant nodes. This structural motif therefore provides a basis for design of amorphous or otherwise disordered networks that are auxetic and isotropic. In this calculation we did not classify nodes with only two bonds as re-entrant, though we arrive at qualitatively the same conclusions if they are included.

2.3.4 Experimental validation

Experimental pruned networks are made out of laser-cut sheets of rubber[26] as described in Methods. The strength of bond bending, k_{ang} in simulation, is modified by controlling the thickness of the bonds at the point where they attach to the nodes as well as their aspect ratio as seen in the inset to Fig. 2.6. We focus on the bond shape shown in that figure. The deformation of such networks can be described quantitatively by our model with the value $k_{ang} = 9 \times 10^{-3}$, which we use for all networks comprised of bonds of this shape. We uniaxially compress three independent networks with $Z_0 = 5.2$ pruned to $Z = 3.0$ and measure ν in both simulation and experiment as shown in Fig. 2.6. At low strains, networks are strongly auxetic, however ν increases monotonically with increasing strain.

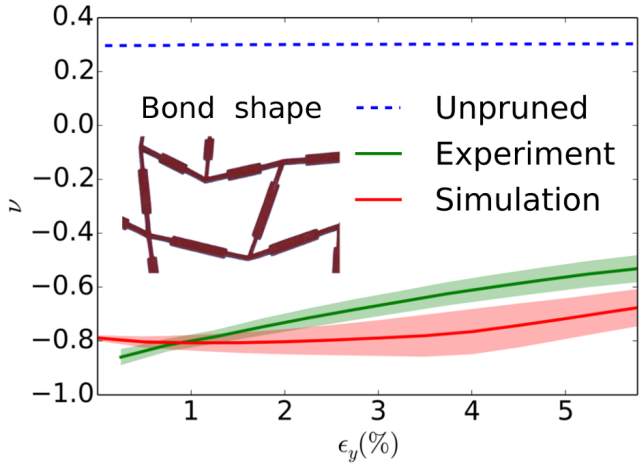

Figure 2.6: Poisson's ratios from simulation and experiment for pruned and unpruned networks. Shown in green and red is ν with uniaxial strain from three different networks pruned to $Z = 3.0$ from $Z_0 = 5.2$. The solid lines represent the average ν for the three configurations and the shaded areas represent standard deviations. The dashed blue line shows ν for unpruned networks in simulation at low strain. A value of $k_{ang} = 9 \times 10^{-3}$ in simulation is fit to match this experimental bond shape, shown in the Figure. This k_{ang} fits well for all networks which use this bond shape. A section of an experimental network is shown as an example of the individual bond shape used.

We now examine the response of a particular network formed with $k_{ang} = 9 \times 10^{-3}$. Panel (a) of Fig. 2.7 shows a network compressed with $\epsilon_y = 0.09$. The shape of the uncompressed network is shown in gray, serving to demonstrate its auxetic response. Panel (b) directly compares experimental and simulated configurations at $\epsilon_y = 2\%$. The experimental configuration is shown in red, and the simulated configuration is shown in blue. At this strain, experiment and simulation are in good agreement. Note that the network pictured in Panel b is isotropic, and will be auxetic with respect to any strain. Using pruning methods discussed in the Appendix, we achieve $\nu = -0.25$ for this network. For higher strains, our simulations are no longer able to accurately predict node positions, as they do not describe the behavior of physical bonds and nodes when they collide. However, Despite this shortcoming, the trends of ν with ϵ_y are captured well by our model, as shown in Fig. 2.6.

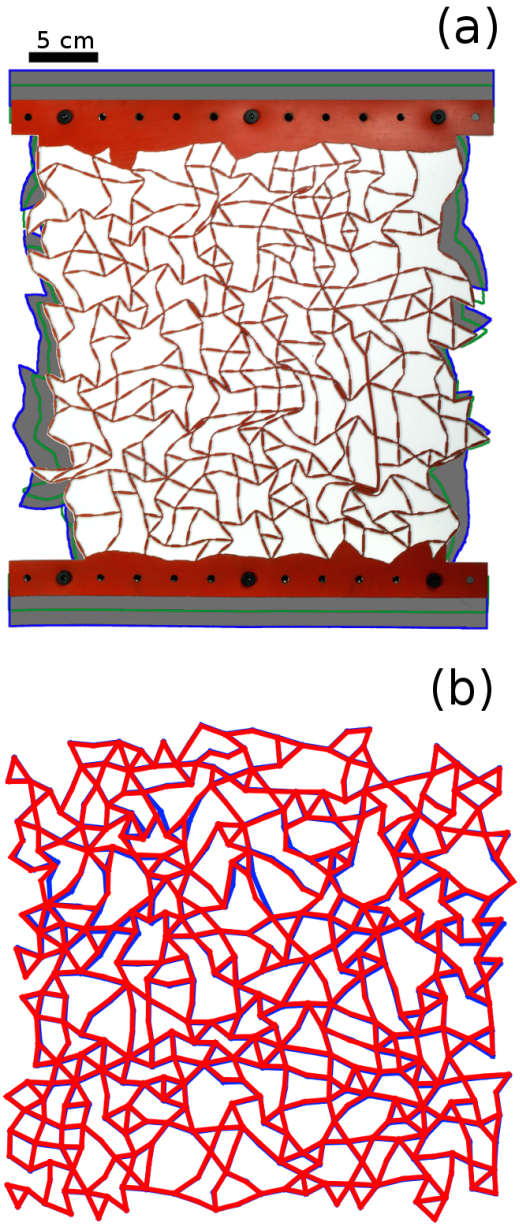

Figure 2.7: A compressed 500-node experimental network with comparison to simulation. Panel (a) shows a compressed experimental network at a strain of $\epsilon_y = 9\%$. The gray shaded region indicates the shape of the uncompressed network, and the green outline represents the shape at $\epsilon_y = 5\%$. Panel (b) compares an experimental configuration with that predicted from simulation at $\epsilon_y = 2\%$. Note that this network is isotropic and will be auxetic with respect to any uniaxial strain, which is distinct from the other networks in this work. It shows $\nu = -0.25$ for deformations up to $\epsilon_y = 4\%$. In red is shown a rendering of the experimental configuration and in blue is shown the simulated configuration at the same strain.

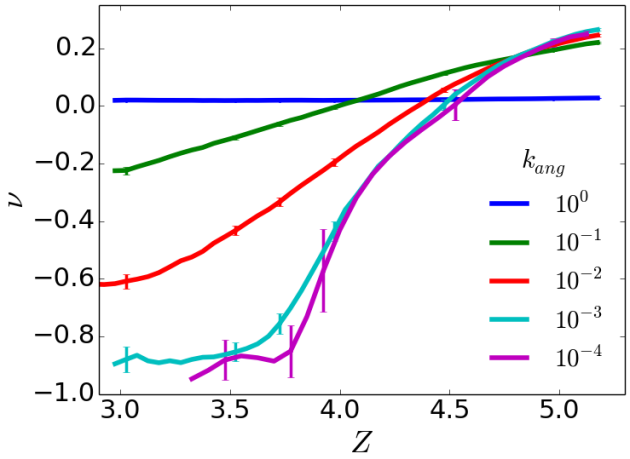

Figure 2.8: Poisson's ratios resulting from pruning 500 node networks with $Z_0 = 5.2$ and k_{ang} values which range from 10^{-4} to 10^0. With larger k_{ang}, pruning becomes less effective due to narrower ranges of ΔG_i and ΔB_i and increased correlations between the two quantities. In the lower limit, ν approaches -1.0 as predicted in previous work[1].

2.3.5 Angle bending stiffness

We have focused only on values of k_{ang} within a relatively narrow range, but one could conceive of specially designed experimental realizations which would span a much wider range. This is of interest because networks with greater bond stiffness can withstand greater strains before failing. As such, we turn our attention to the effect that a wide range of bond bending stiffness has on ν. We study networks with $Z_0 = 5.2$, which yielded the lowest value of ν for $k_{ang} = 0.01$. Fig. 2.8 shows ν resulting from low ΔG pruning of 500-node networks with values of k_{ang} that span five orders of magnitude, from 10^{-4} to 10^0. Consistent with previous work [1], $\nu \to -1$ as $k_{ang} \to 0$ in fully pruned networks. Consistent with these results, we find that as k_{ang} becomes smaller, bond response distributions become wider and are more easily modified by pruning, as shown in Figure 2.10.

2.3.6 Physical insights from model improvement

Three features distinguish the model used in this work from that of previous attempts: (i) the use of finite rather than periodic simulations, (ii) the use of fixed boundary conditions

as employed in experiment, and (iii) most importantly the addition of an angle-bending potential. To demonstrate the importance of the angle-bending term, we study a network which has been pruned to $\nu = -0.96$ at $Z = 3.9$ with an extremely low angle-bending stiffness of $k_{ang} = 10^{-4}$. Increasing k_{ang} to $k_{ang} = 10^{-2}$ increases the Poisson's ratio to $\nu = -0.36$. Increasing k_{ang} past this experimentally determined value to $k_{ang} = 1$ increases ν to 0.0, as shown in Figure 2.17. By picking a value of k_{ang} which does not correspond to the experimental realization, predictions from the simulation would be inaccurate.

Our results suggest that weaker angle-bending forces allow for more dramatic deformations of the concave polygons present in these networks. Assigning a larger k_{ang} penalizes these deformations, which increases ν. Therefore to create auxetic experimental realization of networks, care should be taken to minimize the effect of angle-bending forces.

2.3.7 Stress-strain behavior

For a variety of impact-mitigation applications, it is of interest to develop materials that display a relatively constant stress-strain behavior. Such materials can absorb more energy while maintaining lower applied forces, and thus reduce the possibility of damage. As shown in Figure 2.12, pruned networks display nearly constant stress past 3% strain. At such strains, linear response calculations are no longer accurate, as shown in Figure 2.11. We find that the linear response framework applies well until roughly 1% strain.

2.3.8 Bond strength optimization

Up to this point, we have relied on homogeneous materials, with identical bonds, for all calculations and experiments. In what follows, we modify the strength of individual bonds as a means for decreasing ν in networks composed of bonds with different stiffnesses. This process can be mimicked in experiment by modifying the thickness or material of a given bond. We implement a simple optimization algorithm that iteratively strengthens the bond

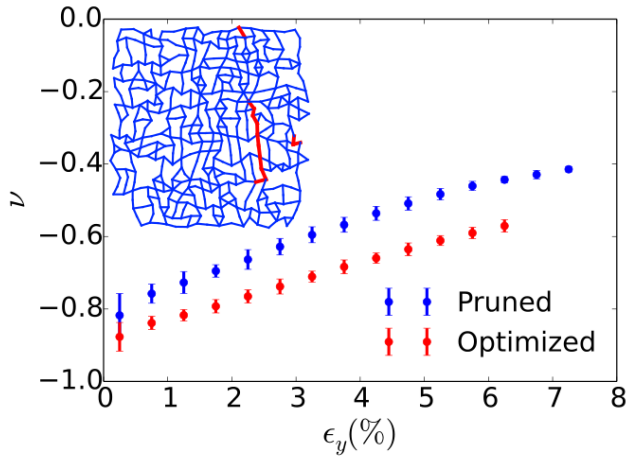

Figure 2.9: Experimentally measured ν for an ordinary pruned network and an otherwise identical network in which several of the bonds have been strengthened. Error bars show 2.5σ. The bonds which were strengthened were chosen in simulation in order to reduce ν. In simulation, the networks with regular and strengthened bonds were predicted to show $\nu = 0.79, 0.91$ respectively at small strains. The inset network configuration shows in red, bonds which were strengthened in experiment and in blue, unstrengthened bonds

leading to the greatest decrease in ν, as described in the Appendix. Both the compressive and bending modulus of a particular bond are increased when a bond is strengthened. We examine a particular network with $k_{ang} = 10^{-2}$ and $\nu = -0.79$. By successively strengthening individual bonds in this network, we further decrease ν from -0.79 to -0.91 in simulation. Interestingly, after 430 iterations with 649 total bonds in the network (where one bond in strengthened by 10% at each iteration), 94% of the bonds remained untouched, while a select few, 1.8%, are strengthened to more than five times their original strength, leading to an essentially bimodal distribution of bond strengths. These strengthened bonds are almost all connected as shown in the inset of Fig. 2.9.

To validate the predictions of our simulations, we also prepared an experimental realization of this optimized network. For simplicity, bonds strengthened by a factor of five or greater were made thicker, and others were left unchanged. The corresponding experimental values of ν are shown in Fig. 2.9, showing a decrease in ν of 0.059 at $\epsilon_y = 0.25\%$ and a decrease

of 0.11 at $\epsilon_y = 2.75\%$, in good agreement with predictions. Importantly, these optimized materials with a few significantly stronger bonds lend themselves to additive manufacturing. In such realizations, some bonds could be constructed of highly rigid materials, while the remainder would be more pliable, and more advanced optimization algorithms could readily be applied to this problem.

2.4 Conclusion

In summary, we have established that it is possible to create designer auxetic materials from amorphous networks. The pruning strategy that we have proposed does not depend on the initial configuration but rather relies on measuring aspects of local response to a globally applied deformation. As such, it may apply more generally to networks based on a variety of initial preparation protocols and not just those based on jamming. The models and concepts introduced in this work have been validated through a concerted program of design, computation and laboratory experimentation. Amorphous networks are shown to offer a number of control parameters that can be tuned to achieve particular mechanical responses. It is found, for example, that a networks' propensity to be made auxetic depends on both the network's original coordination number, as well as the relative resistance to angle bending. More pliable networks yield the lowest Poisson's ratios due to their wide bond response distribution and their low response correlation. Stiffer networks are less amenable to pruning, and only show limited changes of their Poisson's ratio through pruning. By relying on bond-strength optimization schemes, however, it is possible to alter the Poisson's ratio of networks with stiff bonds considerably, thereby providing a strategy to alter not only how auxetic a material is, but also its intrinsic stiffness. While the results presented here have been limited to two-dimensional networks, the concepts and strategies proposed should be equally applicable to three dimensions, where we can use 3D printing to realize our computer models. We therefore anticipate that these networks could be potentially useful for applications involving additive manufacturing. Using appropriately designed nanoparticles,

it is also conceivable that one could form auxetic materials through a self-assembly process.

2.5 Methods

2.5.1 Simulation Methods

Simulated networks are generated as described in the Models section. A harmonic wall coefficient of 2.0 is used to compress particles. To measure ν, $\epsilon_y = 1 \times 10^{-4}$ is applied and the transverse strain of nodes at the left and right edges of the network is measured. Bulk properties are measured by applying uniform compressions of 1×10^{-4}. Shear properties are measured with $\epsilon_x = -1 \times 10^{-4}$ and $\epsilon_y = 1 \times 10^{-4}$ or $\gamma = 1 \times 10^{-4}$, for pure and simple shear, respectively. The average force is relaxed to 1×10^{-13} for all measurements. To mimic experiment, particles along the top and bottom edges of networks are restrained in the x dimension. The coefficient to describe bond bending, k_{ang} is fit by determining the value of k_{ang} which minimized mean square distance between nodes in between uniaxially strained experimental and simulated networks at $\epsilon_y = 3\%$. The same k_{ang} value is used to describe each class of experimental bonds.

2.5.2 Experimental Methods

Experimental networks are constructed out of laser-cut silicone rubber sheets with a Shore value of $A70$ and a thickness of 1.5 mm as described in previous work [26]. We can vary the relative resistance to angle bending (which is quantified by k_{ang} in our simulation model), by narrowing or widening a section of the bond near the node (see Fig. 2.6). To facilitate measurement, nodes at the top and bottom of the network are fused into a solid rubber piece, as shown in Panel (a) of Fig. 2.7. The Poisson's ratio is determined by applying a uniaxial compression in the y direction and measuring the resulting lateral strain.

2.6 Appendix

2.6.1 Bond response distributions with bending stiffness

The effect of angle-bending stiffness can be appreciated by examining the bond response distributions when k_{ang} is varied from 10^{-4} to 10^{0}, as shown in Figure 2.10. Dashed lines denote the distributions of unpruned networks with $Z_0 = 5.2$. As angles become stiffer, the distribution of bond responses narrows significantly. As mentioned in the main text, broader distributions enable more effective pruning. The solid lines of Figure 2.10 show the bond response distributions for the same networks after pruning to $Z = 3.5$. Not only do stiffer bonds lead to narrower distributions - they also make these distributions more difficult to modify through pruning. For the stiffest angles considered here, $k_{ang} = 10^{0}$, no significant change is observed in the corresponding distributions, and little change occurs in ν. A angles become easier to deform (more compliant), the change in distributions becomes more dramatic. Correlations between bond responses ΔG_i and ΔB_i decrease significantly, leading to larger changes in ν. We calculate the Pearson correlation coefficient for unpruned networks to be 0.134, 0.125, and 0.843 for $k_{ang} = 10^{-4}$, 10^{-2}, and 10^{0}, respectively. The lower the correlation, the more tunable the network becomes.

2.6.2 Non-linear behavior

While a host of properties are readily accessible through linear-response calculations, the corresponding predictions are not valid for large deformations. To address the extent of linear response, we compare in Figure 2.11 the node positions of systems strained along the y-direction - as predicted by linear-regime calculations - to those predicted by the true network-dynamics formalism adopted here. We quantify the relative error between the two predictions through the average of $100 * |\vec{r}_{md} - \vec{r}_{lin}|/|\vec{r}_{md}|$, where $\vec{r}_{md}$ is the calculated displacement of a node and $\vec{r}_{lin}$ is the displacement of a node within the linear regime scaled to the strain of interest. The linear-regime responses are calculated at $\epsilon_y = 0.1\%$. We average

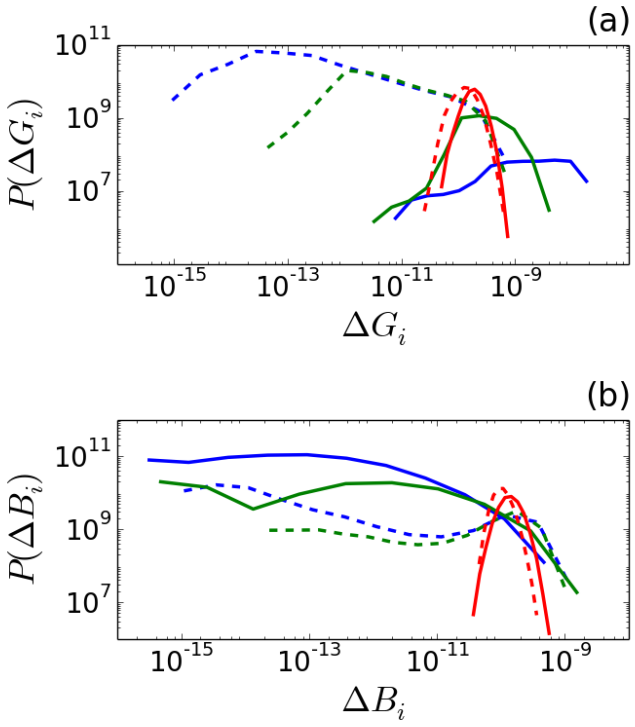

Figure 2.10: Distributions of ΔG_i, ΔB_i for networks before pruning ($Z = 5.2$) and after pruning ($Z = 3.5$) of networks with different values of k_{ang}. Distributions are shown for $k_{ang} = 10^{-4}$ (blue), 10^{-2} (green), 10^{0} (red). Distributions for unpruned networks are shown with dashed lines, while those for pruned networks are shown with solid lines. As k_{ang} decreases, the change in distributions becomes more significant, corresponding to the greater change in ν with pruning as seen in Figure 8 of the main text.

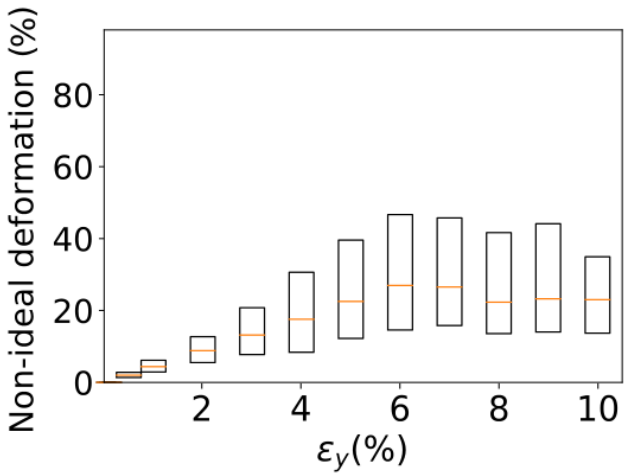

Figure 2.11: Relative error of between node displacements as predicted by molecular dynamics and linear regime calculations with uniaxial strain. Relative error is calculated as $100 * |\vec{r}_{md} - \vec{r}_{lin}|/|\vec{r}_{md}|$. Red lines denote the medians of samples, box edges denote the 25^{th} and 75^{th} percentile.

this quantity across every node in three distinct 500-node networks with $Z = 3.0$ pruned from $Z_0 = 5.2$. The relative error increases nearly linearly from roughly 0% at $\epsilon_y = 0.5\%$ to a median of 30% at $\epsilon_y = 5\%$. Note, however, that the relative error of individual nodes can exceed 800%. From this data, one can assess to what degree linear regime predictions can be considered accurate over a range of strains.

2.6.3 Stress-strain behavior

For a variety of impact-mitigation applications, it is of interest to develop materials that display a relatively constant stress-strain behavior. Such materials can absorb more energy while transmitting less force, and thus reduce the possibility of damage. Figure 2.12 shows the stress-strain behavior of networks before and after pruning. Unpruned networks show typical linear stress versus strain behavior. Pruned networks, however, behave sub-linearly, and exhibit a nearly constant stress past 3% strain. This behavior is characteristic of a material undergoing complex rearrangements, such as collapsing concave structures. Also shown is an extrapolation of the linear-regime behavior for pruned networks, demonstrating

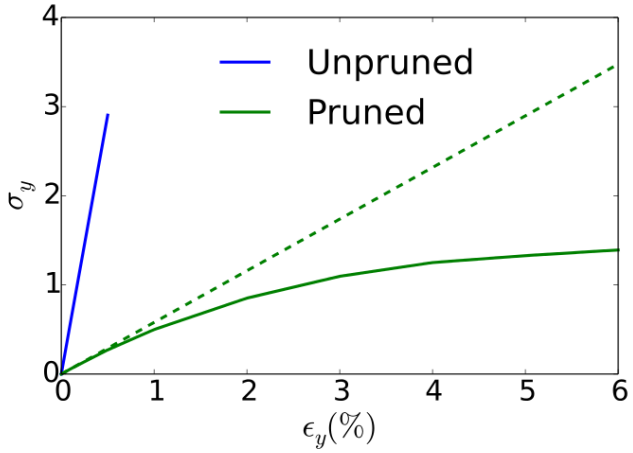

Figure 2.12: Stress-strain curve for unpruned ($Z = 5.2$) and pruned ($Z = 3.0$) networks. The dashed green line shows an extrapolation of the pruned networks' linear regime behavior. Error bars are smaller than the size of the line. The unpruned network stress behaves linearly with strain, as is expected from a network which employs harmonic constraints. The pruned network, however, behaves sublinearly, as is characteristic of a material undergoing complex rearrangements.

the degree of sublinearity.

2.6.4 Isotropic and anisotropic networks

In the main text, we discuss the two relevant shear moduli - those associated with pure and simple shear. We denote these moduli G_p and G_s, respectively. Here we show that networks pruned only to have high G_p/B do not have high G_s/B, and vice versa. In practice, this means that a network pruned to be auxetic when pulled in a direction normal to its edges will not be auxetic if pulled outwards from its corners. We also examine isotropic networks - those which have been pruned to show low $(G_p + G_s)/B$. Isotropic networks are formed by iteratively pruning the minimum $\Delta G_p + \Delta G_s$ bond.

In what follows, we examine what happens when unpruned, low ΔG_p pruned, low ΔG_s pruned and low $\Delta G_p + \Delta_s$ pruned (isotropic) networks are deformed by stretching the materials in a direction normal to their edges and by stretching along a diagonal. Figure

2.13 shows an unpruned network deformed by pulling from the edges and corners (along a diagonal) in Panels a and b, respectively. The gray background shows the outline of the undeformed network. Since the network is unpruned, ν is positive when pulled from the top and bottom edges and from the corners. Figure 2.14 shows a network which has been low ΔG_p pruned. As can be seen, the network is auxetic when pulled from the top and bottom edges as in Panel a, but not when pulled from the corners, as in Panel b. If we instead prune low ΔG_s bonds as in Figure 2.15, we observe the opposite behavior. The network is not auxetic when pulled from the top and bottom edges as in Panel a, and it is auxetic when pulled from the corners as in Panel b.

Figure 2.16 shows an isotropic network formed by iteratively pruning the lowest $\Delta G_p + \Delta G_s$ bond. Creating isotropic networks is a more demanding optimization task, since two moduli must be kept high relative to B instead of only one. As a result, ν of the isotropic networks is less negative than ν of anisotropic networks. The network shown is predicted to have $\nu = -0.25$ isotropically in the linear regime using $k_{ang} = 0.01$ as in other networks. The structure of this isotropic network is noticeably different from that of anisotropic networks - while anisotropic networks show significant rectangular ordering, the isotropic sample does not.

2.6.5 Effect of angle potentials on ν

Initial attempts to create auxetic networks in experiment were based on simulations that did not include angle-bending forces. In this work, we incorporate the effect of angle-bending forces as described in the main text. Here, we investigate what occurs when k_{ang} is varied for already-pruned networks. The results are shown in Figure 2.17. We start with a single 500 node network pruned to $Z = 3.87$ with $k_{ang} = 10^{-4}$ (analogous to simulations that ignored k_{ang}). As we increase k_{ang}, ν follows the same trends as networks pruned with those values of k_{ang}, as shown in Fig. 8 of the main text.

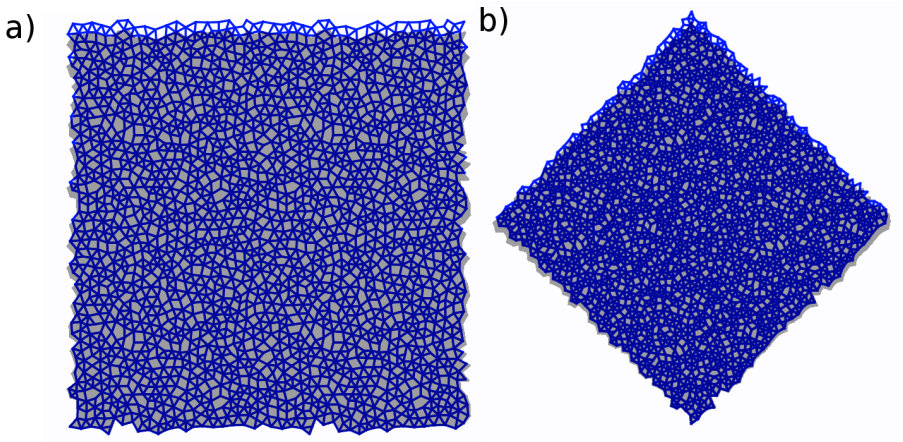

Figure 2.13: Unpruned networks deformed by pulling along the vertical axis. The gray shaded region shows the shape of the undeformed network. This network shows positive ν with respect to both deformations, since it is unpruned.

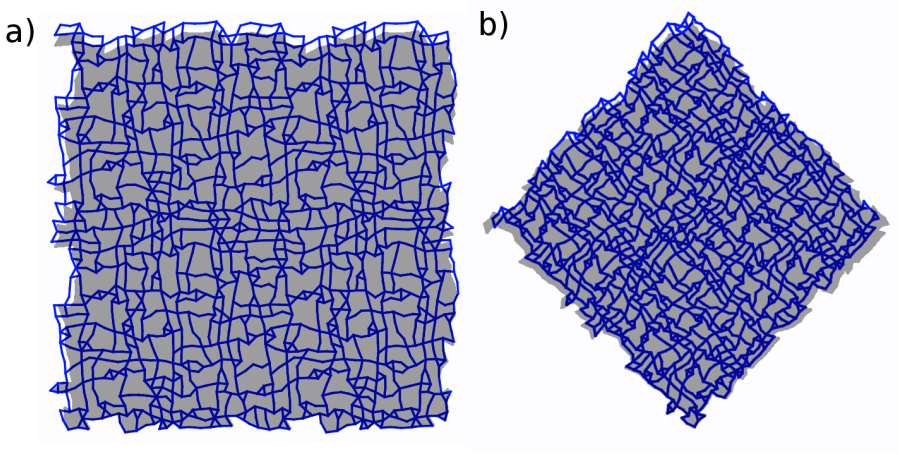

Figure 2.14: Low ΔG_p pruned network deformed by pulling along the vertical axis. The gray shaded region shows the shape of the undeformed network. This network is auxetic with respect to deformation normal to its top and bottom edge, but not when pulled from its corners.

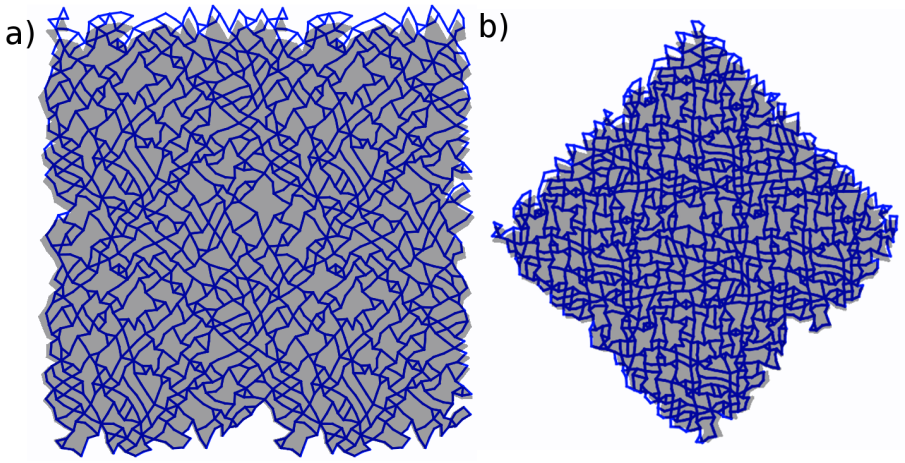

Figure 2.15: Low ΔG_s pruned network deformed by pulling along the vertical axis. The gray shaded region shows the shape of the undeformed network. This network is auxetic with respect to being pulled from its corners, but not deformation normal to its top and bottom edge.

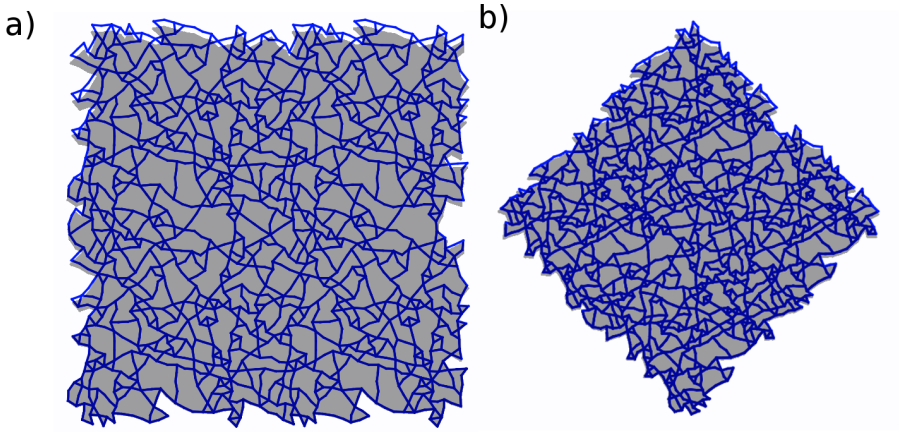

Figure 2.16: Low $(\Delta G_s + \Delta G_p)$ pruned network deformed by pulling along the vertical axis. The gray shaded region shows the shape of the undeformed network. This network is isotropic, so it auxetic for all types of deformation. However ν of this network is higher than in anisotropic networks.

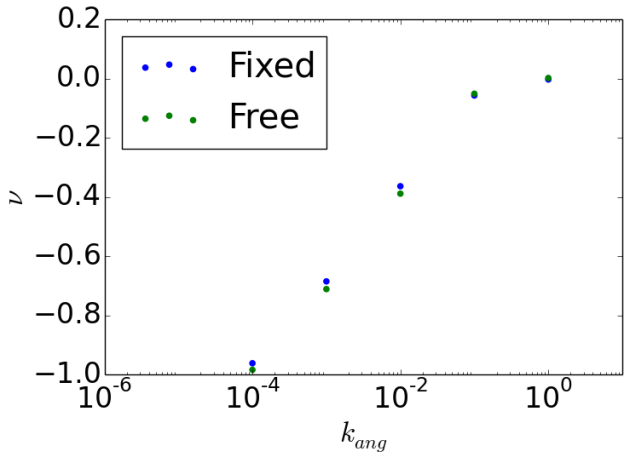

Figure 2.17: Poisson's ratio of a single network pruned to $Z = 3.87$ by low ΔG pruning at $k_{ang} = 10^{-4}$. The value of k_{ang} is then swept from 10^{-4} to 10^{0} with both fixed and free boundary conditions.

At $k_{ang} = 1$, the coefficients for angle bending and compression are equal. Interestingly, ν reaches zero at this point. We suggest that stronger angle-bending forces inhibit the complex deformations of the concave polygons present in these networks. Inhibiting this deformation will reduce auxetic behavior. The addition of the angle potential is the most important factor in ensuring that our models agree with experiment.

2.6.6 Boundary conditions

The boundary conditions of the networks in this study differ in two ways from previous attempts. In previous attempts, the simulations were periodic. In experimental realizations, however, there are no periodic boundaries and these periodic systems were terminated, with their top and bottom nodes fixed in the x dimension. In this work, we incorporate these experimental features into the simulation in order to match the experiments more closely. Figure 2.18 shows ν vs. ϵ_y for a periodic 500 node network which has been cast as a finite system tiled in both dimensions some number of times. The Poisson's ratio quickly reaches an asymptotic value as the tiling increases. However if a periodic system is simply made finite with no tiling (as is the case for $\#tiles = 1$), ν will be non-trivially less negative.

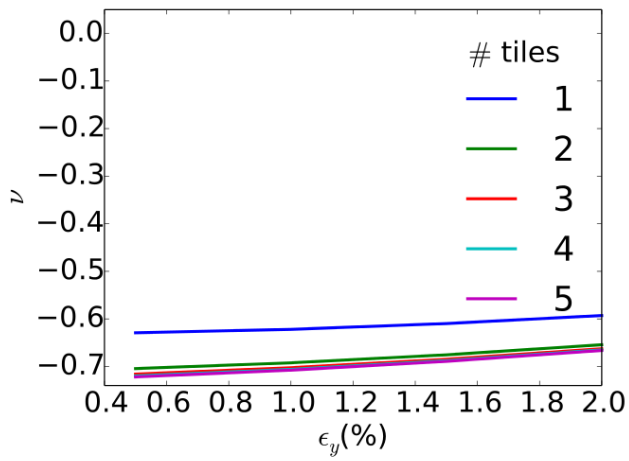

Figure 2.18: Poisson's ratio vs. uniaxial strain of simulated 500 node periodic networks which have been tiled in both dimensions and then made finite. Increased tiling decreases ν, as edge effects are reduced. These edge effects are not present when the periodic system is pruned. For systems of this size ν rapidly converges to a final value with tiling.

Figure 2.19 shows ν of networks with fixed and free boundary conditions pruned with low ΔG pruning from $Z = 5.2$ to $Z = 3.0$. In networks with fixed boundary conditions, nodes at the top and bottom of the network are restrained in both the x and y dimension upon deformation, mimicking experimental boundary conditions. In networks with free boundary conditions, nodes at the top and bottom of the network may relax in the x dimension upon deformation. As can be appreciated, the fixed boundary conditions do not significantly affect ν. All results in this work are produced using fixed boundary conditions unless otherwise specified.

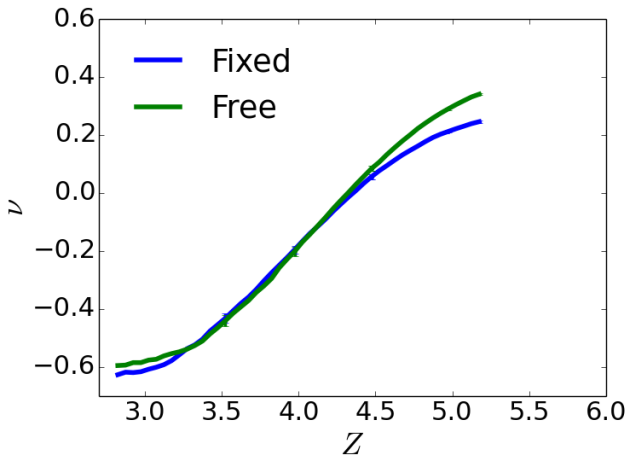

Figure 2.19: Poisson's ratio of networks pruned with fixed and free boundary conditions for 500 node networks. The boundary conditions do not significantly effect the resulting values of ν.

CHAPTER 3

FORMATION OF ISOTROPIC AUXETIC NETWORKS USING MATERIALS OPTIMIZATION STRATEGIES

3.1 Introduction

Precisely manipulating the mechanical properties of solids is a goal critical to the design of novel materials. Materials with negative Poisson's ratios, termed 'auxetics' represent a promising yet underutilized area of materials development. Auxetics show potential for applications in areas such as impact mitigation[5, 6], filtration [7, 8], fabric design [9, 10], and cases in which materials must maintain shape under deformation, such as in aerospace applications[32, 33].

A variety of auxetic materials have been proposed in recent years, including metamaterials[34, 35, 36, 19, 33], foams prepared by special processing techniques[12, 37, 38, 5], and composites[2]. The vast majority of these materials are anisotropic, meaning that the Poisson's ratio, ν, depends on the direction of strain, which is typically not desirable for applications. Of the few materials which are isotropic, all except specially prepared foams, which reach $\nu = -0.82$[38], are inherently two-dimensional or exceptionally complex[39]. To be widely useful, such materials must be isotropically auxetic, be readily fabricated in three dimensions, and show Poisson's ratios approaching the lower mechanical limit of -1[5].

Disordered networks derived from jammed packings present an appealing means of designing auxetic materials which satisfy these elusive criteria. Previous work has shown that networks can be tuned to show an auxetic response through selective pruning of bonds[1, 40]. In most crystalline solids, the change in G or B when a single bond is removed (termed ΔG_i or ΔB_i respectively) is identical for every bond, and these quantities are highly correlated. As a consequence, removing bonds will not significantly change G/B.

Disordered networks differ in two key ways: First, the distributions of ΔG_i and ΔB_i span several orders of magnitude. Second, these quantities are decorrelated[1, 25, 40]. Thus

by iteratively removing for example, the greatest ΔB_i or smallest ΔG_i bond, one can drive ν to negative values. Indeed, it has been shown that by iteratively pruning the smallest ΔG_i from disordered networks, materials can be formed in simulation and experiment with $\nu = -0.9$[40] in two dimensions. However, such materials are anisotropic as only one shear modulus was considered. When networks are instead pruned to be isotropic, ν only reaches -0.18.

Here, we show that by augmenting bond removal strategies with materials optimization techniques which modify node positions and bond strengths, disordered networks can be designed which are isotropic and show ν as low as -0.98. Such predictions are validated in experiment. As networks are optimized, distinct concave structural motifs emerge. Using an artificial neural network, we show that these motifs correlate well with ν. Auxetic networks also show high degrees of mechanical heterogeneity. As ν drops, changes in area of individual polygons which constitute the network become highly disperse. In addition, more auxetic networks show regions of negative moduli, highlighting the complex mechanics of these materials. Taken together, these results lay out a clear framework for the design of highly auxetic isotropic materials which can be readily applied to three dimensions.

3.2 Results and Discussion

3.2.1 Disordered networks

Disordered networks, the starting point of the materials optimization process, are initialized from jammed packings as described in detail in previous work[1, 24, 25, 40]. To summarize briefly, polydisperse particles are randomly positioned in the simulation box. System density is chosen to control the average coordination number, Z, which plays a strong role in network properties[1, 40]. Particles interact via a soft sphere potential shown in Equation 2.1. The system is relaxed and bonds are formed between all pairs of particles for which $r < \sigma_a + \sigma_b$. The soft sphere potential is then erased and the network is formed.

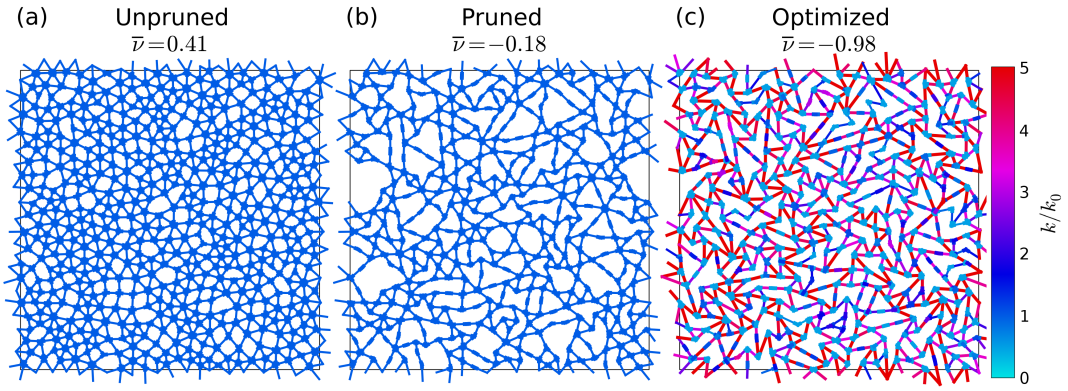

Figure 3.1: Networks at three steps in the materials design process. In Panel (a), an unpruned network with $Z = 5.2$ and $\nu = 0.41$. In Panel (b), the same network after low ΔG_i bonds have been pruned with $\nu = -0.18$, and in Panel (c), the same network after optimization with $\nu = -0.98$. Values of ν are averaged over 30 independent networks. The color at the end and along the length of each bond represents $k_{i,0}^{ang}/k^{ang}$ $k_i^{comp}/k_{i,0}^{comp}$, respectively. As can be appreciated, most values of k_i^{comp} are increased while those of k_i^{ang} are decreased.

3.2.2 Network model

Once networks are formed, the constituent bonds are described by two potentials - harmonic compression along the length of the bond, and harmonic bending around the node. These simple potentials have been shown to accurately capture experimental network behavior in both the linear regime and at high material strains[40].

3.2.3 Network formation and pruning

To form highly auxetic isotropic materials, three distinct steps are carried out: (i) network formation, (ii) pruning, and (iii) optimization. An example network after each of these steps is depicted in Panels a, b, and c of Figures 3.1 respectively.

Unpruned periodic networks, as exemplified in Panel a of Fig 3.1, are initialized with $Z = 5.2$ and show $\overline{\nu} = 0.41$. An initial value of $Z = 5.2$ was shown to produce maximally auxetic pruned networks in previous work, and so is used here [40]. Once networks are formed, the pruning process is carried out. To prune networks, the bond which shows the

lowest value of $\Delta G_i^p + \Delta G_i^s$ is iteratively pruned until Z is reduced to 3.5 and $\nu = -0.18$, as shown in Panel a Fig 3.2. Here G^p and G^s denote the two orthogonal shear moduli in two dimensions: pure and simple shear. An example of a pruned network is shown in Panel b of Fig 3.1. Further pruning does not significantly reduce ν.

3.2.4 Network optimization

Once networks are pruned, the optimization process is carried out to reduce ν to near -1. A gradient descent optimization technique is used, which optimizes the compression and angle coefficients of each bond as well as the position of each node. At each step in the optimization process, bond coefficients are updated using the criteria shown in Equation 3.1. Here k_i is the compression or angle coefficient for the i^{th} bond. Values of k_i are constrained to be between 0.5 and 5.0 times their initial value to ensure that bonds can be faithfully fabricated in experiment. The parameter Δ_k is the step size of the optimization, and is set so that the maximum change of a coefficient is $0.1max(k_{i,0})$ at each iteration.

Equations 3.2 and 3.3 show the update criteria for node positions. Nodes positions are optimized to minimize ν while a repulsive term ensures that nodes do not cross bonds. As with bond coefficients, Δ_r sets that maximum step size and is chosen such that the maximum node motion at each iteration is 0.1.

$$k_i(t+1) = k_i(t) - \Delta_k \frac{\partial \nu}{\partial k_i} \tag{3.1}$$

$$r_a(t+1) = r_a(t) - \Delta_r \frac{\partial E_a}{\partial r_a} \tag{3.2}$$

$$E_a = \nu + \sum_{i \in bonds} \epsilon \Big(\frac{\sigma}{|r_{ai}|} \Big)^6 \tag{3.3}$$

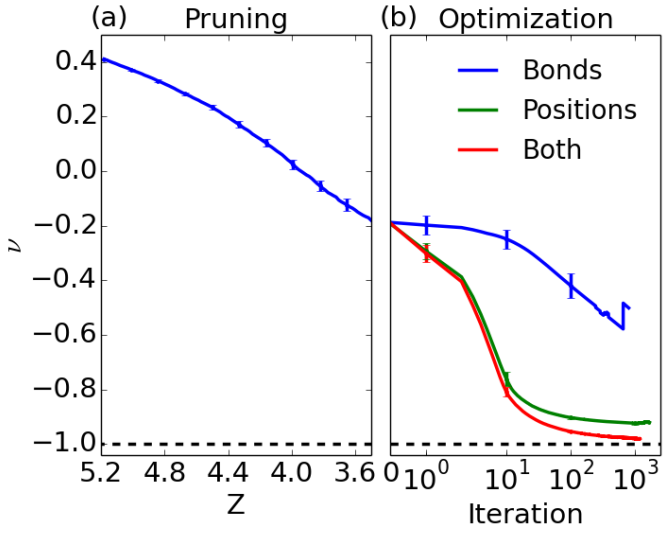

Figure 3.2: Poisson's ratio over the pruning and optimization process. Panel a shows ν as the network is pruned from $Z = 5.2$ to $Z = 3.5$. Pruned networks are then optimized as shown in Panel b. The three data sets show ν as (i) only bond strengths are optimized, (ii) only node positions are optimized, and (iii) both bond strengths and node positions are optimized.

3.2.5 Optimization results

Panel b of Fig 3.2 shows ν as the optimization process is carried out. Poisson's ratios resulting from optimizing only bond coefficients as in Eqn 3.1, only positions as in Eqn 3.2, and both parameters sets simultaneously are shown. All optimization algorithms yield isotropically auxetic materials. Optimizing only bond parameters yields materials with $\overline{\nu} = -0.50$, and optimizing only node positions yields $\overline{\nu} = -0.91$. Optimizing both quantities simultaneously, however, yields $\overline{\nu} = -0.98$, near the lower mechanical limit. An example of a network in which both node positions and bond strengths have been optimized is depicted in Panel c of Figure 3.1. These results demonstrate that node positions play the dominant role in controlling ν. This bodes well for creating experimental realizations, where node positions can be more precisely controlled than bond strengths.

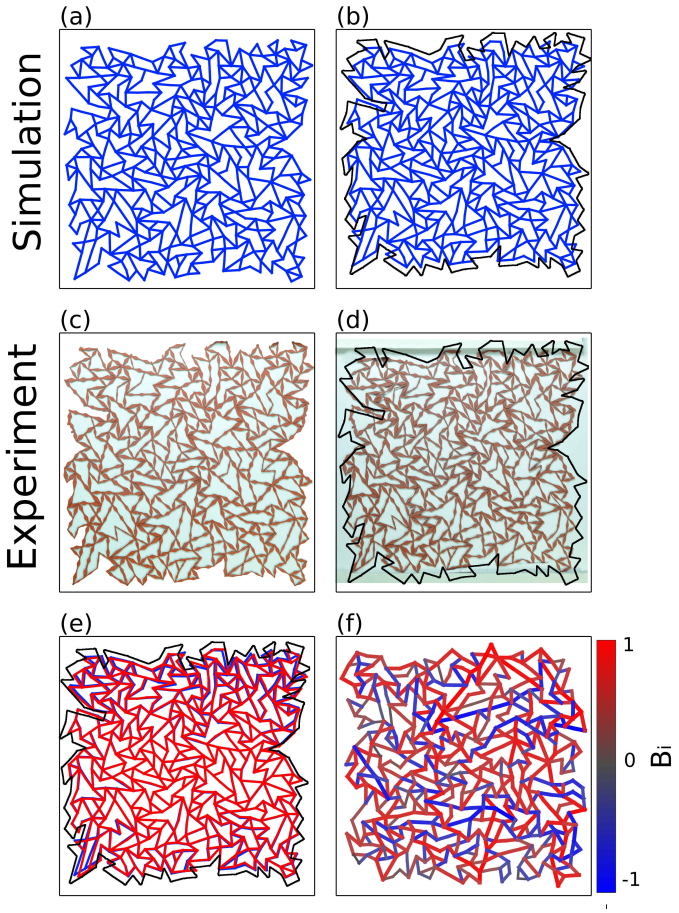

Figure 3.3: Isotropic auxetic networks compressed in simulation and experiment. (a) Uncompressed simulation of auxetic network predicted to show $\nu = -0.5$. (b) Simulated network uniaxially strained to $\epsilon_y = 5\%$ with outline of uncompressed network shown in black. (c) Uncompressed experimental realization of identical network. (d) Compressed experimental network at $\epsilon_y = 5\%$ with outline of uncompressed network shown in black. (e) Overlay of experimental (red) and simulated (red) networks at $\epsilon_y = 4\%$. (f) Bond-level contributions to B in network under uniform compression. Contributions are normalized by the largest value of B_i.

3.2.6 Experimental realizations

Experimental analogues of simulated networks are created by laser-cutting configurations from sheets of silicone rubber. A representative network is shown in Panel a Figure 3.3. Upon uniaxial compression in the vertical dimension (y), the network behaves auxetically, as shown in Panel b Figure 3.3. Thicknesses of bonds must be carefully controlled, as they are the experimental analogues of k_i^{comp} and k_i^{ang}. Bond compression strength is modulated in experiment by controlling the thickness along the length of the bond. Bond angular strength on the other hand is modulated by controlling the thickness near the end of bonds. To reduce the likelihood of bonds colliding, the thickness contribution due to compressive strength is tapered linearly from a maximum at the center of bonds to the ends. Exact protocol for setting thicknesses of experimental bonds is described in Methods and Materials.

Recent work has revealed within disordered polymer glasses regions of negative moduli[41]. Interestingly, regions of negative moduli also appear in disordered networks. A bond which has a negative contribution to B, for example, is under tension while the material is under compression, or visa versa. Panel f Figure 3.3 shows the per-bond contribution to B for a network with $\nu = -0.5$. Interestingly, (34%) of bonds in optimized networks contribute negatively to the bulk modulus, compared to 24% and 2% in pruned and unpruned networks, respectively.

3.2.7 Isotropic auxetic behavior

To validate that the networks are isotropic, two realizations of a 500 node periodic auxetic network are created in experiment. The two networks are cut from the same periodic unit cell, one as a square which lies flat along the x axis, and the other which lies at 45° to the x axis (the xy axis). The two networks are compressed along the x and xy axes, respectively. Deforming the first network along the x (or y) axis measures ν as it relates to G^p/B, which we denote ν_0. Deforming the second network along the xy (or yx) axis measures ν as it relates to G^s/B, which we denote ν_{45}. A material which shows the same value for ν_0 and

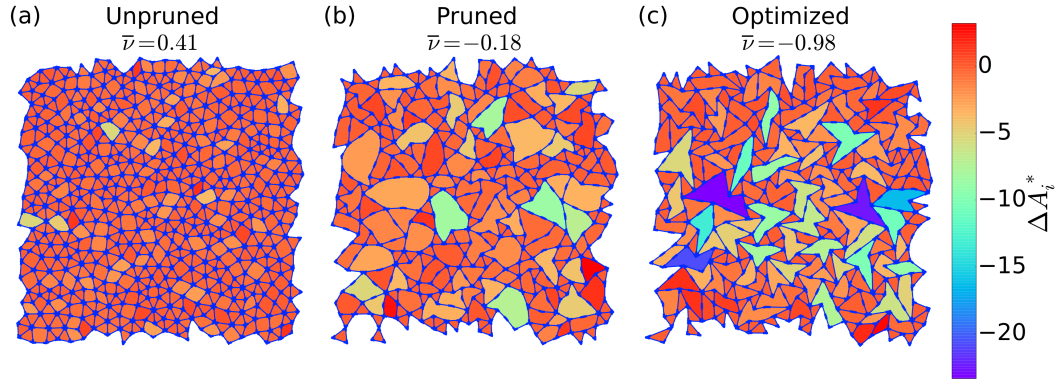

Figure 3.4: Normalized changes in minimal cycle areas, ΔA_i^* of a single 500 node network at the three stages of preparation: unpruned, pruned, and optimized. ΔA_i^* was measured after the networks were compressed by $\epsilon = 0.01\%$. More negative values of ΔA_i^* contribute to lowering ν. As quantified in Figure 3.5, networks with lower values of ν show more mechanically heterogeneous behavior.

ν_{45} is perfectly isotropic. The two networks show excellent agreement between simulation and experiment, showing $\nu_0 = -0.99, -1.03$ and $\nu_{45} = -0.88, -0.87$, for simulation and experiment respectively. The values of ν are nearly constant up to strains of 4%, and are shown in Figure S1.

3.2.8 Effect of pruning and optimization of moduli

As a result of the material optimization process, G of optimized networks is nearly doubled compared to that of non-auxetic networks. Here G is computed as the average of G^s and G^p, which are calculated as the total energy stored in the network under small deformation[1, 40]. Unpruned networks show $G = 38 \times 10^{-9}$, while pruned, auxetic networks show a decreased value of $G = 17.0 \times 10^{-9}$. Interestingly, optimized networks show $G = 69.5 \times 10^{-9}$, nearly a two-fold increase over that of unpruned networks, validating the idea that auxetic materials can in fact be mechanically resilient to shear. It is worth noting, however, that B in optimized

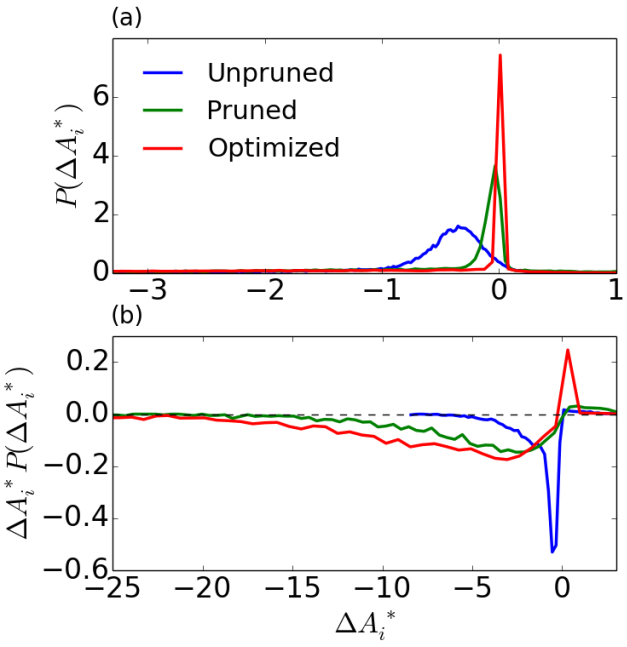

Figure 3.5: Distributions of minimal cycle deformations, ΔA_i^* upon compression for unpruned, pruned, and optimized networks. Panel a shows the probability distribution of ΔA_i^*. As networks are pruned and then optimized, the distributions becomes increasingly sharp. Panel b, which shows $P(\Delta A_i^*)$ weighted by ΔA_i^*, demonstrates that for pruned and optimized networks, the low probability outliers of ΔA_i^* are responsible for the majority of the material deformation.

networks is two orders of magnitude smaller than in unpruned networks.

3.2.9 Physical understanding of auxetic behavior

To understand the structural features which gives rise to auxetic behavior, we now study the properties of the individual polygons, or minimal cycles, which compose the network. The Poisson's ratio can be related to change in each minimal cycle's area, ΔA_i as shown in Equation 3.4. Here, x and y refer to the side lengths of the network and i is the i^{th} cycle. For clarity, values of ΔA_i in all data are normalized by strain and average minimal cycle area as shown in Equation 3.5. For the strains and used in this work, negative values of ΔA_i^* contribute to lowering ν.

Panels a, b, and c of Figure 3.4 show ΔA_i^* of each cycle for unpruned, pruned, and optimized networks respectively. As can be seen, the values of ΔA_i^* become more disperse as networks are pruned, and even more so when optimized. Additionally, it can be observed that all cycles with very low values of ΔA_i^* are concave, consistent with predictions from previous work [40].

$$\nu = \Big(\frac{1}{\epsilon_y}\Big)\Big(\frac{\sum \Delta A_i}{x_f y_o} + \frac{y_o}{y_f} - 1\Big) \tag{3.4}$$

$$\Delta A_i^* = \frac{\Delta A_i}{\overline{A}\epsilon} \tag{3.5}$$

The general observations which can be made about networks pictured in Figure 3.4 are now made quantitative with ΔA_i^* data taken from 30 independent networks at each stage in the formation process. The distributions of ΔA_i^* are shown in Panel (a) Figure 3.5. Unpruned, pruned, and optimized networks show average ΔA_i^* of -0.55, -1.04, and -1.87, respectively, with standard deviations of ΔA^* of 0.72, 2.38, and 3.75. The distributions become increasingly sharp as networks are pruned and optimized. Interestingly, the most probable value of ΔA_i^* for unpruned, pruned, and optimized of networks increases from -0.35, to -0.03 to 0.01. Consistent with the increasing most probable value, as networks become more auxetic, a greater fraction of cycles within the network increase in area upon material compression. The fraction of cycles with $\Delta A^* > 0$ for unpruned, pruned, and optimized networks is 0.06, 0.16, and 0.17. This unexpected behavior paints a picture in which materials become highly heterogeneous as they become auxetic. While negative values of ΔA_i^* contribute to lowering ν, many cycles in the most auxetic materials do nothing, or even grow. This suggests that auxetic behavior is largely the result of a relatively small number of highly compliant cycles.

To better appreciate the contribution of cycles at each ΔA_i^* to ν, Panel b of Figure 3.5 shows $\Delta A_i^* P(\Delta A_i^*)$, the probabilities weighted by the magnitude of deformation. This

quantity corresponds to the relative contribution of cycles at that ΔA_i^i to the total change in network area and thus ν. For unpruned networks, cycles with relatively small values of ΔA_i^* between -3 and 0 constitute 92% of cycles, and make up 84% of the change in area. As networks becomes more auxetic, the picture changes significantly. In pruned networks, 70% of cycles show ΔA_i^* between -3 and 0, which make up only 31 of the total change in area. However a long tail of cycles of 30% of cycles with $\Delta A_i* < -3$ contribute 61% of the change in area. The picture becomes more extreme in the optimized case, where the 62% of cycles with ΔA_i^* between -3 and 0 contribute 14% of the total area chance, while the 21% with $\Delta A_i^* < -3$ contribute 77%. Together, these findings show that auxetic behavior is marked by highly heterogeneous mechanics. This opens to door to designing materials with a select few high compliant regions fused together by large relatively rigid sections.

3.2.10 Machine learning analysis

Modern machine learning techniques provide a powerful platform for understanding how structure relates to material properties. Here, feed forward neural networks are trained to predict ν across the entire pruning and optimization process. By determining the minimal feature set required to predict ν, we can surmise which physical parameters control ν.

Panel (a) of Figure 3.6 shows predicted values of ν for a neural network trained on histograms of angles between adjacent bonds on nodes. Examples of such histograms for unpruned, pruned, and optimized networks are shown in Panel (c) of Figure 3.6. The neural network is trained and tested on networks through the entire pruning process, and during the optimization process for networks where bond coefficients and node positions are optimized, and for networks where only node positions are optimized. Predictions are generated using leave-one-out cross-validation. The predictions are accurate across the entire range of ν, with a mean-square error (MSE) of 0.0010. Interestingly, the network is predictive even for networks where the bond coefficients have been optimized. This suggests that angles between bonds play the dominant role in determining network properties even when bond

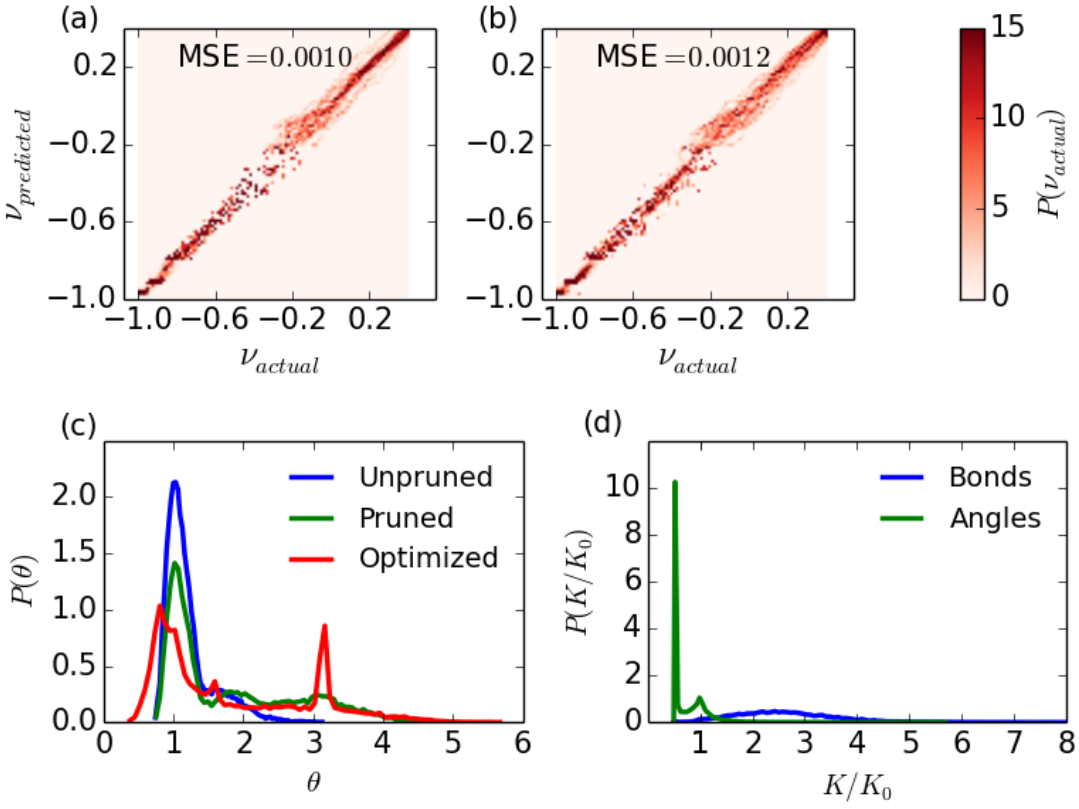

Figure 3.6: Neural network predictions of ν and sample distributions used to train network. (a) Predictions of ν for networks during pruning, and during optimization based on positions as well as bond strengths and positions. Neural network are trained only on angle probability distributions. (b) Predictions of ν for networks using node positions and bond coefficients during pruning and optimization using the schemes in (a) as well as optimizing only bond coefficients. Neural networks are trained on bond coefficient and angle probability distributions. (c) Probability distributions of angles between adjacent bonds at nodes. (d) Probability distribution of compressive and angular coefficients for optimized networks.

coefficients have been optimized.

Panel (b) of Figure 3.6 show predicted values of ν when an identically structured neural network is trained on both angles as in Panel (a) as well as histograms of bond coefficients as shown in Panel (d) of 3.6. Here, all classes of optimized networks as shown in Figure 3.2 are included. Note that including bond coefficients is now necessary, as in some networks, only bond coefficient are optimized. This suggests that using these two parameter sets, network behavior can be completely captured.

Panels (c) and (d) of Figure 3.6 show snapshots of training data. Panel (c) shows probability distributions of angles between adjacent bonds on nodes for unpruned (Z=5.2), fully pruned (Z=3.5), and fully optimized (using both node positions and bond coefficients) networks. As can be seen, the unpruned network angles are tightly distributed around 1.2 radians which corresponds to $2\pi/Z_0$ where $Z_0 = 5.2$. In pruned networks, the average angle grows to 1.8 radians and the distribution becomes more disperse. In optimized networks, extremely small angles proliferate and a peak appears at π. Panel (d) shows probability distributions for $k_i^{comp}/k_{i,0}^{comp}$ and $k_i^{ang}/k_{i,0}^{ang}$. As can be seen, many angles are weakened (82%), while a small fraction are unchanged or grow stronger. The average angle is 0.73 times as strong as its original value. Note that the large peak at 0.5 is due to the imposed minimum angle strength. Compressive coefficients, on the other hand, show a broad distribution with the majority growing stronger (98%). The average k_i^{comp} is 2.6 times stronger than its original value.

3.3 Conclusion

The work presented here lays out a clear framework for designing tunable highly auxetic isotropic materials with unique mechanical properties. Being metamaterials, the structures will be auxetic if fabricated at any length scale, from building-scale to molecular-level structures. While fabrication for large scale devices is relatively straightforward, fabrication at smaller scales presents a greater challenge. One such option is to use purposefully assem-

bled DNA-functionalized nanoparticles. Such assemblies have been shown to have a host of unusual mechanical properties[42, 43], and can be made amorphous (ask josh for citation), a requirement for these materials. Glassy materials can also show a host of unusual and tunable materials properties depending on material processing and formation conditions [44, 45, 46]. With sufficiently high resolution, 3D printing may also provide a feasible path towards material fabrication [47]. With several possible routes forward, fabricating micro-scale auxetic networks will prove a challenging yet fruitful avenue for materials development.

CHAPTER 4

AGE AND STRUCTURE OF A MODEL VAPOR-DEPOSITED GLASS

4.1 Introduction

Glasses represent kinetically arrested states of matter, whose characteristics depend strongly on the process of formation[48]. They are generally prepared by gradual cooling of a liquid to temperatures below the glass transition, T_g, of the corresponding bulk material. The properties of liquid-cooled, "ordinary" glasses depend on cooling rate and on the "age" of the glass - the amount of time that the material is allowed to rest at a given temperature (below T_g). Lower cooling rates (or ageing) lead to materials that lie deeper in the underlying potential energy landscape. They tend to have a higher density[49, 50], greater mechanical strength[51], lower enthalpy[49] and higher onset temperature (the temperature at which the film transforms from a glass into a liquid upon heating)[52], than those prepared by fast cooling. Higher stability is desirable in a wide range of applications, from organic electronics[53] to drug delivery[54].

Recent experimental work has shown that glasses prepared by a process of physical vapor deposition (PVD) can reach levels of stability that are equivalent to those of liquid-cooled glasses allowed to age for thousands of years[50, 55]. These highly stable PVD glasses are formed by depositing the glass former onto a substrate whose temperature is somewhat lower than T_g. It has been proposed that newly deposited molecules can freely explore configurational space near the surface of the growing film, leading to molecular arrangements that correspond to lower free energy states than those accessible by quenching a bulk liquid [50, 56, 57].

The properties of three-dimensional (3D) PVD glasses have also been examined in computer simulations. On the one hand, results for a 3D model glass former consisting of a binary mixture of spherical particles indicate that vapor deposition leads to materials that exhibit higher kinetic stability, and whose structure is similar to that of their liquid-cooled counterparts[58]. On the other hand, simulations of model glasses consisting of anisotropic molecules suggest that a PVD process leads to materials that exhibit varying amounts of anisotropy[59]. Importantly, past simulations of vapor deposited glasses have relied on a formation process that involves repeated minimizations of potential energy, which are introduced for computational reasons. As such, past studies have been unable to reveal the role that hot molecules impacting a surface can have on the relaxation of the underlying glassy film. A recent study investigated the formation of highly stable 2D glasses prepared through a "pinning" technique[60]. The authors formed equilibrium glasses by freezing in-place a small fraction of the particles in a glass-forming liquid, raising the glass transition temperature above the current temperature, and glassifying the system in an equilibrium configuration. As insightful as the results from the pinning strategy have been, however, such glasses do not incorporate the presence of an interface into the simulations.

Past studies of two-dimensional (2D) systems have shed considerable light into the behavior of glasses. A variety of colloidal particles, including polystyrene and latex, have been shown to assemble into monolayers exhibiting varying degrees of local and long-range order [61, 62]. By virtue of being quasi-2D, such studies allow for the direct observation of glassy dynamics, including structural relaxation near the glass transition, thereby serving as a source of validation for theory and simulations [63, 64]. Atomic 2D glasses have also been prepared, consisting of silica on a graphene substrate [65]. Such systems show a coexistence between crystalline and amorphous regions, which range in size from several unit cells to tens of nanometers across. Going beyond systems of spherical particles, 2D colloidal glasses have been formed using ellipsoids in order resist crystallization [66].

In this work we build upon these past studies by introducing a PVD formation approach that mimics closely that employed in experiments. Specifically, we avoid the artificial energy minimizations and temperature controls that were employed in past computational studies of 3D systems. Furthermore, by restricting our simulations to 2D systems, where configurations can be more easily visualized and inspected, we arrive at unambiguous correlations between local structure and energetic stability. Three important results emerge from our analysis. First, in contrast to previous reports, we find that vapor deposition leads to glasses whose energetic stability far exceeds that of samples prepared by liquid cooling. Second, it is shown that newly deposited particles generate cascades of hot particles that could serve to relax the interior of the film, and that help explain the advantages of PVD processes for preparation of new glasses. Third, we find that the structure of PVD glasses is isotropic and identical to that of liquid-cooled glasses, provided these two classes of materials are compared under preparation conditions for which their inherent structure energies are comparable.

4.2 Results

4.2.1 Model system

The details of the vapor deposition simulations presented here are discussed in the Methods section. Here we point out that the model considered in this study consists of a binary mixture of spheres whose glass-forming behavior in the bulk has been examined exhaustively, and that vapor-deposited samples are prepared by depositing groups of hot vapor particles onto a substrate held at a temperate T_s. Particles are deposited until a desired film thickness of approximately 35 molecular diameters is reached. Liquid-cooled samples are prepared by heating vapor deposited films above T_g, and then cooling them at a constant rate to a temperature near zero. A representative system is shown in Figure 4.1, where the blue layer

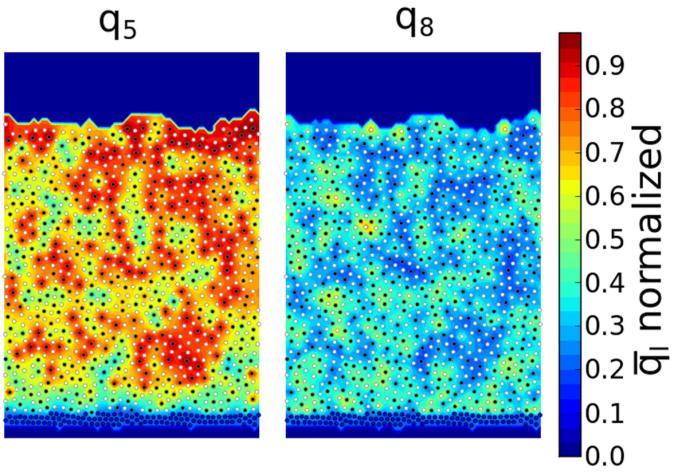

Figure 4.1: Diagram of liquid-cooled sample formed with $t_{cool} = 1.4 \times 10^1 \tau_\alpha$. Type A and B atoms are shown in white and black, respectively, while substrate atoms are shown in blue. This film has an inherent structural energy, E_{IS}, of -3.90. The background coloring in the left and right panels represents values of bond order parameters q_5 and q_8 as discussed in the Structural features section. Substrate atoms are held tightly in place once equilibrated using harmonic springs. Atoms are kept inside the simulation box using a harmonic repulsive wall as described in Methods.

at the bottom represents the substrate, the white spheres are of type A, and the black spheres are of type B. Vapor-deposited and liquid-cooled films are prepared using a wide range of deposition and cooling rates. The inherent structure energy E_{IS} of a configuration, used to quantify its stability, is the potential energy of a configuration brought to its local energy minimum.

The 2D model considered here exhibits considerable local structure; to quantify this structure, we rely on two bond order parameters that assign values to each particle based on the configuration of its neighbors [67]. The first, denoted by q_5, selects for local pentagonal order. The second, q_8, selects for local rectangular order. The background colors in Figure 4.1 correspond to the magnitude of such order parameters.

4.2.2 Energetic properties

The energetic properties of PVD glasses are determined using only particles in the "bulk" region of the films, which is highlighted in Figure 4.2. It corresponds to a wide domain of constant density and composition. Figure 4.2 shows results for a variety of PVD and liquid-cooled films. From Figure 4.2, we point out two features that arise at the surface of these films: first, the density near the surface decreases gradually. This results from the surface being uneven, as density is simply taken as the number density at a horizontal cross section. Second, χ_A, the mole fraction of type A, rises near the surface of the films, as shown by previously Shi et al.[68]. More stable configurations maximize A-B interactions, as ϵ_{AB} is larger than ϵ_{AA} and ϵ_{BB}. Type A particles, which are more abundant at $\chi_A = 65\%$, segregate to the surface to maximize these interactions.

The inherent structure energy, E_{IS}, is an effective measure of the position of a glass on the potential energy landscape [69]. Inherent structure energies of several liquid-cooled and PVD films are shown in Panel (a) of Figure 4.3. The deposition time for vapor deposited films, t_{dep}, corresponds to the interval between addition of new groups of particles to the growing film. During this time, newly deposited particles are allowed to cool down and become integrated into the growing film. The cooling time, t_{cool}, is the time over which an ordinary film is cooled from $T = 5\,T_g$ to $T = 0.2\,T_g$. Cooling and deposition times are expressed in units of the alpha relaxation time of this system, τ_α, which is calculated using the self-intermediate scattering function at $T = 1.10\,T_g$, as shown in Figure 4.13. For all simulations, new, "hot" particles are introduced into the system with an initial temperature of $T_i = 5.0\,T_g$. The simulated bulk T_g for this material is approximately 0.21 in Lennard-Jones units, as determined by taking the fictive temperature of a liquid-cooled film prepared with $t_{cool} = 1.4 \times 10^3\,\tau_\alpha$.

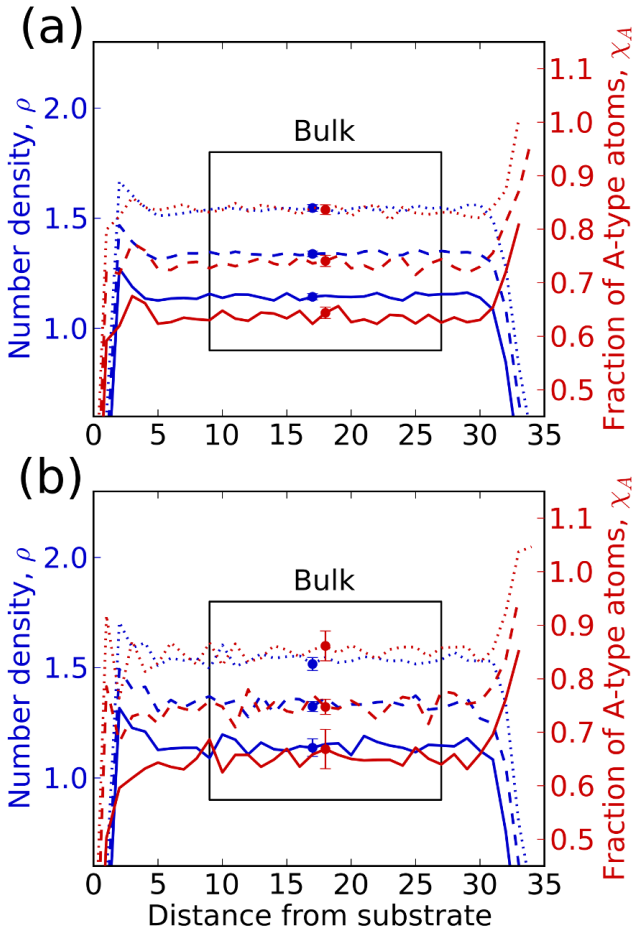

Figure 4.2: Number density and composition for liquid-cooled and vapor deposited films formed under several conditions. Data for liquid-cooled films are shown in Panel (a) while data for vapor deposited films are shown in Panel (b). The dotted, dashed, and solid lines represent films formed with $t = 1.4 \times 10^{(1,2,3)}$ at film temperatures of (0.75, 0.85, 0.85) T_g. From top to bottom in each figure, ρ is offset by (0.4, 0.2, 0.0) and χ_A is offset by (0.2, 0.1, 0.0). In (a), t refers to t_{cool} and T refers to the film's current temperature in the course of cooling. In (b), t refers to t_{dep} and T refers to substrate temperature. Only atoms in the bulk region shown are used in calculations unless otherwise specified. We define the bulk region to be several σ_{AA} away from where bulk composition and density properties are reached to ensure that edge effects are not present in the data. Error bars represent 95% confidence intervals.

Previous experimental work has shown that the optimal substrate temperature, T_s, for the formation of glasses via PVD lies in the vicinity of $0.85\,T_g$[50, 55, 70, 71]. For the 2D model system considered here, we find that that the optimal substrate temperature (that leading to the lowest inherent structure energy) for a given deposition time decreases as deposition slows. PVD samples formed with $t_{dep} = 1.4 \times 10^0$ show an optimal T_s of $0.87\,T_g$, while samples formed with $t_{dep} = 1.4 \times 10^4 \tau_\alpha$ show an optimal T_s of $0.68\,T_g$ of T_g, as shown in Table 4.1. Furthermore, PVD samples prepared at lower deposition rates exhibit significantly lower inherent-structure energies than those prepared at faster rates. As can be appreciated in Figure 4.3, depositing with $t_{dep} = 1.4 \times 10^4\,\tau_\alpha$ and $T_s = 0.68\,T_g$ gives $E_{IS} = -3.965$ while $t_{dep} = 1.4 \times 10^0\,\tau_\alpha$ and $T_s = 0.87\,T_g$ gives $E_{IS} = -3.918$. Optimal temperatures are found by fitting a cubic spline to the values of E_{IS} vs. T_s in panel (a) Figure 4.3 and taking the temperature at the minimum energy value.

We suggest that the ideal deposition temperature decreases with slower deposition rate due to a competition between thermodynamics and kinetics. As the substrate temperature decreases, lower energy states become more thermodynamically favorable, but the kinetics to reach such states become slower. As films are formed through more gradual deposition, atoms are allowed more time to approach equilibrium energy states. As originally proposed by Swallen et al., the ideal substrate temperature is where an ideal trade-off is found between which states the system is moving towards (thermodynamics) and how closely the system can approach those states (kinetics)[50].

Panel (b) in Figure 4.3 shows E_{IS} of liquid-cooled films evaluated at $T = 0.25\,T_g$ as a function of cooling time (t_{cool}). Previous work on 3D models suggests that E_{IS} varies linearly with $\log(t_{cool})$ [72, 58]. The 2D glass model considered here exhibits a nonlinear dependence. As shown in Panel (b) of Figure 4.3, a power-law fit of the form:

$$E_{IS} = 0.090\,t_{cool}^{-0.087} - 3.98 \tag{4.1}$$

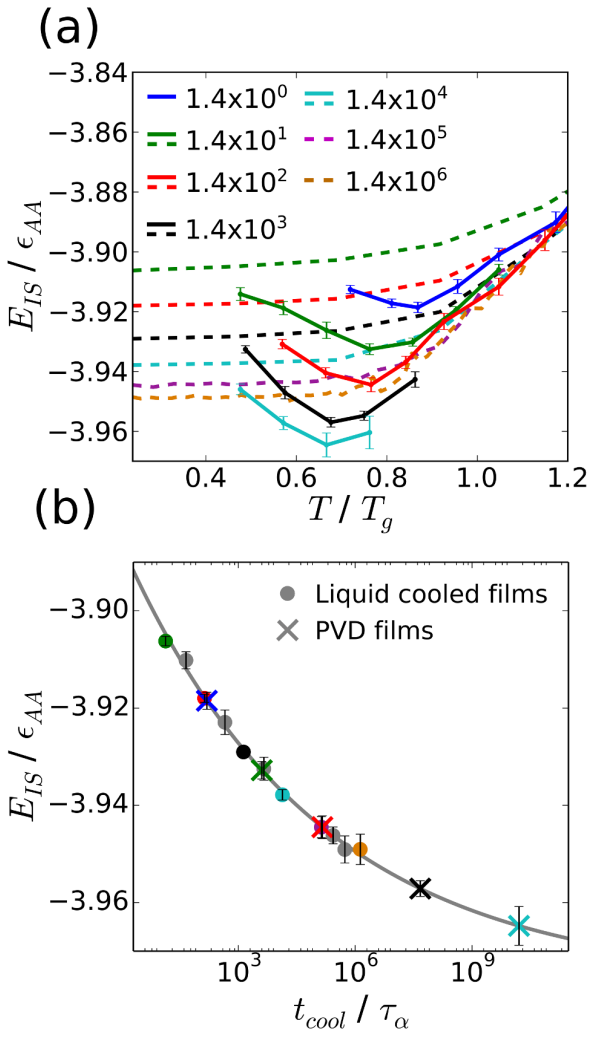

Figure 4.3: Inherent structure energy of PVD and liquid-cooled films along with predicted liquid-cooling rates required to form films with energy equal to that of PVD films. (a) Inherent structure energy of PVD and liquid-cooled films vs. temperature. Dashed lines represent liquid-cooled data while solid lines represent PVD data. For liquid-cooled samples, the film's temperature refers to the temperature at which E_{IS} was calculated during its linear cooling. For PVD films, temperature refers to the substrate temperature with which the film was formed. Legend values refer to t_{cool} or t_{dep} for a given data set, in units of τ_α (calculated at $T = 1.10\,T_g$ as shown in Figure 4.13). The ideal substrate temperature decreases as t_{dep} increases for PVD films as described in Table 4.1. Error bars represent 95 % confidence intervals. (b) Inherent structure energies of liquid-cooled films at $T = 0.25\,T_g$ vs t_{cool} with power law fit from Equation 4.1. Colors of the points correspond to the liquid cooling or deposition rate of that the color represents in panel (a). If a point is grey, that particular cooling rate is not shown in panel (a). 95% confidence intervals are shown. The X's represent predicted t_{cool} values necessary to form liquid-cooled films with energy equal to PVD films, as calculated using Equation 4.1. PVD film energies in panel (b) correspond to that of the substrate temperature that yields optimal stability for each t_{dep}.

describes our results reasonably well. Equation 4.1 can be used to estimate how slowly a liquid should be cooled to form ordinary glass films having inherent structure energies comparable to those of PVD films. These estimated cooling rates are shown by crosses in panel (b) of Figure 4.3, for t_{dep} values ranging from 1.4×10^0 to 1.4×10^4, separated by order-of-magnitude intervals. On the basis of this simple extrapolation, one can anticipate the most stable PVD configuration prepared here to be equivalent to a liquid-cooled sample prepared with $t_{cool} = 1.6 \times 10^{10} \tau_\alpha$, which is 1.1×10^5 times longer than the time utilized for the slowest cooling rate that we could accomplish with our computational resources.

As PVD films are formed more slowly, the inherent structure energy apparently approaches that of the deepest minima in the amorphous region of the potential energy landscape. By setting the liquid cooling time equal to infinity in Equation 4.1, one can estimate that these lowest energy states have inherent structure energies of -3.98. By this prediction, the most stable configurations produced here for $t_{dep} = 1.4 \times 10^4$ with $T_s = 0.67\,T_g$ are only 0.013 above this value. We emphasize here that these estimates should be viewed with some skepticism, as the curve shown in the inset of Figure 3 extends well beyond the data that can be generated with available computational resources. Also note that the more stable vapor deposited films show a similar, slowing rate of change for inherent structure energy as a function of deposition time, which we believe supports the idea that these films are gradually approaching the bottom of the amorphous regions of the potential energy landscape.

While the overall composition of each film is fixed, the local composition of the bulk region cannot be controlled precisely. On average, type A particles are excluded from the bulk, and the degree of exclusion varies by film formation type and formation time. It has been shown that E_{IS} for 3D $Ni_{80}P_{20}$ films depends linearly on composition over a small range [72]. That linear dependence is also observed in our 2D films. To account for the variation in E_{IS} due to composition effects, we perform linear fits of E_{IS} to χ_A for several cooling times. We find $\partial E_{IS}/\partial \chi_A = 1.6$ near $\chi_A = 0.65$ fits well across a wide range of film formation times

during both liquid cooling and vapor deposition. The energy of all films is thus interpolated to $\chi_A = 0.65$ for all films, including those used in Figure 4.3. The average χ_A values for PVD and liquid-cooled films in the bulk are 0.648 and 0.637, respectively.

While the aim of this work is to investigate how vapor deposition may influence the structure of glass films, it is worth pointing out that for situations where PVD films and liquid-cooled films exhibit comparable structures, vapor deposition provides an efficient computational method for generating low-energy glasses. For instance, forming a liquid-cooled film with $t_{cool} = 1.4 \times 10^5 \, \tau_\alpha$ requires 5.0×10^7 time units and 5.0×10^5 seconds on a particular machine. To form a vapor deposited film of equal energy, one can deposit with $t_{dep} = 1.4 \times 10^2 \tau_\alpha$ and $T_s = 0.76 \, T_g$, which requires 5.12×10^6 time units and 4.1×10^4 seconds on the same machine, or approximately one order of magnitude less CPU time. Using predicted equivalent cooling rates from Table 4.1, we anticipate that this difference becomes greater for more stable, lower-energy films. We estimate that our most stable PVD films, prepared with $t_{dep} = 1.4 \times 10^4 \, \tau_\alpha$, would require over three orders of magnitude more CPU time if prepared by liquid cooling.

4.2.3 Kinetic properties

The stability of the PVD films prepared here, based upon two measures, is comparable to that observed in experiment. First, we calculate the fictive temperature, T_f, of several liquid-cooled and PVD films. The fictive temperature is defined as the temperature at which the energy line extrapolated from the glass phase meets the energy line extrapolated from the equilibrium liquid phase, as shown in Figure 4.4. In the experiments of Swallen et al., the fictive temperature of the glass former 1,3-bis-(1-naphthyl)-5-(2-naphthyl)benzene (TNB) ($T_g = 347 \ K$) was measured for three types of films: ordinary liquid-cooled films, aged liquid-cooled films, and PVD films[50]. These authors found the T_f of these films to be 0.99 T_g, 0.95 T_g, and 0.91 T_g, respectively. Later work in which PVD films were formed at

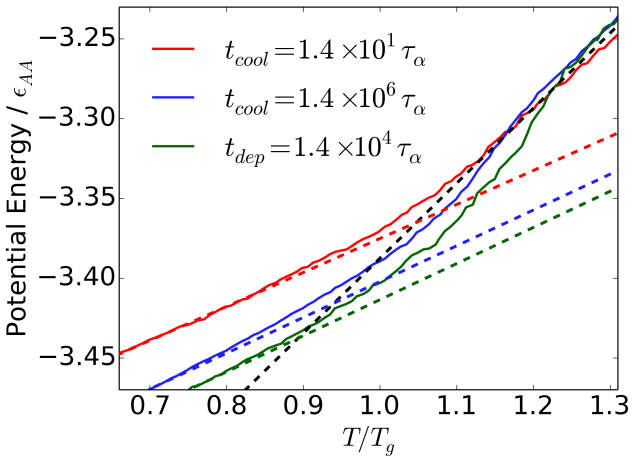

Figure 4.4: Potential energy versus temperature for PVD and liquid-cooled films on heating. Fictive temperatures, T_f, are calculated for three types of films: Shown in red and blue are films formed by liquid cooling at our smallest and largest cooling time, respectively. Shown in green are films formed by vapor deposition at our largest deposition time. The fictive temperatue is calculated to be the temperature where the extrapolated liquid line (dashed black) meets the extrapolated glass lines (dashed red, blue, green). Films are heated from below T_g at a constant rate of 2×10^{-6} in reduced units. We calculate fictive temperatures of 1.05 T_g and 0.94 T_g for the liquid cool films, and 0.89 T_g for the PVD films.

slower deposition rates yielded TNB films with T_f of 0.88 T_g [73]. Following their work, we calculate T_f for three types of films: films formed by liquid-cooling with $t_{cool} = 1.4 \times 10^1$ τ_α, films formed by liquid-cooling with $t_{cool} = 1.4 \times 10^6$ τ_α (analogous to an aged glass prepared by liquid cooling), and films formed by vapor deposition using our slowest deposition rate, $t_{dep} = 1.4 \times 10^4$ τ_α. The results are shown in Figure 4.4. We find $T_f = 1.05$ T_g, 0.94 T_g and 0.89 T_g for the three classes of films, respectively. To measure T_f, films were heated at a constant rate of 2×10^{-6} from well below T_g. The ordering and spread of the corresponding fictive temperatures from simulations are consistent with those found in experiment.

Second, we calculate transformation times for both liquid-cooled and PVD films and compare them to experiment. The transformation time is defined as the time required for a material to melt after rapid heating to a temperature above T_g. Ultrastable PVD glasses have been shown to melt through a liquid front that originates at the surface of the film.

Growth front velocities for ultrastable indomethacin (IMC) have been measured across a wide range of temperatures above T_g. These velocities have been found to be constant over a wide range of film thicknesses [74]. We measure film transformation times by rapidly heating films from below T_g to 1.1 T_g, and determining the time required for the film to reach an equilibrium energy, as described in the Methods section. The results, normalized by τ_α at $T = 1.1\ T_g$, are shown in Figure 4.14. Energies used to calculate these transformation times are shown in Figure 4.15. The experimental τ_α of IMC at $T = 1.1\ T_g$ is 1.3×10^{-4} seconds, while our 2D system shows a τ_α of 1.48×10^{-10} seconds assuming a Ni-P model. Our most stable PVD films show a transformation time of 158 τ_α, and are 8.93 nm thick, using a Ni-P model. Using data from the literature, we calculate that a 8.93 nm thick film of IMC would melt over 354 τ_α, where τ_α is measured at 1.1 T_g for IMC[74]. By this comparison, our PVD films are just over half as stable as would be expected experimentally for films of this thickness. Note, however, that this comparison is highly speculative, given that both the materials and dimensionality of these two types of films are different. We suggest that the lower stability observed in simulations relative to experiment is expected, given that our slowest film growth rate (using a Ni-P model) is 48 μm per second. Experimental growth rates are typically a few nanometers per second, i.e. several orders of magnitude slower. Additional details on the conversion to real units and film growth rates are given in the "Conversion to real units" section of the Methods[75].

4.2.4 Comparison with 3D films

Vapor deposition in two dimensions is more efficient than in three dimensions. Two-dimensional films exhibit surface regions which show higher mobility than 3D films assembled using comparable models. This trait allows 2D materials to explore configuration space more effectively, which we suggest leads to the lower inherent structure energy seen in 2D. To compare 2D and 3D films formed by PVD, we examine 3D films with the same interaction parameters as in 2D, but with $\chi_A = 0.80$, as in previous work [72, 58]. We define the efficiency of vapor

deposition as the ratio of a PVD film's growth rate to the film's equivalent liquid cooling rate. In 2D, equivalent t_{cool} values are found using the power law shown in Equation 4.1. In 3D, E_{IS} is linearly fit to $\log(t_{cool})$ for accessible cooling rates. By combining results from 3D films generated using NVE deposition (Figure 4.16) with the 2D data presented here, we estimate that vapor deposition in 2D is between 6×10^1 and 6×10^2 times more efficient than in 3D for the films with the lowest inherent structure energies.

Molecules near the surface of a glassy film are more mobile than those in the bulk [76]. Highly mobile molecules can explore configurations more rapidly, thereby allowing films prepared by vapor deposition to reach lower energies than those without mobile surface regions. Consistent with this understanding of surface mobility and our estimated efficiencies, we find that molecules near the surface of 2D films are both more mobile and encompass a thicker region than in 3D. To quantify these observations, we calculate $\langle \Delta r^2 \rangle$ of 2D and 3D films for a range of temperatures and film stabilities. For 2D and 3D samples held at $T = 0.75\, T_g$, we find that molecules in the surface region are, on average, 70% more mobile than those in the bulk. The high-mobility region extends nearly twice as far into the film than in 3D, as shown in Figure 4.5. Surface mobilities do not depend strongly on film stability, as shown in Figure 4.17. Mechanistically, we suggest that the thicker and more mobile surface layer in 2D allows atoms to sample more configurations before being frozen into their glassy states, thereby enabling exploration of lower energy basins along the free energy landscape.

4.2.5 Heat transfer through films

As hot vapor particles impact the surface of growing films, energy is transferred from the vapor into the film. In this material, heat transfers along tightly coupled strings of particles. Correlated strings of particles in glasses have been reported before[77]. Note, however, that the strings discussed here are inherently different as they correspond to events initiated by

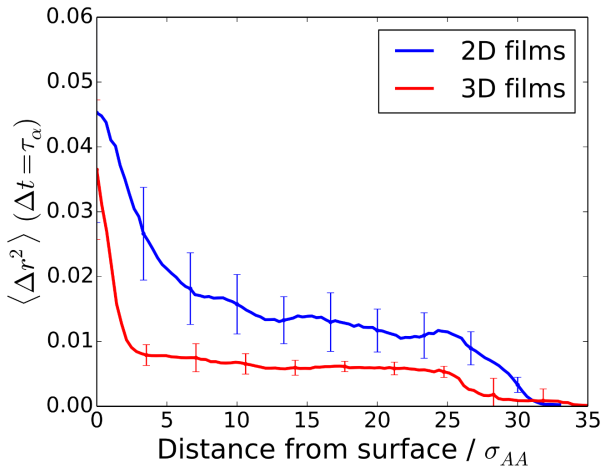

Figure 4.5: Mobility of atoms in both 2D and 3D PVD films. We measure $\langle \Delta r^2 \rangle$ with respect to distance from film surface calculated over $\tau_{\alpha,2D}$ time units for 2D and 3D films. Both films were formed with $t_{dep} = 1.4 \times 10^1 \, \tau_{\alpha,2D}$, which gives nearly equal film growth rates. The films are held at $T = 0.75 \, T_g$. Comparing 2D to 3D, the surface region is 70% more mobile and nearly twice as thick in 2D. The surface region is defined using the distance from surface where linear interpolations of the bulk region and the more steeply sloped surface region meet. Error bars represent the standard error from 20 2D and 3D films.

newly deposited hot surface particles that introduce a disturbance. Several representative configurations of long strings are shown in Figure 4.6. Particles in these thin strings reach kinetic energies near that of the vapor particle at impact. While 75% of these strings penetrate less than 4 atom diameters into the film, occasionally, such strings can be significantly longer. In 3% of the cases, strings penetrate over seven atom diameters into the film, thereby providing a highly focused energy transfer process down to a relatively large depth.

Heat transferred along strings enters the film much more rapidly than would be expected from a diffusive mechanism. To illustrate the difference, one can rely on a simple one-dimensional continuum model where heat only transfers by diffusion. The continuum model's surface is initialized at a high temperature, such that the total amount of heat added to the continuum and molecular dynamics models are the same. Parameters for the continuum model, such as heat capacity and thermal diffusivity, are determined from molecular dynamics simulations as described in the Methods section. One can then generate temperature

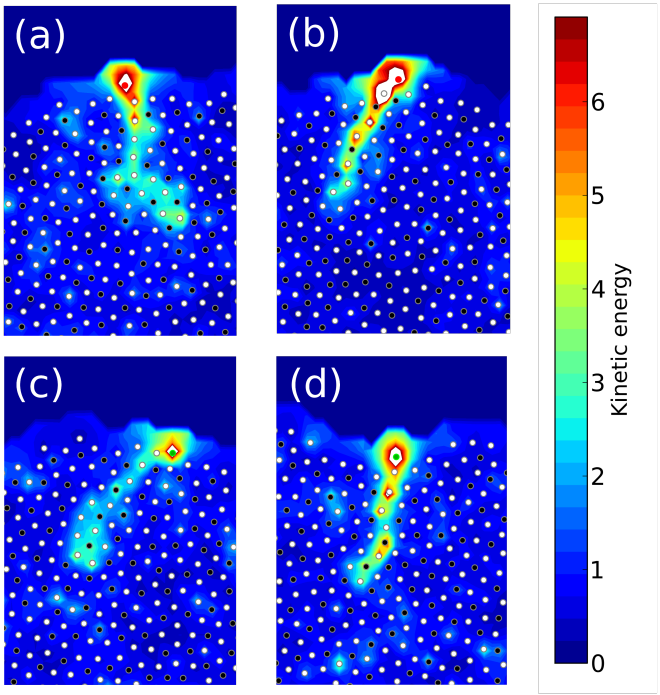

Figure 4.6: Strings of high-energy particles resulting from the impact of a vapor atom during the PVD process. The four panels, (a), (b), (c), and (d), show independent examples of energy transfer along strings of particles after a vapor particle impacts the surface of the film. The kinetic energy of each particle is normalized by $k_B T_g$. Prior to impact, the films were equilibrated at $T = 0.5\,T_g$. As energy travels through the string, it is localized to only one or two atoms at a time. For clarity, atoms involved in a string are shown with their maximum kinetic energy over the lifetime of the string. The particle that impacted the surface is colored red or green, depending on whether it is of type A or B, respectively. Particles already in the film are colored white or black for type A or B, respectively.

profiles with respect to distance from the film's surface of these two models as they evolve in time. Figure 4.7 shows the temperature profile of the PVD films shown in Figure 4.6 as compared to the continuum model at $1.1 \times 10^{-2}\tau_\alpha$ after impact or initialization. If one looks at heat transfer averaged over many films, the continuum results are recovered, as shown in Figure 4.21. However, in the case of long strings, heat transfer is much faster and energy is much more localized than in the continuum case, as shown in Figure 4.7.

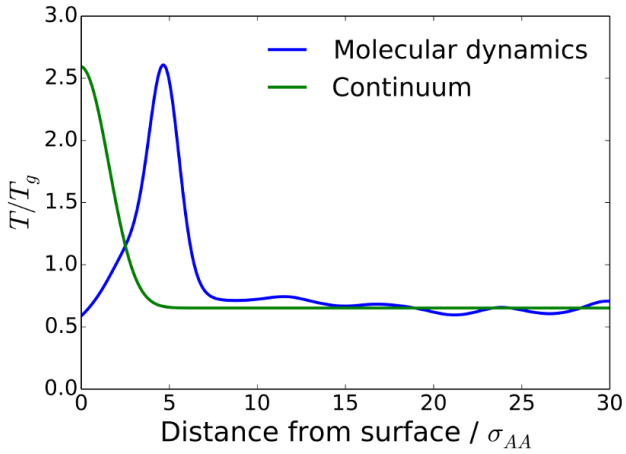

Figure 4.7: Temperature profiles resulting from continuum and molecular dynamics heat transfer when vapor particle impacts on the surface of a film. The temperature profile of molecular dynamics simulations shown in Figure 4.6 is shown $2.6 \times 10^{-4} \tau_\alpha$ after the impact of a vapor atom, as compared to temperature profile from similar continuum simulation. The continuum simulation is initialized with a high temperature at its surface to match heat added by vapor atoms' impact. Molecular dynamics simulations which show long strings are used to show the process's effect on thermal transport. The molecular dynamics temperature profile is taken from a narrow slice of the film around the four strings shown in Figures 4.6, such that the temperature increase can be easily resolved.

4.2.6 Structural features

The 2D films considered here exhibit considerable local pentagonal and rectangular order. Figures 4.1 and 4.8 show representative configurations of the system. The q_5 and q_8 order parameters (which select for local pentagonal and rectangular order, respectively), are used here to analyze the structure of the films[67]. Additional details on the order parameters' selectivity for different geometries are given in Figures 4.22, 4.23, and 4.24. The q_l order parameter, which is calculated for each particle based on the arrangement of its neighbors, is defined in Equation 4.2, where a is a particle, N is the set of a's neighbors, and Y_{lm} is the spherical harmonic for the specified l and m:

$$q_l(a) = \sqrt{\frac{4\pi}{2l+1} \sum_{m=-l}^{m \leq l} |q_{lm}(a)|^2} \tag{4.2}$$

$$q_{lm}(a) = \frac{1}{\widetilde{N}} \sum_{n \in N} Y_{lm}(a \rightarrow n) \tag{4.3}$$

High q_5 pentagons tend to form mostly as five white type A particles surrounding a single black type B particle. For this reason, q_5 is calculated only for type B particles. The q_8 parameter is calculated for all atoms. The nearest four neighbors of atoms in high q_8 rectangular structures tend to be of different type, thereby maximizing the A-B interaction. Figure 4.1 shows a contour map of $\overline{q_5}$ and $\overline{q_8}$ values calculated for a liquid-cooled film with a cooling time of $t_{cool} = 1.4 \times 10^1$. Here $\overline{q_l}$ denotes a time averaged q_l parameter averages over in-cage vibrations. It can be seen that high-q_8 clusters are of medium size, while locally-ordered q_5 clusters, which cannot tessellate, appear to be pentagonal. A similar coexistence of medium-range ordered clusters and locally-ordered structures was reported in a simulated atomic glass system in which particles' anisotropy frustrated crystallization[78].

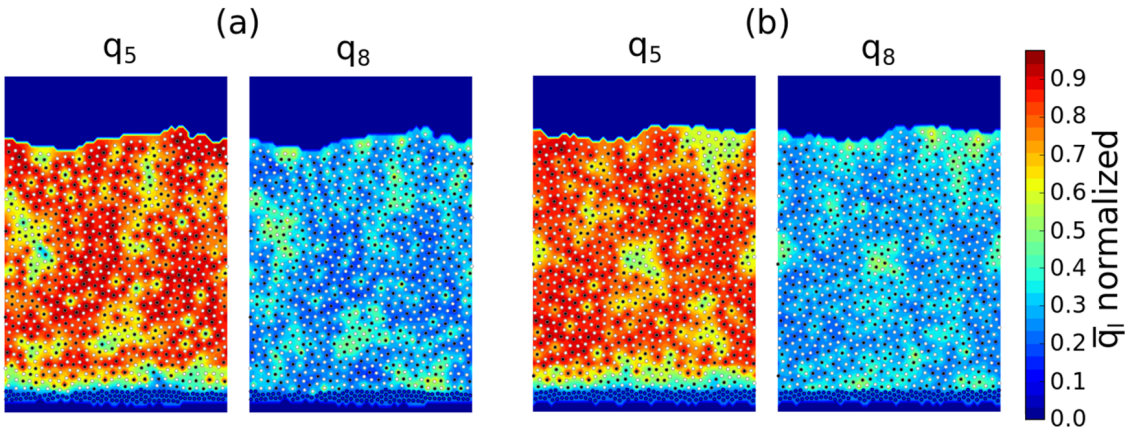

Figure 4.8: Contour maps of q_5 and q_8 for liquid-cooled and PVD films both with $E_{IS} = -3.95$. Panel (a) shows liquid-cooled film formed with $t_{cool} = 1.4 \times 10^5\,\tau_\alpha$ at $T = 0.25\,T_g$. Panel (b) shows vapor deposited film formed with $t_{dep} = 1.4 \times 10^3\,\tau_\alpha$ and $T_s = 0.75\,T_g$. These films are of equal inherent structural energy, allowing for direct comparison of the structures. The ordering within these two films shows no systemic differences, suggesting that isotropic PVD glasses are equilvalent to those formed by liquid cooling when the films are of equal inherent structure energy.

To assess the extent of order in these films, particle groups are classified as highly ordered or not using a simple cutoff scheme described in the "Order parameters" section of Methods. High-order cutoff values are chosen to be $\phi_5 = 0.55$ and $\phi_8 = 22.0$, or 78% and 34% of their values relative to perfectly pentagonal or square configurations (which yield the maximum values for these order parameters). All results can be reproduced using different cutoffs as shown in Figures 4.25, 4.26, 4.27, 4.28, 4.29, 4.30, .

We define the degree of order, D_l, as the fraction of particles involved in high-l ordered groups. We plot the D_l for all PVD and liquid-cooled films in Figure 4.9. We find that as the films become more stable, the q_8 character decreases, while the q_5 character increases. This can be appreciated by visually comparing Figure 4.9 to Figure 4.3, and by comparing the relatively unstable film in Figure 4.1 to the relatively stable films in Figure 4.8. Given the direct relationship between these parameters and E_{IS}, we conclude that the structure and stability of these films are well captured by the q_5 and q_8 parameters.

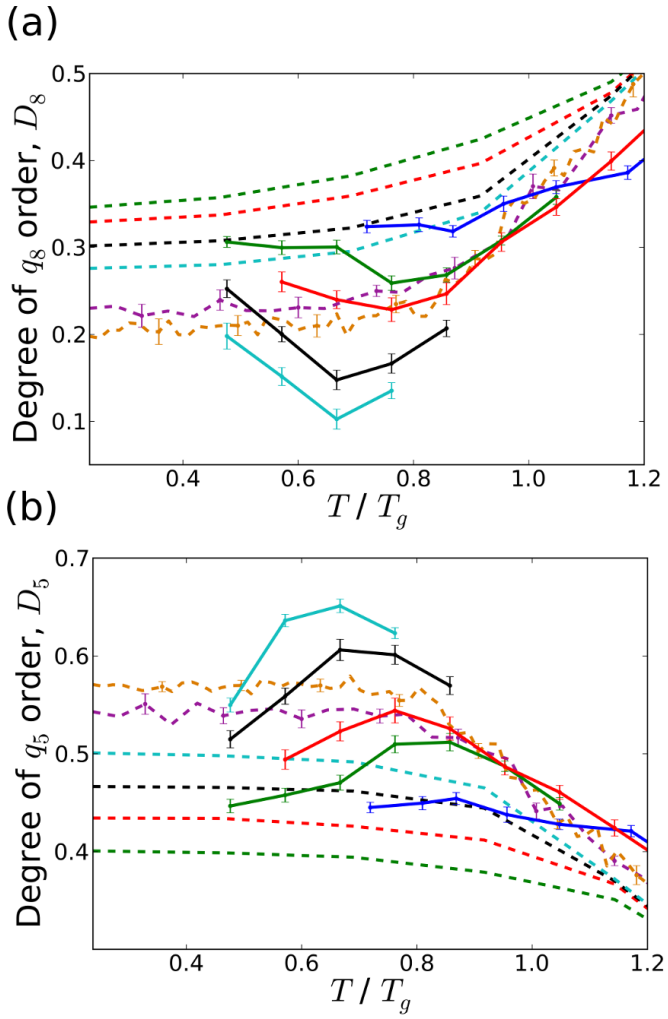

Figure 4.9: Degree of q_5 and q_8 order in PVD and liquid-cooled films. Dashed lines represent data from liquid-cooled films, while solid lines represent data from PVD films. Panel (a) shows data for the q_8 order parameter while Panel (b) shows data for the q_5 order parameter. The colors correspond to the same rates as in Figure 4.3, where blue is $t = 1.4 \times 10^0$ τ_α, orange is $t = 1.4 \times 10^6$ τ_α, and colors in between are separated by one order of magnitude in cooling rate. D_5 increases with film stability while D_8 decreases. These data show the same trends as the inherent structure energy shown in Figure 4.3, suggesting that these metrics provide a quantitative link between structure and stability in these glassy films. D_8 is calculated using all particles in the bulk, while D_5 is calculated using only type B particles in the bulk, as pentagonal structures form almost exclusively around these atoms. Error bars represent the standard error; they are only shown for liquid-cooled samples when the error is non-negligible.

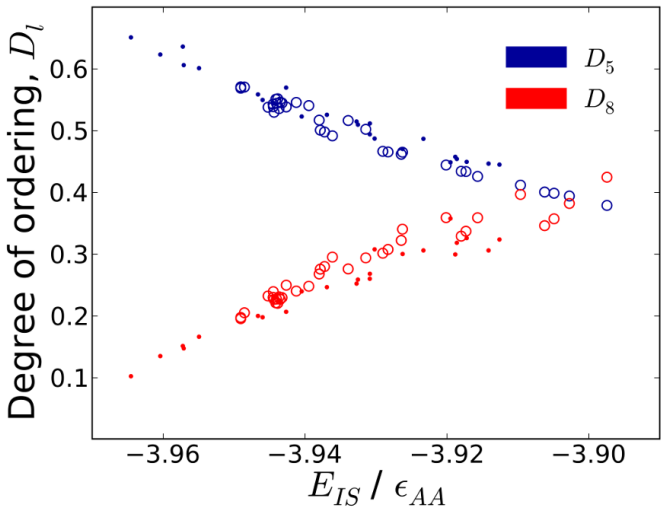

Figure 4.10: Degree of q_5 and q_8 ordering for vapor deposited and liquid-cooled films versus inherent structural energy. Solid circles represent vapor deposited data while open circles represent liquid-cooled data. Data for liquid cooling is taken from runs with t_{cool} ranging from $1.4\times10^1\,\tau_\alpha$ and $1.4\times10^6\,\tau_\alpha$, while data for vapor deposition is taken from runs with t_{dep} ranging from $1.4\times10^0\,\tau_\alpha$ to $1.4\times10^4\,\tau_\alpha$. Only data from films with $T<0.5T_g$ are used. q_5 and q_8 show an inverse relationship with q_5 increasing with film stability and q_8 decreasing. The q_l values of films with equal energy appear substantially equivalent regardless of film formation style, considering that compositions of the two types of films are not identical.

Figure 4.10 shows the degree of q_5 and q_8 order vs. E_{IS} for all liquid-cooled and PVD films. Only data from films well in the glassy state, $T<0.2$, are included. The q_5 and q_8 trends with temperature are similar and independent of the process of formation. These results can in fact be used to estimate inherent structure energy from degree of order since both D_5 and D_8 behave monotonically with E_{IS}. The degree of q_8 order for PVD films on average lies slightly below that of liquid-cooled films. We attribute this slight difference to the differences in composition between PVD and liquid-cooled films: on average, their bulk compositions are $\overline{\chi_A}=0.648, 0.637$, respectively.

Note, however, that more subtle differences could in principle exist between PVD and liquid-cooled samples. In Figure 4.31, we present data on the scale of ordered groups in these films. As with D_l, we find that the properties depend solely on E_{IS} of the films. Figure 4.8 compares vapor deposited and liquid samples with $E_{IS}\approx-3.95$. The contour

map shows no systematic differences in high-order cluster size, location, or shape. Comparing the film in Figure 4.1 to the more stable films in Figure 4.8, one can appreciate the increase in q_5 and the corresponding decrease in q_8 character that comes with increasing stability.

To conclude, a new method was introduced to prepare glasses in silico through a process of vapor deposition. The method was applied to investigate a model 2D glass forming liquid. After comparing the structure and energy of the resulting materials to that of ordinary liquid-cooled glassy films, it was found that *in-silico* physical vapor deposition greatly expands the range of film properties and structures that can be accessed as compared to traditional liquid cooling. In the 2D materials studied here, the range of structures includes pentagonal clusters and square-grid ordered regions of varying size. Under appropriate conditions, forming films by physical vapor deposition creates extremely low energy films, equivalent to liquid-cooled films cooled five orders of magnitude slower than possible on available computers. By varying the rate of vapor deposition, it is found that the ideal substrate temperature decreases with slowing deposition rate. In 2D, the surface layer of glassy films is thicker than it is in 3D, leading to a more effective PVD formation mechanism. Upon impacting a growing PVD film, newly deposited molecules form strings of hot particles that can reach well into the interior of the film, possibly providing an additional relaxation mechanism that helps the system explore its energy free landscape. An analysis using bond order parameters that select for square and pentagonal order revealed that films transition from a high square-grid character structure to a locally-ordered pentagonal structure as films stabilize. By examining the change in D_5 and D_8 in films formed using both methods, it was possible to establish that the degree of order does not depend on the formation type. More generally, the results presented in this work serve to demonstrate that, for the simple, isotropic model considered here, the glassy materials prepared by PVD are the same as those prepared by gradual cooling from the liquid phase, and that PVD glasses correspond to liquid-cooled glasses prepared at extremely slow cooling rates.

4.3 Methods

4.3.1 Simulation Parameters

The films in this work consist of a binary mixture of Lennard-Jones particles with a third particle type acting as the substrate. The interaction potential is given by Equation 4.4, where r is the distance between two particles, r_c is the distance beyond which interactions are not considered, and ϵ and σ change the strength and range of the interactions.

$$E = 4\epsilon\left((\frac{\sigma}{r})^{12} - (\frac{\sigma}{r})^{6}\right) \qquad r < r_c \tag{4.4}$$

These simulations use the values $r_c = 2.5$, $\epsilon_{AA} = 1.0$, $\epsilon_{AB} = 1.5$, $\epsilon_{BB} = 0.5$, $\sigma_{AA} = 1.0$, $\sigma_{AB} = 0.8$, $\sigma_{BB} = 0.88$. Values of ϵ and σ for the A and B particles acting on the substrate are 1.0 and 0.75, respectively. The masses of all particles are set to 1.0. The simulation box uses periodic boundary conditions in the x dimension and finite in y. The x dimension is parallel to the substrate while the y dimension is perpendicular. The simulations box is $30\sigma_{AA}$ wide and the height is set so that the boundary is $10\sigma_{AA}$ above the surface of the film as it grows. A timestep of $\Delta t = 0.005$ is used for all simulations. A Nosé-Hoover thermostat is used to maintain the temperature of all NVT ensembles [79].

Inherent structural energies were calculated by minimizing configurations using the FIRE algorithm with energy and force tolerances of 1×10^{-10}[80]. All simulations were performed using LAMMPS[81] and all figures were generated using Matplotlib[82].

4.3.2 Formation of PVD Films

Vapor deposited films are formed by initializing a substrate, then adding groups of atoms to the simulation box and allowing them to settle and cool on the growing film. The substrate is formed such that it does not impose any strong ordering the on film. First, substrate particles are randomly placed in a small rectangular area near the bottom of the simulation

box. The rectangle spans the width of the box and is 3 σ_{AA} tall. The atoms are tethered to their original positions using harmonic springs with a spring constant $k = 5$. The substrate is then minimized using the FIRE algorithm. The substrate atoms are then re-tethered to their minimized positions using harmonic springs with $k = 1000$. The initial weak spring ensures that the substrate thickness stays roughly constant during the minimization. Throughout the simulation the temperature of the substrate is held constant using a Nosé-Hoover thermostat in an NVT ensemble as described above. A wall with a harmonic repulsive potential is placed 10 σ_{AA} above the substrate. The wall is moved as the film grows to keep the distance between the film and the wall constant.

The film is grown using the following method: Ten particles are initialized in a region $3-5$ σ_{AA} above the growing film. The particle types are chosen to keep the film configuration as close to $\chi_a = 0.65$ as possible. The particles are initialized with random velocities at $T = 1.0$, as in previous work[58, 72]. The new particles and the growing film are then simulated as an NVE ensemble for t_{dep}. The new particles cool by natural heat transfer through the growing film to the substrate. This process is repeated until the films have a height of approximately $35\sigma_{AA}$.

In all but films formed with $t_{dep} = 1.4 \times 10^0$, the film temperature was tightly distributed around T_s. Film temperatures for those formed with $t_{dep} = 1.4 \times 10^0$ were deposited quickly enough that T_{film} was roughly $0.1\,T_g$ higher than T_s. In these cases, the actual temperature of the film was used in data.

4.3.3 Formation of Liquid Cooled Films

Liquid-cooled films are generated by heating vapor deposited films to $T = 1.0$, then recooling linearly over the time t_{cool}. The wall and substrate spring parameters are not changed during this process. To ensure the independence of each liquid-cooled film, the heated configurations are equilibrated for a random time ranging from 100 to 10000 time units while at $T = 1.0$. The films are cooled to $T = 0.05$, at which point the inherent structural energy has essentially

stopped decreasing.

4.3.4 Transformation Time Measurements

Transformation times are measured by heating a film to $T = 1.1\ T_g$ over 100 time units, then setting the thermostat to $T = 1.1\ T_g$ and measuring the potential energy of the film as it melts. When a film's potential energy is 90% of the way from its initial energy to its final energy, it is said to be transformed. We find that if the films are instantaneously heated from very low temperatures ($T = 0.25\ T_g$) to above T_g, the films expand extremely quickly, push off the static substrate, effectively 'jump'. For this reason, we introduce the initial heating step.

4.3.5 Thermal Conductivity Measurements

Parameters for the one-dimensional continuum heat transfer were taken from molecular dynamics simulations. In the model, the equation $\frac{dT}{dt}c_v = q = \kappa\nabla T$ is iterated, where T is temperature, t is time, c_v is heat capacity, and κ is thermal conductivity. c_v is determined by heating the systems around in the temperature of interest, and measuring the energy required. Thermal diffusivity is measured using the Green-Kubo relation which relates the auto-correlation of heat flux to thermal diffusivity.

4.3.6 Order Parameters

When selecting highly ordered q_8 clusters, two techniques are used to refine groupings. First, any cluster that is of 5 or fewer atoms is ignored. Second, we note that multiple q_8 clusters are occasionally connected by single-atom-wide chains of q_8-ordered atoms. For the purposes of counting cluster size, we would like to separate these clusters, as they are structurally distinct (but still connected). To do this, we remove particles from q_8 clusters using the following method: First, we count how many of a given atom's neighbors (within a radius of 1.2) are in

a q_8 ordered group. Then we look at those ordered neighbor particles and perform the same count. If the sum of all of these ordered neighbors is less than five, we remove the particle from its ordered group, as the atom is likely part of some thin protrusion or connection. The beta relaxation time is defined here as the time over which the self-intermediate scattering function decays from its initial value of 1 to its in-cage plateau value of roughly 0.9 as shown in Figure 4.42. A neighbor cutoff of 1.2 was used for equation 4.3. This value represents the first minimum in the radial distribution function and gave good contrast for bond order parameter values.

4.3.7 Conversion to Real Units

In order to facilitate comparison to experiment, the Lennard-Jones units used in this work are converted to real units. We cast type A particles into nickel and type B particles into phosphorus. The simulated atom of nickel (type A) has mass and Lennard-Jones parameters of unity; to convert into real units, one only needs the energy, length, and mass by which those parameters were normalized. Dimensional analysis shows that the time unit in simulation is given by $t_{unit} = \sigma\sqrt{m/\epsilon}$, with Lennard-Jones parameters for nickel as $\epsilon = 5.65 kcal mol^1$ $= 23,640 Jmol^1$, $\sigma = 2.55210^{10} m$, and the mass is $58.6910^3 kgmol^1$ [75]. Dividing the and mass by Avogadros number, we find that the real time unit is $4.02110^{13} s$. Our longest PVD simulations lasted 9.210^{10} simulation timesteps with $dt = 0.005$ Lennard-Jones time units, which translates into a real time of $1.8510^{-4} s$. Films are roughly 35σ, or 8.93×10^{-9}meters thick, giving a growth rate of $48 \mu m$ per second.

4.4 Appendix

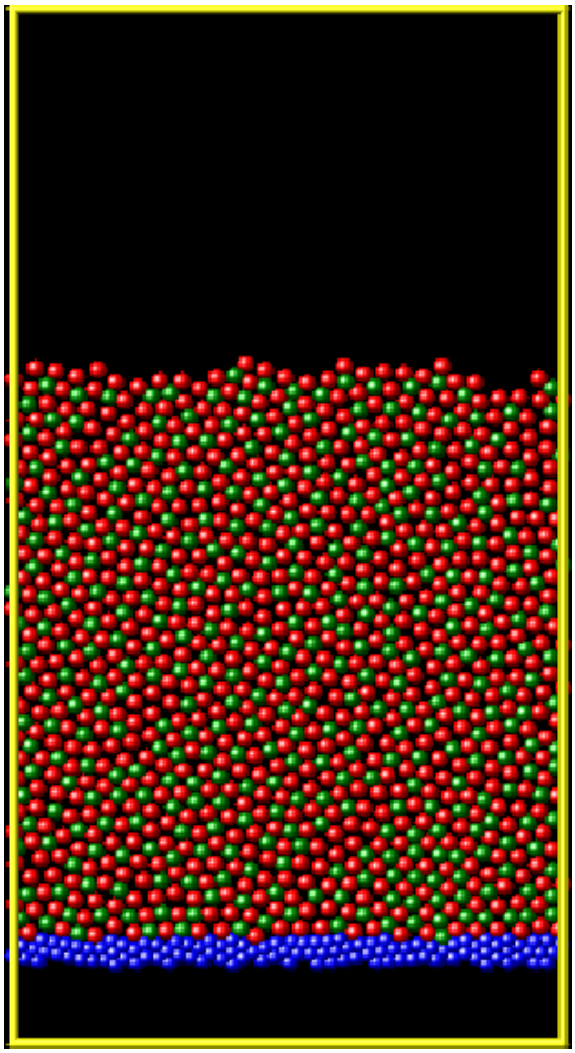

Figure 4.11: A sample vapor deposited configuration generated using $t_{dep} = 1.4 \times 10^4 \tau_\alpha$ with $T_s = 0.67 T_g$. This film represents one of our most stable configurations. Type A particles are shown in red while type B particles are shown in green.

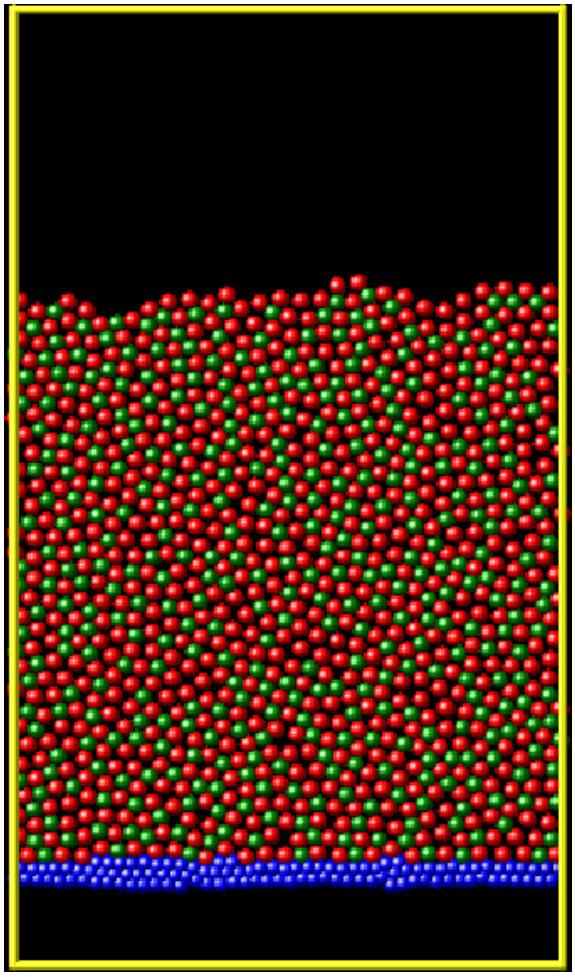

Figure 4.12: A sample liquid cooled configuration generated using $t_{cool} = 1.4 \times 10^1 \tau_\alpha$ taken at $T = 0.25 T_g$. This film is among our less stable configurations. Type A particles are shown in red while type B particles are shown in green.

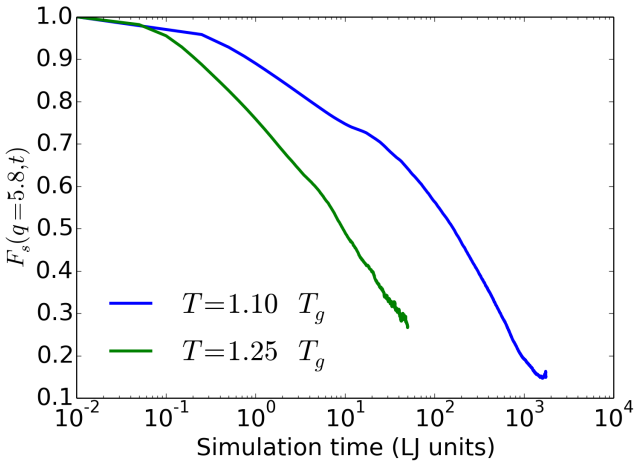

Figure 4.13: Self-intermediate scattering function for 2D films at $T = 1.1T_g$ and $T = 1.25T_g$ calculated with $q = 5.8$, as determined from the static structure factor. τ_α is taken to be where the value of the self-intermediate scattering function decays to $1/e$. We normalize all simulation times by τ_α taken at $T = 1.1T_g$, 370 Lennard-Jones time units.

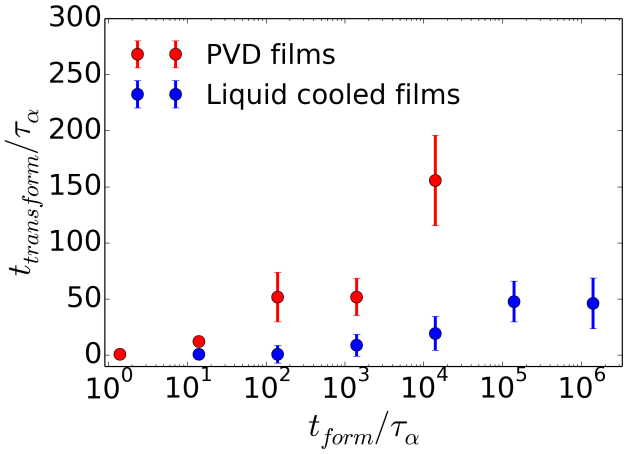

Figure 4.14: Transformation times of PVD and liquid-cooled films measured at $T = 1.1T_g$. Transformation times are normalized by τ_α measured at $T = 1.1T_g$. The characteristic formation time of the films, t_{form}, refers to t_{dep} for PVD films and t_{cool} for liquid-cooled films. Error bars represent standard deviations of transformation times.

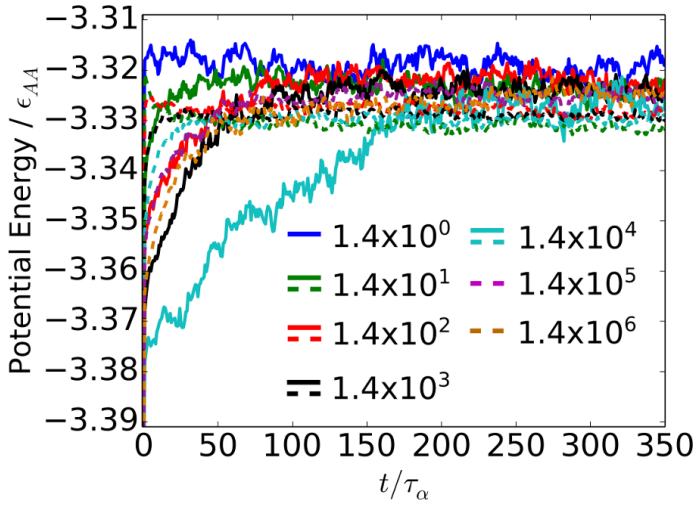

Figure 4.15: Potential energy vs. time for films which have been quickly heated to $1.1T_g$. Energies are used to calculate film transformation times shown in Figure 4.14. Dashed lines represent liquid cooled data while solid lines represent vapor deposited data. Legend values refer to t_{cool} or t_{dep} for a given data set, in units of τ_α (calculated at $T = 1.10T_g$). The transformation time is defined to be when the film has moved 90% of the way from its initial energy to its equilibrium energy. This is a two stage melting process. In the first stage, which we observe here, locally ordered structures melt. In the second, film composition will re-equilibrate given the new temperature. As described in the main text, the composition of these films is not uniform, and can depend on formation method and rate. Thus energies after the first stage of melting are not all precisely equal.

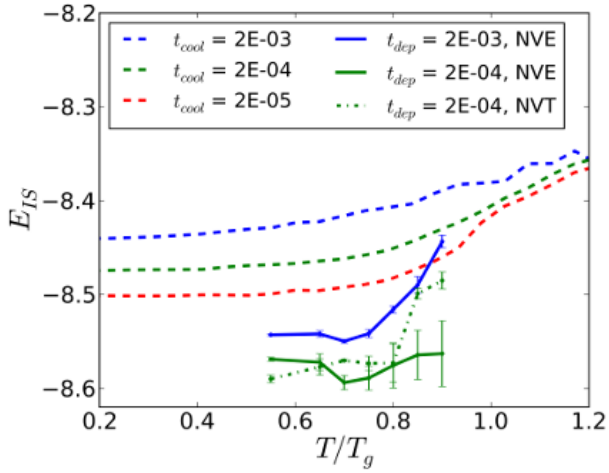

Figure 4.16: Inherent structural energies for liquid cooled, NVE deposited, and NVT deposited films for 3D glass films. We find that NVE deposition is at least as efficient as NVT in 3D as well. We use the standard 3D Kob-Andersen model, with $\chi = 0.8$, and deposit at several rates and substrate temperatures. Figure XX shows that NVE energies are at least as low as in NVT Dashed lines represent liquid cooled films, solid lines represent PVD films formed with NVE deposition, which dotted lines represent PVD films formed with NVT deposition. The data shows that both NVE and NVT deposition produce highly stable films. The data also shows that NVE deposition is at least as effective as NVT, making it a preferable method as it is more physically realistic. Error bars represent standard error. The cooling or deposition rate is represented by γ, which is in Lennard-Jones units.

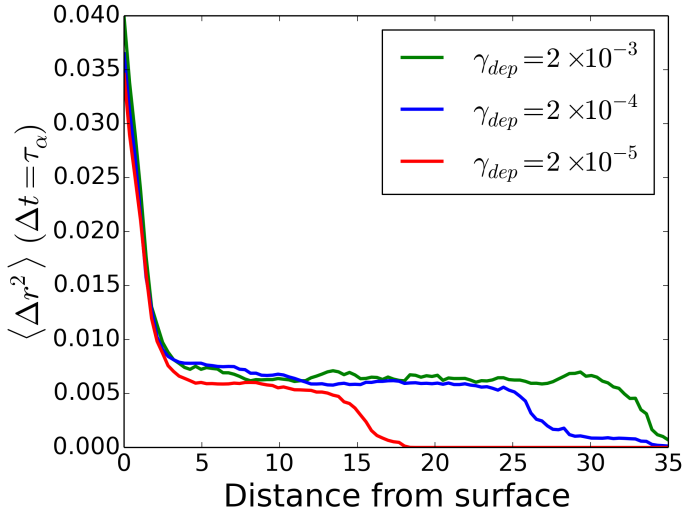

Figure 4.17: Mobility data for 3D PVD films formed at several deposition rates with $T_s = 0.8T_g$. Films formed with slower deposition rates are more stable and show slightly lower mobilities. The deposition rate is labeled as γ_{dep}. Note that the films formed with $\gamma_{dep} = 2.0 \times 10^{-5}$ are thinner than others, thus the data does not extend as far from the surface.

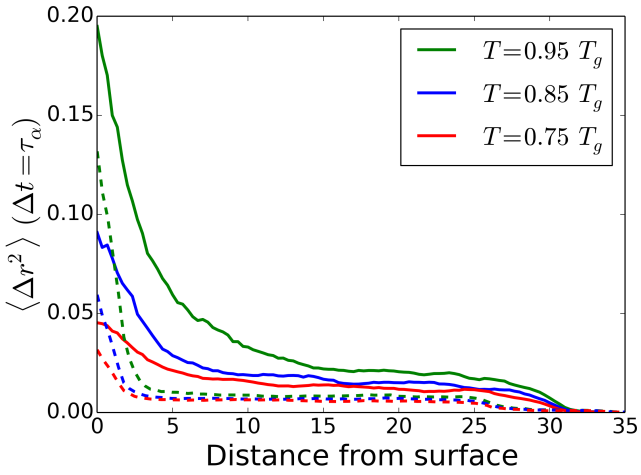

Figure 4.18: Mobility data for 2D and 3D PVD films equilibrated at several temperatures, all formed using NVE deposition at $t_{dep} = 1.4 \times 10^1 \tau_\alpha$, which corresponds to roughly the same growth rate for both types of films when growth rates are normalized by τ_α. Dashed lines represent 3D films, while solid represent 2D films. The fraction of species A, A = 0.65, 0.80 and $T_g = 0.21$, 0.335 in 2D and 3D, respectively. $< r^2 >$ is measured for $\Delta t = \tau_\alpha$. As temperature increases, the mobile layer extends further into the film. At the same multiple of T_g, the mobile layer in 2D always extends further. At this deposition rate, the growth rate of 2D and 3D films are nearly equal.

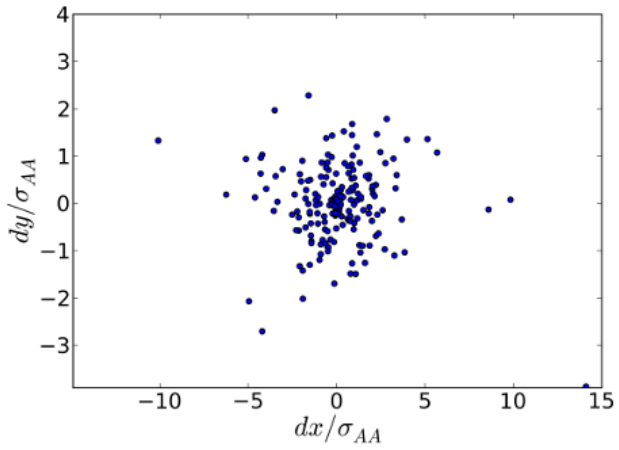

Figure 4.19: Change in x and y from vapor atoms' position at initial touchdown and cooling to their position once 300 more atoms have been deposited and the tracked atoms have been glassified. Values shown are for type A atoms only. Films are formed using $t_{dep} = 1.4{\times}10^4\tau_\alpha$.

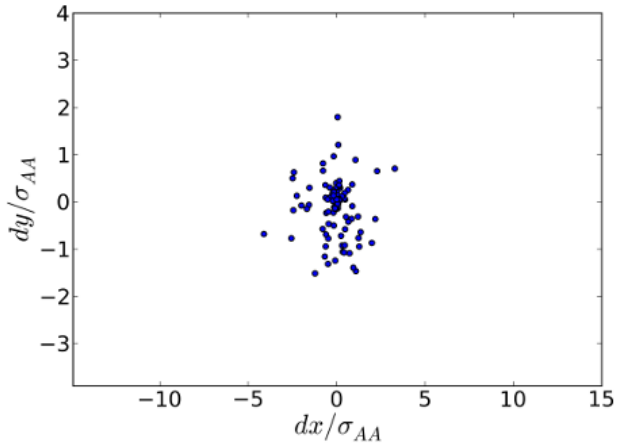

Figure 4.20: Change in x and y from vapor atoms' position at initial touchdown and cooling to their position once 300 more atoms have been deposited and the tracked atoms have been glassified. Values shown are for type B atoms only. Films are formed using $t_{dep} = 1.4{\times}10^4\tau_\alpha$.

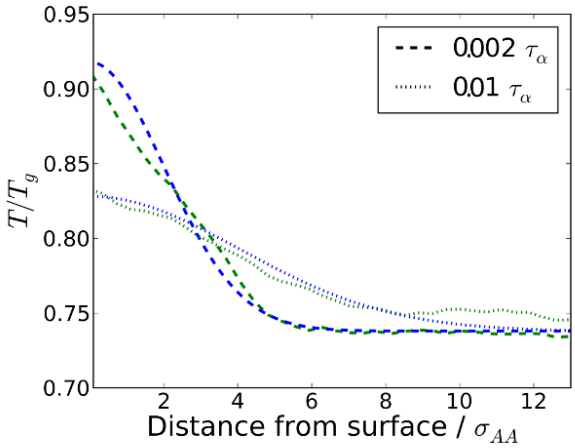

Figure 4.21: Temperature profile for PVD films shortly after the impact of many vapors, and a 1-dimensional model which mimics a PVD film where heat only transfers by diffusion. PVD film data are shown in green while data from the continuum model are shown in blue. In contrast to material presented in the main text, where the impact of only one atom was considered, here we consider the impact of many atoms. As a result, the continuum results are recovered.

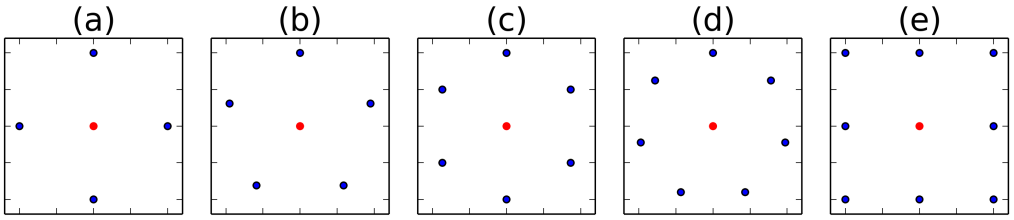

	(a)	(b)	(c)	(d)	(e)
q_5	0	0.701	0	0	0.415
q_8	64.0	0.273	3.79	0.273	64.0

Figure 4.22: Several sample configurations for which the q_5 and q_8 order parameters are calculated. The q parameters are calculated for the red center atoms of each configuration. Note that the q order parameters are based on spherical harmonics and thus depend only on the angle between the red center atom and each neighbor. Thus configurations such as an octagon and a square represented by 8 points as shown in (e) are equivalent. Also included are calculated q5 and q_8 values for configurations (a) through (e). q5 selects strongly for 5-fold symmetry (b) and weakly for 8-fold symmetry (e). The cutoff we use for high q5 order is above the q5 value for an 8-fold symmetric configuration as shown in (e). The q_8 parameter selected strongly for 4 and 8-fold symmetry, and very weakly for other symmetries.

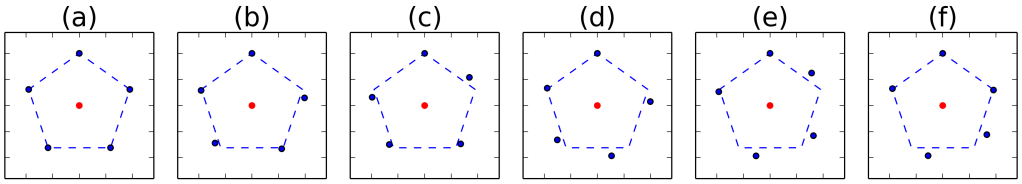

	(a)	(b)	(c)	(d)	(e)	(f)
q_5	0.71	0.65	0.60	0.55	0.50	0.45
q_8	0.00	23.4	44.7	16.7	21.5	16.5

Figure 4.23: Several sample configurations for which the q_5 and q_8 order parameters are calculated. The calculated values are shown in the associated table. The blue dashed line represents a perfect pentagon. The q parameters are calculated for the red center atoms of each configuration. The configurations range from a perfect pentagon (a) which yields a maximum q_5 value to configurations which yield lower q_5 values. While these configurations are representative, they are by no means the only configurations which yield these values. The configurations were generated by starting with a perfect pentagon and randomly rotating points around the center until the desired q5 value was reached. Panel (d) represents a q_5 value of 0.55, that used as a cutoff in the main work.

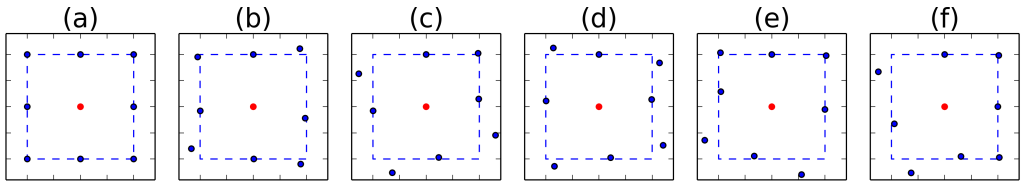

	(a)	(b)	(c)	(d)	(e)	(f)
q_5	0.00	0.22	0.09	0.16	0.14	0.14
q_8	64.0	40.0	30.0	24.0	22.0	20.0

Figure 4.24: Several sample configurations for which the q_5 and q_8 order parameters are calculated. The calculated values are shown in the associated table. The blue dashed line represents a perfect square, which yields a maximum q_8 value. The q parameters are calculated for the red center atoms of each configuration. The configurations range from a perfect square (a) which yields a maximum q_8 value to configurations which yield lower q_8 values. The configurations were generated by starting with a perfect square and randomly rotating points around the center until the desired q_8 value was reached. Panel (e) represents a q_8 value of 22, that was used as a cutoff in the main work. Note that while many of these configurations appear similar to the eye, different cutoffs can distinguish between varying degrees of order. For example, increasing the high-order q_8 cutoff from that used for (e) to that used for (d) significantly decreases the fraction of high-order atoms, as can be seen comparing Figure 4.9 in the main work to Figures 4.28 and 4.25 in the Supplementary Information.

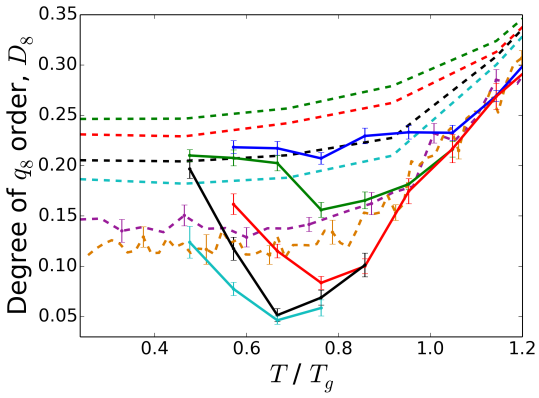

Figure 4.25: Fraction of highly q_8 ordered atoms for vapor deposited and liquid cooled films. Solid lines represent vapor deposited films, while dashed lines represent liquid cooled. The color of each line represents the rate at which its films were formed, as described in the main text. The data here was generated using a q_8 cutoff value of 24, rather than 22 as in the main text.

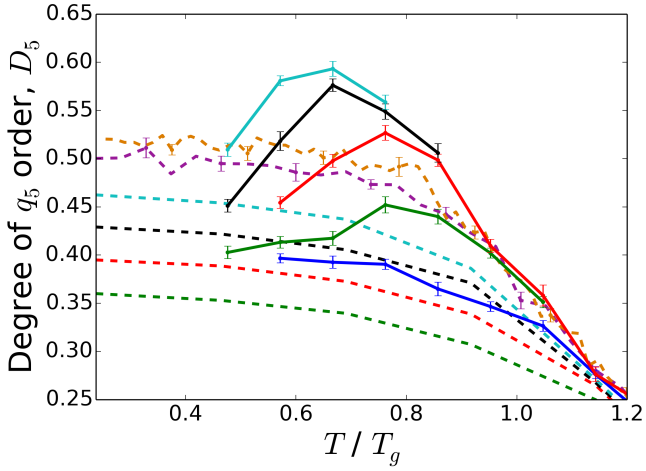

Figure 4.26: Fraction of highly q_5 ordered atoms for vapor deposited and liquid cooled films. Solid lines represent vapor deposited films, while dashed lines represent liquid cooled. The color of each line represents the rate at which its films were formed, as described in the main text. The data here was generated using a q_5 cutoff value of 0.60, rather than 0.55 as in the main text.

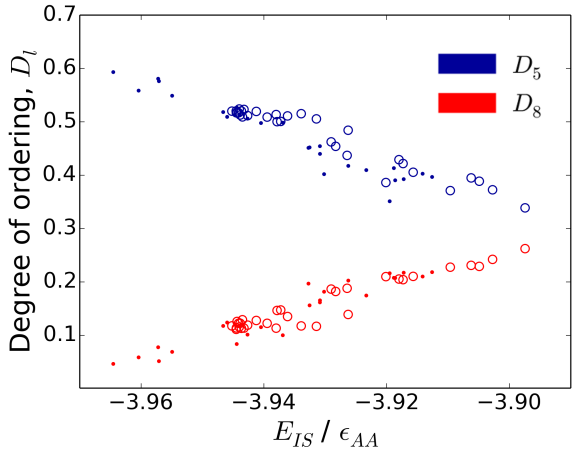

Figure 4.27: Degree of q_5 and q_8 ordering, D_l, for vapor deposited and liquid cooled thin films vs. inherent structural energy, E_{IS}. Solid circles represent vapor deposited data while open circles represent liquid cooled data. Films used are identical to those used in the main text. This data uses the high crystallinity thresholds as shown in Figures 4.25 and 4.26.

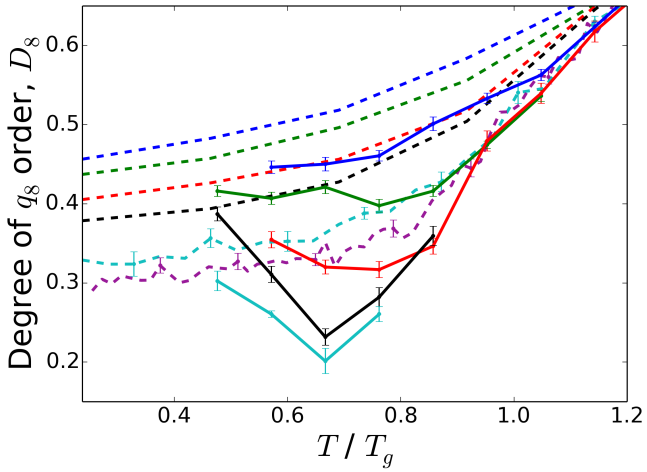

Figure 4.28: Fraction of highly q_8 ordered atoms for vapor deposited and liquid cooled films. Solid lines represent vapor deposited films, while dashed lines represent liquid cooled. The color of each line represents the rate at which its films were formed, as described in the main text. The data here was generated using a q_8 cutoff value of 20, rather than 22 as in the main text.

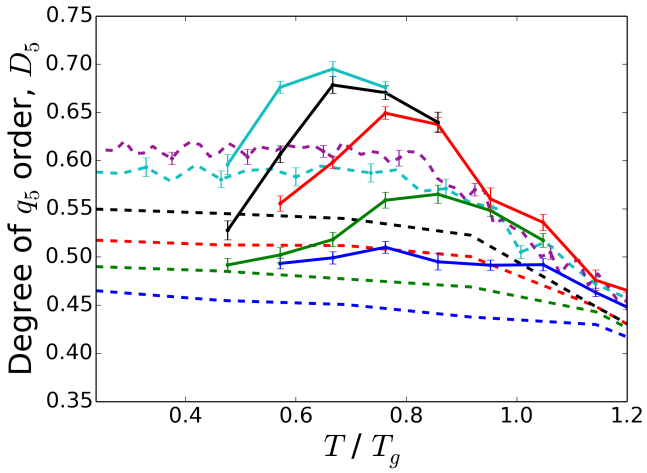

Figure 4.29: Fraction of highly q_5 ordered atoms for vapor deposited and liquid cooled films. Solid lines represent vapor deposited films, while dashed lines represent liquid cooled. The color of each line represents the rate at which its films were formed, as described in the main text. The data here was generated using a q_5 cutoff value of 0.50, rather than 0.55 as in the main text.

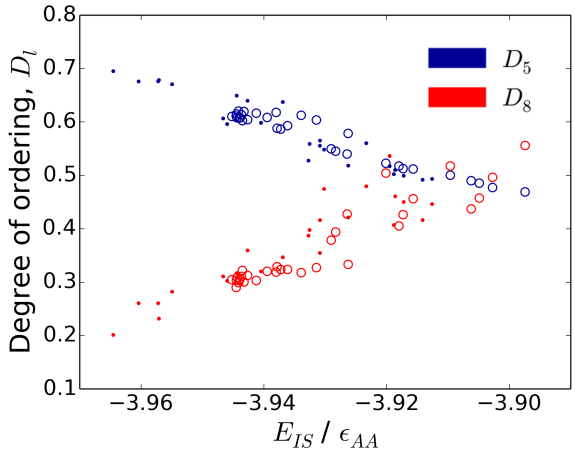

Figure 4.30: Degree of q_5 and q_8 ordering, D_l, for vapor deposited and liquid cooled thin films vs. inherent structural energy, E_{IS}. Solid circles represent vapor deposited data while open circles represent liquid cooled data. Films used are identical to those used in the main text. This data uses the high crystallinity thresholds as shown in Figures 4.25 and 4.26.

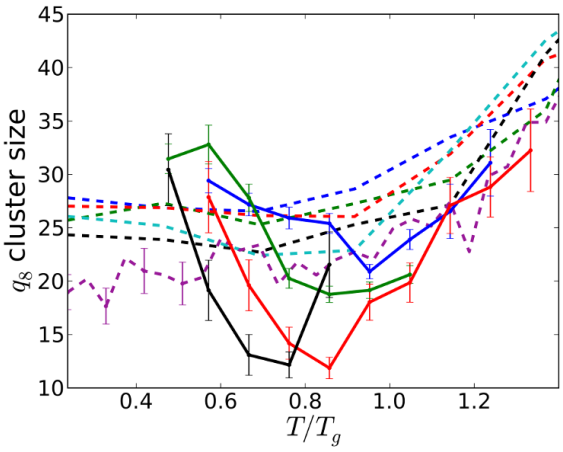

Figure 4.31: Average size of q_8 high-order clusters for liquid cooled and vapor deposited films as discussed in the main text. Cluster size is reported in number of atoms. Dashed lines represent liquid-cooled data while solid lines represent vapor deposited data. We find that ordered q_8 domains grow smaller with film stability and decreasing D8. The noise in this data is due to the low number of q_8 clusters found in each sample. The data shows that the q_8 cluster sizes for vapor deposited and liquid-cooled films are roughly equivalent for films of equal energy. Error bars represents 95% confidence intervals. As films become very stable, they show so few q_8 clusters that the data become noisy. Thus, cluster size data for our most stable films is not included.

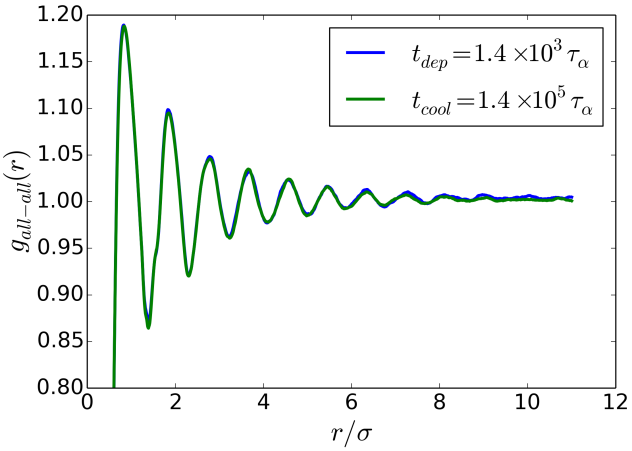

Figure 4.32: Radial distribution function for all-all in liquid cooled films formed with $t_{cool} = 1.4 \times 10^5 \tau_\alpha$ at $T = 0.16$ and PVD films formed with $t_{dep} = 1.4 \times 10^3 \tau_\alpha$ with $T_s = 0.16$.

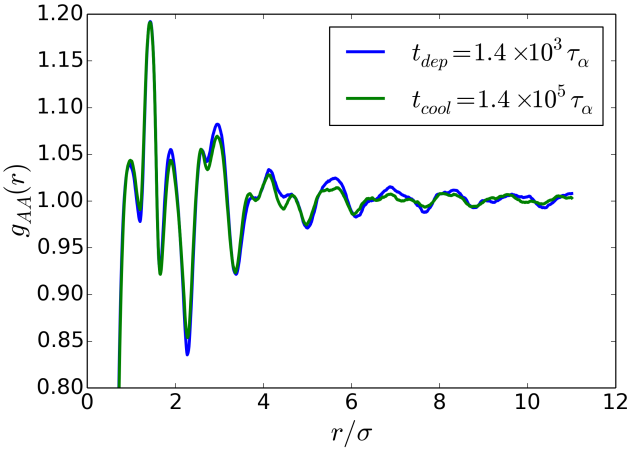

Figure 4.33: Radial distribution function for A-A in liquid cooled films formed with $t_{cool} = 1.4e5\tau_\alpha$ at $T = 0.16$ and PVD films formed with $t_{dep} = 1.4 \times 10^3 \tau_\alpha$ with $T_s = 0.16$.

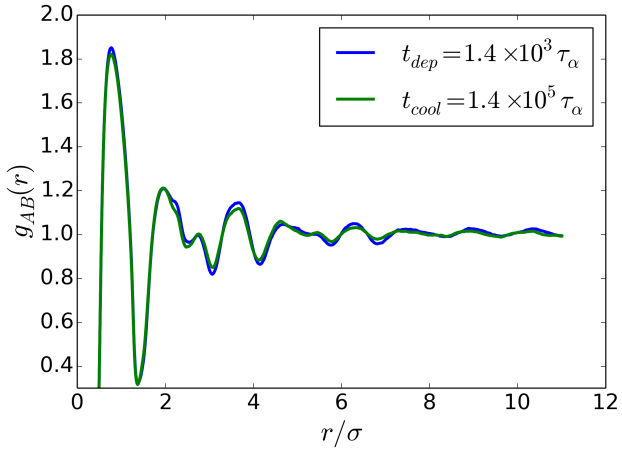

Figure 4.34: Radial distribution function for A-B in liquid cooled films formed with $t_{cool} = 1.4e5\tau_\alpha$ at $T = 0.16$ and PVD films formed with $t_{dep} = 1.4 \times 10^3\tau_\alpha$ with $T_s = 0.16$.

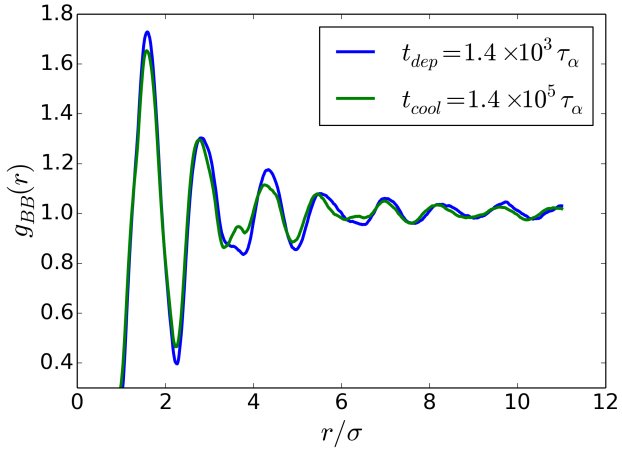

Figure 4.35: Radial distribution function for B-B in liquid cooled films formed with $t_{cool} = 1.4e5\tau_\alpha$ at $T = 0.16$ and PVD films formed with $t_{dep} = 1.4 \times 10^3\tau_\alpha$ with $T_s = 0.16$.

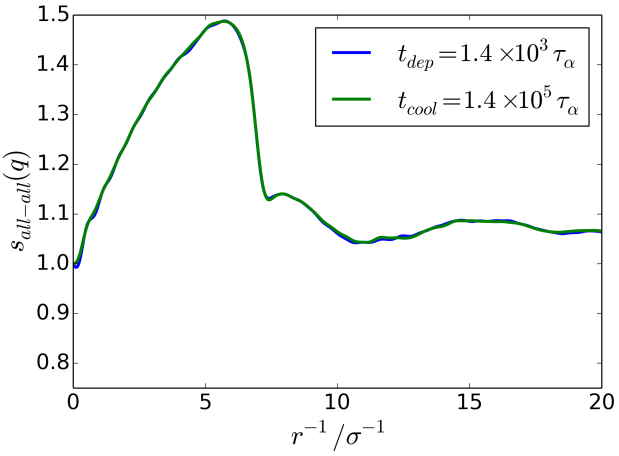

Figure 4.36: Structure factor for all-all in liquid cooled films formed with $t_{cool} = 1.4e5\tau_\alpha$ at $T = 0.16$ and PVD films formed with $t_{dep} = 1.4 \times 10^3\tau_\alpha$ with $T_s = 0.16$.

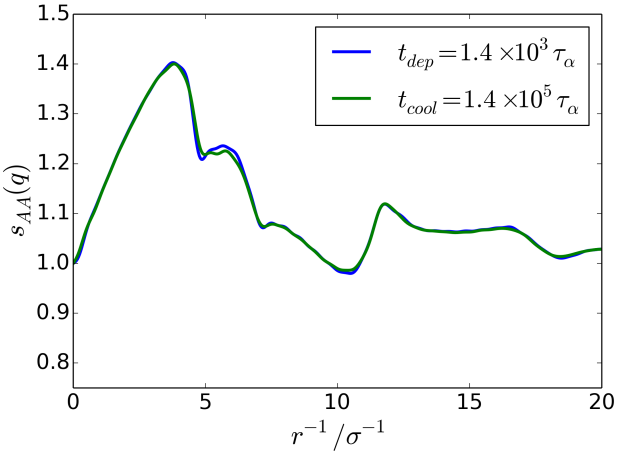

Figure 4.37: Structure factor for A-A in liquid cooled films formed with $t_{cool} = 1.4e5\tau_\alpha$ at $T = 0.16$ and PVD films formed with $t_{dep} = 1.4 \times 10^3\tau_\alpha$ with $T_s = 0.16$.

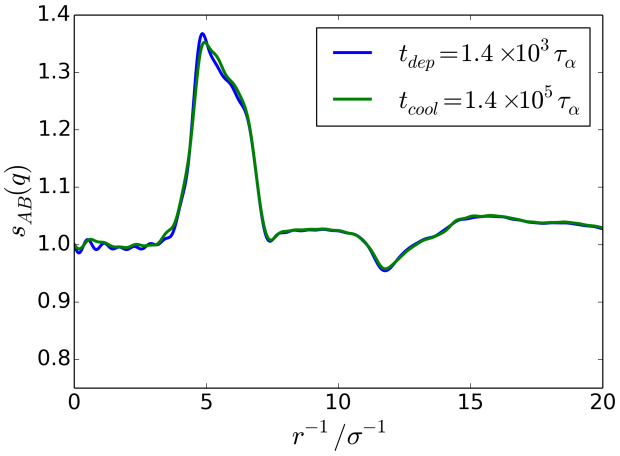

Figure 4.38: Structure factor for A-B in liquid cooled films formed with $t_{cool} = 1.4e5\tau_\alpha$ at $T = 0.16$ and PVD films formed with $t_{dep} = 1.4 \times 10^3\tau_\alpha$ with $T_s = 0.16$.

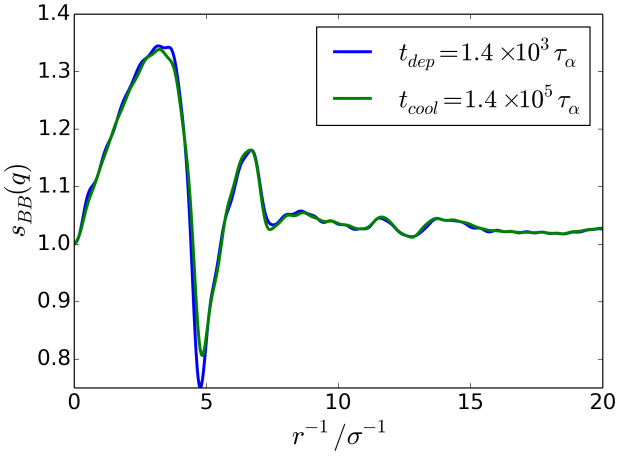

Figure 4.39: Structure factor for B-B in liquid cooled films formed with $t_{cool} = 1.4e5\tau_\alpha$ at $T = 0.16$ and PVD films formed with $t_{dep} = 1.4 \times 10^3\tau_\alpha$ with $T_s = 0.16$.

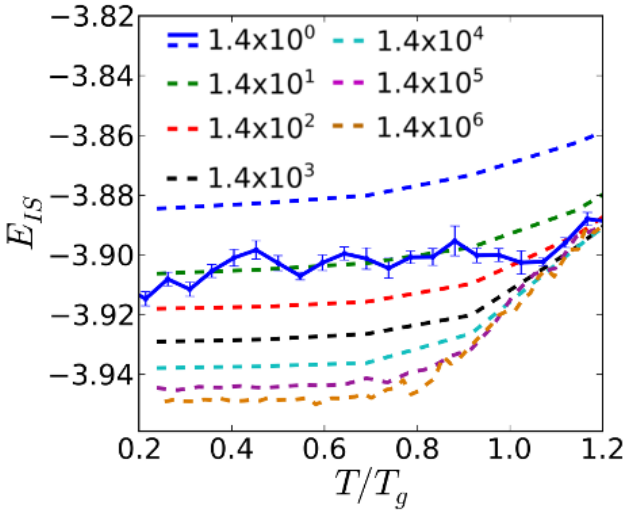

Figure 4.40: Inherent structural energies for liquid cooled and NVT deposited 2D films. Dotted lines represent liquid cooled energies and solid lines represent vapor deposited. All conditions in these simulations are identical to those done in the main work except for the deposition style. Films produced by NVT deposition are significantly less stable than those produced by NVE deposition. NVT deposition in 2D also fails to show an ideal substrate temperature as is shown in both experiment and NVE deposition. Previous work has employed thermostats to control the temperature of the substrate, film, and newly added atoms, with new atoms being cooled linearly to the film temperature (NVT deposition). In this work, a thermostat is only applied to the substrate, which acts as a heat bath for the rest of the film, which has no thermostat applied to it (NVE deposition).

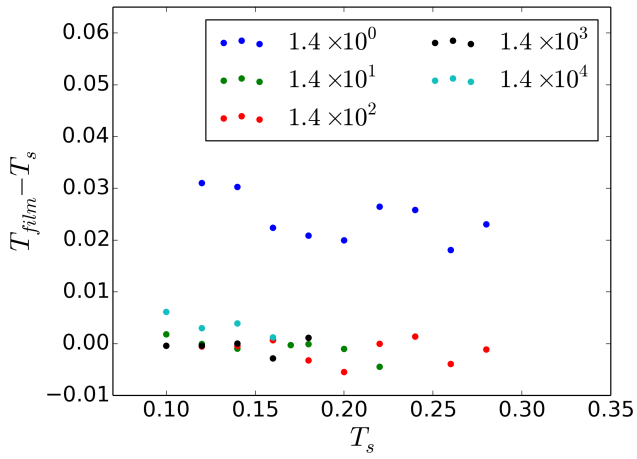

Figure 4.41: Deviation of film temperatures from substrate temperatures for all deposition rates and substrate temperatures. Legend values refer to t_{dep} in units of τ_α measured at $T = 1.10T_g$. The deviation occurs due to the heat from vapor atoms. Heat is absorbed by the substrate, which is held under at constant temperature. If deposition occurs quickly, a temperature gradient through the film occurs. Each point represents the average of the instantaneous temperature of ten 35 σ thick films. At equilibrium, the temperatures of the film and substrate will be equal to within thermal fluctuations. However if vapor atoms are added too rapidly, the film temperature could deviate from that of the substrate. For films deposited with $t_{dep} = 1.4 \times 10^0 \tau_\alpha$, T_{film} was used for all calculations. For all other deposition rates, T_s was used in calculations.

t_{dep}/τ_α	T_s/T_g	t_{cool}/τ_α
1.4×10^{0}	0.87	1.5×10^{2}
1.4×10^{1}	0.79	4.0×10^{3}
1.4×10^{2}	0.73	1.4×10^{5}
1.4×10^{3}	0.70	4.7×10^{7}
1.4×10^{4}	0.68	1.5×10^{10}

Table 4.1: Predicted liquid cooling time required to form films with energy equal to vapor deposited samples deposited with ideal substrate temperature. Predicted liquid cooling rates are calculated using Equation 4.1. Ideal substrate temperatures are found by fitting a cubic spline to E_{IS} vs. T_s at a given t_{dep} using data shown in Figure 4.3.

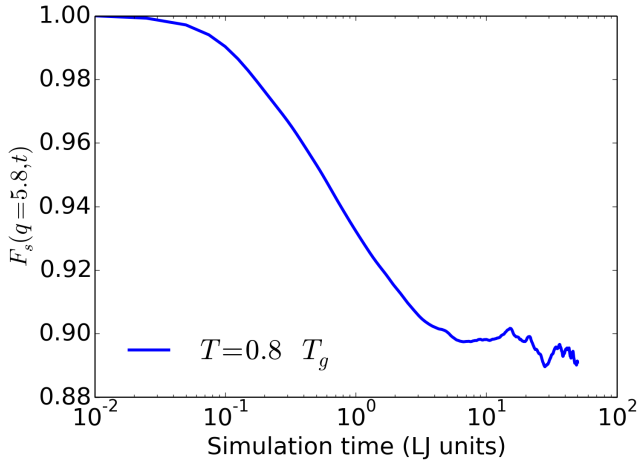

Figure 4.42: Self-intermediate scattering function for 2D films at $T = 0.8T_g$ calculated with $q = 5.8$, as determined from the static structure factor. We use data from this figure to estimate the in-cage relaxation time, τ_β, which is used to time-average positions for analysis of local order. The time must be at least long enough for particles to sample configurations within the local cage. For this reason, we use the time where the scattering function has fully decayed to its plateau value, 10 Lennard-Jones time units.

CHAPTER 5

AGGREGATION AND SOLUBILITY OF A MODEL CONJUGATED DONOR-ACCEPTOR POLYMER

5.1 Introduction

In thin-film organic semiconductors, specifically bulk-heterojunction organic photovoltaic (OPV) cells[83, 84], the film morphology is exceedingly complex[85]. The inability to control morphologies of organic semiconductors (OSC) is perceived as a limiting step in the successful commercialization of these materials [86]. While some OSC exhibit glass transition temperatures (T_g) below room temperature[87], many have T_g's significantly above 298K[88, 89, 90] and exist in kinetically trapped, glassy morphologies. As solution-deposition is the most common processing route for many OSC, solution-phase conformations may be kinetically trapped into the deposited film morphology.

Evidence has emerged indicating that solution-phase polymer conformations influence the morphology of solution-deposited thin-films[91, 92, 93, 94, 95, 96, 97, 98, 99, 100, 101]. Increases in OSC performance have been obtained via solution-deposition at high temperatures[102] or in poor solvents[103, 104, 105], suggesting that control over solution-phase aggregation phenomena can improve device performance. Many OSC materials aggregate in solution, as even relatively good solvents are not "good" in the traditional Flory definition[106]. Indeed, even for short oligomeric chains, optical studies have revealed the occurrence of single-chain folding in oligomers above a critical molecular weight;[107, 108] in test systems, the enthalpic contributions to similar processes have been quantified[109]. Side-chain engineering has proven a powerful avenue for manipulating solubilities of conjugated polymers, with branched versions of common alkylic side-chains often improving solubility relative to that of chemically equivalent linear side-chains.[110]

Molecular modeling is used here to shed light on the solution-phase conformations of conjugated polymers. While experimental methods can be applied to assess general aggregation

trends,[111, 112, 113] molecular simulations can describe the atomistic structure of the aggregates that give rise to complex optoelectronic phenomena. We emphasize that in recent studies, atomistic[114, 115, 116, 117, 118, 119] and coarse-grained[120, 121, 122] simulations have broached the topic of solution-phase conformations of conjugated polymers. However, an understanding of the thermodynamic contributions to conjugated polymer solubility, and their potential chemical manipulation, is lacking.

In this letter we examine the conformations and solubilities of the common OPV polymer PTB7 in explicit solvents, and determine the mechanisms by which side chain structure influences these essential properties. To assess solubility, we determine the free energy change upon aggregation of a pair of PTB7 oligomers. We validate this approach by comparing free energies to experimental solubilities and find general agreement for a series of common solvents. Results are also validated against aggregation of longer oligomer chains. Once validated, we employ this approach to study the solubility of three side chain variants of PTB7: branched (2-ethylhexyl), linear (octyl), and cleaved (methyl). We find that side chains disrupt the stacking of conjugated polymer backbones, and in the case of branched side chains, enhance solubility. However, the enhanced solubility is not directly related to the disrupted backbone structure, but rather the destabilization of the solvent associated with the more disordered, bulky structure. These results provide both an experimentally-validated framework for screening conjugated polymer solubility and a means of understanding the structural origin of solubility in conjugated materials.

5.2 Results

5.2.1 Solubilities in a variety of solvents

Three common solvents/additives are studied: chlorobenzene (CB), chloronapthalene (CN), and diiodooctane (DIO). Our approach, based on dimer formation, captures three key contributions to the Flory-Huggins χ parameter: solute-solute, solute-solvent, and solvent-solvent

interactions. The details of the procedure are provided in the Methods but, to summarize: Pairs of PTB7 stacked oligomers are solvated. Dimers of PTB7 are used, which are long enough to show strong stacking motifs. Steered molecular dynamics is performed to generate initial configurations for free energy sampling, which is performed using replica exchange umbrella sampling, measuring the free energy with respect to the center-of-mass (COM) separation of the two conjugated PTB7 backbones.

Calculated free energies of aggregation (ΔA) are shown in Figure 5.1, where r is the COM separation, n is the degree of polymerization, and L_c is the contour length. Free-energies are normalized by the degree of polymerization (n). PTB7 in CB and CN shows a shallow free energy basin with a minimum of ≈ -8.4 kJ/mol-n, whereas in DIO it exhibits a deeper basin of ≈ -25.1 kJ/mol-n. The deeper free energy basin in DIO indicates that DIO is a worse solvent than both CB and CN. Experimentally determined solubilities for PTB7 in CB, CN, and DIO are (¿75, ¿75 and ¡0.1) mg/mL, respectively. It was not feasible to determine exact solubilities, and solutions with high concentrations of PTB7 were opaque and gel-like. Despite this, experiments clearly differentiate between good and poor solvents, and simulations are in agreement. The two free-energy minima of Figure 5.1 present at $r/L_c \approx 0.5$ and $r/L_c \approx 0.05$ correspond to the oligomers having one or both, respectively, of their monomers stacked with the other oligomer. This suggests that PTB7 oligomers (dis)aggregate via a sliding process, rather than a rotationally isotropic approach. Visual examination of trajectories as shown in Supplementary Information supports this hypothesis.

5.2.2 Single chain properties

To ensure that dimers capture simulated polymer solubilities more broadly, we study the structure of PTB7 10-mers in CB, CN, and DIO. Ten-mers are initialized in a self-folded state and are run for 100 ns at 300 K. Three replicates are run for each solvent. Aggregates unfold in good solvents and remain folded in poor solvents. The 10-mers in CB unfold at 4, 10, and 53 ns. Two of three 10-mers in CN unfold at 13 and 40 ns, while the third remains

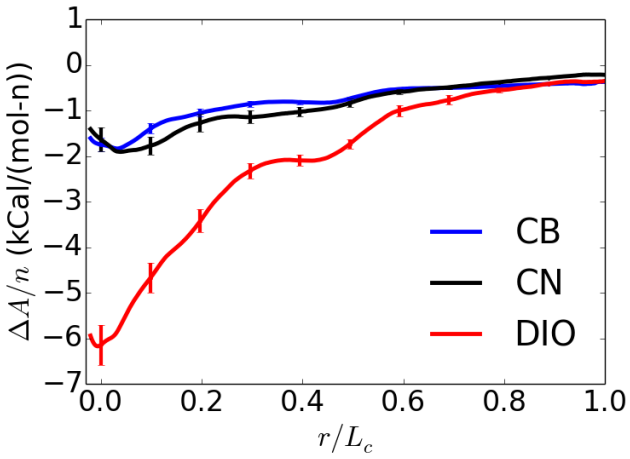

Figure 5.1: Free-energy vs COM separation of two PTB7 oligomers with 2-ethylhexyl side-chains in CB, CN, and DIO. Free-energy is normalized by the degree of polymerization (n) and the COM separation (r) by oligomer contour length (L_c). Poor solvents yield more stable aggregated states, corresponding to low values of ΔA at $r/L_c \approx 0$.

folded. All 10-mers in DIO remain folded. These results are consistent with solubility trends from dimer simulations. From configurations which unfold, persistence lengths of PTB7 are calculated to be 4.3 nm and 4.1 nm in CB and CN, respectively, using a simple worm-like chain model[123]. To further validate these results, small angle neutron scattering measurements were performed on low molar mass PTB7 ($\approx$ 35 kg/mol) in d^5-CB. From these measurements, the persistence length was determined via a flexible cylinder model to be 5 ± 1 nm at 298 K, which is in good agreement with our calculated value, particularly since the persistence length is expected to be larger for higher molar masses. These results suggest that dimers capture the relevant polymer behavior to predict solubilities.

Solubility parameters can also be computationally determined as explained in the Supporting Information; however, they fail to capture experimental solubility trends.

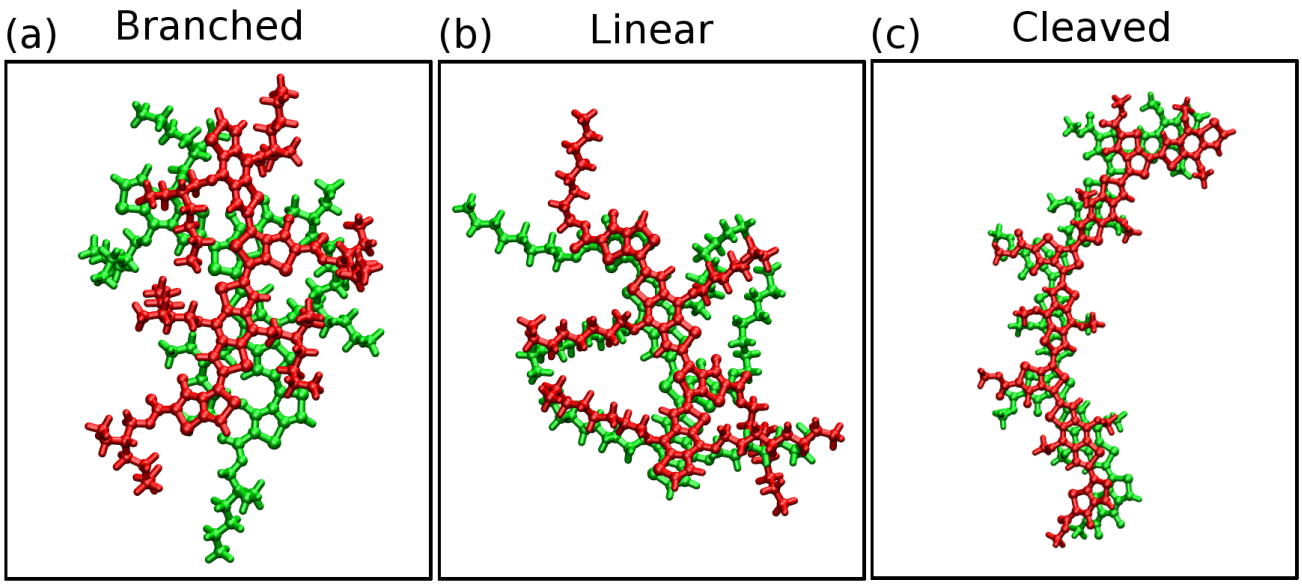

Figure 5.2: Representative configurations of PTB7 aggregates with (a) branched (2-ethylhexyl), (b) linear (octyl), and (c) cleaved (methyl) side-chains. The aggregate with branched sidechains is poorly stacked while tgat with linear or cleaved sidechains is well-stacked. These behaviors are quantified through average backbone stacking energies of $\Delta U = -58$, -71, and -88 kJ/mol-n for a), b), and c) respectively.

5.2.3 Modifying polymer architecture

Having established that free energy calculations qualitatively predict solubility, we examine the mechanisms by which PTB7 sidechains might be varied to control solubility and aggregation. To that end, PTB7 is studied in explicit CB solvent with three different types of side-chains: branched, linear, and cleaved. The branched and linear variants are chosen to conserve carbon atoms (2-ethylhexyl/octyl). Representative snapshots of the polymer architectures are shown in Figure 5.2. Dimers are used for branched and linear variants, while 4-mers are used for those with cleaved side chains. These degrees of polymerization ensure that the aggregate shows an aligned and stacked structure, as would be seen in a larger polymer.

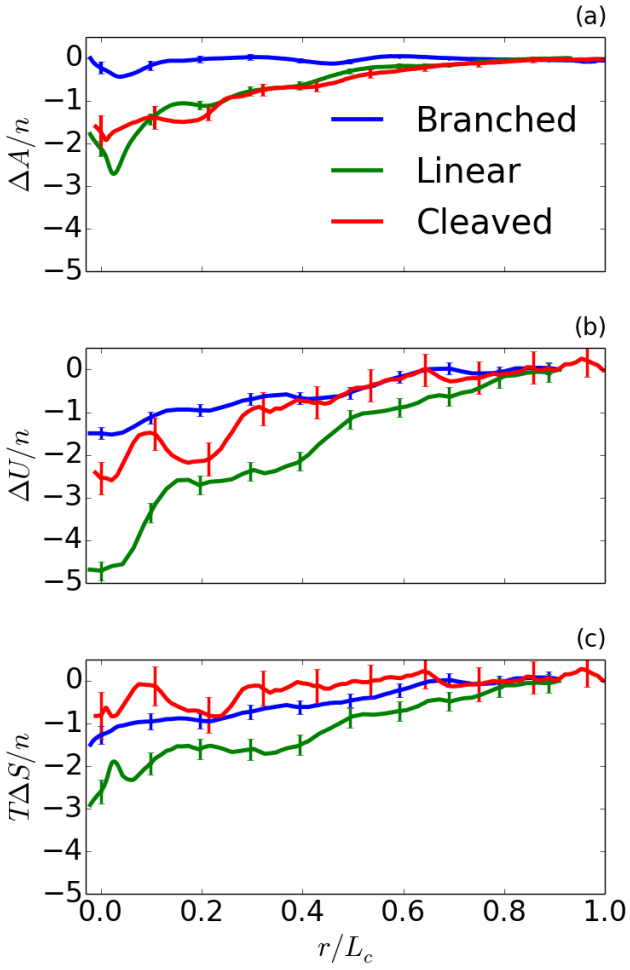

Figure 5.3: a) Free energy b) potential energy and c) entropy vs scaled COM separation r/L_c of two PTB7 oligomers with three variants of side-chains in explicit CB solvent. All energies are normalized by the degree of polymerization (n).

The free energies of aggregation for the side chain variants are shown in Figure 5.3 a). The free energy minima suggest that the structures with linear and cleaved side chains also aggregate via a sliding mechanism. Branched PTB7 is more soluble than that with linear side chains, as demonstrated by the 8.4 kJ/mol-n difference in the depth of the free energy basin. This phenomenon is commonly observed in experiments[110], accounting for the proliferation of polymer architectures with branched side chains. Curiously, the PTB7 cleaved side-chain oligomer shows a free energy basin that is nearly identical to that of the variant with linear side chains. This goes against the intuition that the addition of side chains reliably increases solubility.

5.2.4 Understand energetic contributions

To quantify how side chain structure influences solubility, the free energies of aggregation are decomposed into enthalpic and entropic contributions in Figure 5.3 b) and c), respectively. The linear sidechain variant is the most enthalpically stable, and also shows the lowest entropy, suggesting an ordered aggregate, which is corroborated by Figure 5.2 b). The branched side chain variant differs, showing the highest enthalpy and the second lowest entropy. The cleaved side chain variant, on the other hand, shows the highest entropy. This is likely due to the side chain degrees of freedom being reduced upon aggregation, which does not occur in the cleaved side-chain case. The backbone stacking energy for the three side-chain variants suggests that this entropic difference is not due to backbone stacking disorder ($\Delta U = -88$ kJ/mol-n vs -58 and -71 for branched and linear, respectively).

Entropic contributions can be attributed to backbone and side chain disorder, however enthalpic contributions require more study. Figure 5.4 a) partitions ΔU into polymer-polymer interactions shown in solid lines and solvent interactions shown in dashed lines. The negative of the solvent interaction energy is shown. The variant without side chains shows the smallest ΔU for both types of interactions, as it has the fewest atoms. Interestingly, ΔU of

polymer-polymer interactions is strongest for oligomers with branched side chains, despite showing the highest system ΔU. Two features must be explored: first, why do polymers with branched side chains aggregate more favorably, and second, how do these stable branched side chain aggregates lead to a less stable system overall?

The favorable polymer-polymer interactions are not explained by enhanced backbone stacking interactions. Figure 5.4 b) shows backbone-backbone energies for the three PTB7 variants, demonstrating that side chains disrupt backbone stacking. The data show that cleaved, linear, and branched side chains destabilize aggregates from least to greatest, respectively. These backbone energies do not correlate with polymer-polymer energy, suggesting that while side chains disrupt π-stacking, they are not directly responsible for the change in solubility.

Figure 5.4 c) demonstrates that the enhanced stabilization of oligomers with branched side chains originates from strong sidechain-backbone interactions. With the backbone stacking disrupted, the branched architecture of the side chain can associate freely with the backbone, resulting in the highly stable oligomer aggregate.

We now examine solvent energies in Figure 5.4 d). Solid lines depict the ΔU of polymer-solvent interaction energy and in dashed lines the ΔU of solvent-solvent interaction energy. The data show that aggregates with branched side chains interact least favorably with the solvent, despite having the same number of atoms as those with linear side chains. This energetic contribution is largely responsible for destabilizing the system of aggregated PTB7 with branched side chains. We therefore suggest that the more disordered aggregation motifs caused by the branched side chain structures create a less favorable interaction surface for the solvent, which plays a crucial role in determining solubility.

Taken together, these results unveil the intricate behavior of solubility in complex organic molecules. While dogma has long held that branched side chains increase solubility by disrupting backbone stacking, we propose a more subtle picture. While side chains do disrupt

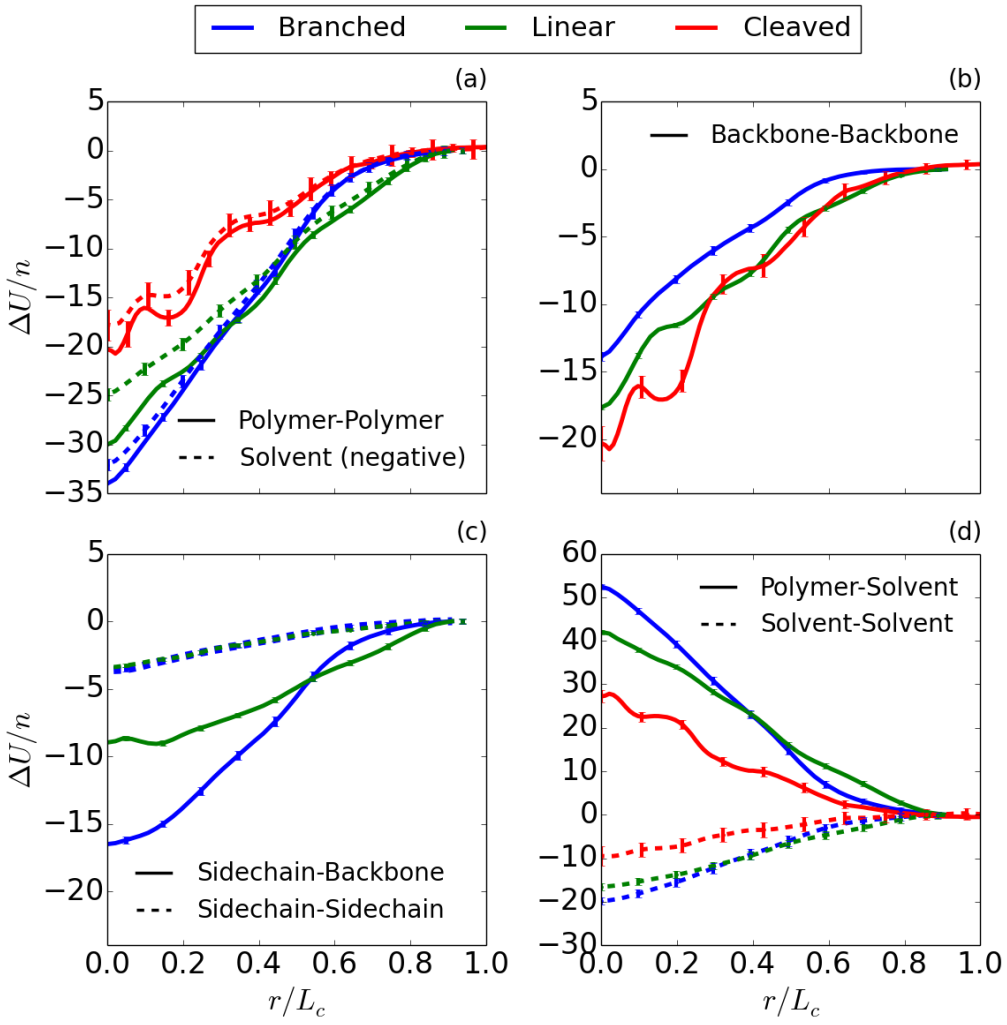

Figure 5.4: Potential energy (ΔU) contributions of the three PTB7 variants. For all panels, blue, green and red data sets refer to branched, linear, and cleaved sidechain structures. a) ΔU of polymer-polymer interactions (solid lines) and the *negative* sum of solvent-polymer and solvent-solvent interactions (dashed lines). The difference between these two is the total ΔU of the system. b) ΔU of interactions between conjugated oligomer backbones. Results indicate that sidechains disrupt backbone stacking. c) ΔU of sidechain-backbone (solid lines) and sidechain-sidechain (dashed lines) interactions. d) ΔU of polymer-solvent (solid lines) and solvent-solvent (dashed lines) interactions. 95% confidence intervals are shown.

backbone stacking, this does not directly lead to increased solubility. In fact, aggregates with more complex side chains are more stable in the absence of solvent. Rather, the side chains' effect on solvent interactions dominate the enthalpic contribution to the free energy of aggregation. Entropic contributions can be understood through the lens of side chain-induced disorder, however these interactions are relatively small compared to the enthalpic contribution. To design materials with higher solubility, we suggest that new designs should include side chains that maximize polymer disorder to the extent that it disrupts solvent structure.

5.3 Methods

Simulations utilize the opls-aa force-field for explicit solvent[124], and an opls-style atomistic force-field for PTB7 recently parameterized in the literature[114]. Simulations employ the GPU code DASH[125]. A Lennard Jones interaction cutoff of 1 nm was used for all simulations. Coulombic interactions in the solubility parameter simulations used the damped shifted force with a cutoff of 1.2 nm. Coulombic interactions in the free-energy simulations used a short-range cutoff of 1.2 nm and the particle-particle-particle-mesh formalism for long-range interactions. The Nose-Hoover thermostat was used, with a time constant of 200 fs. Details of the free energy sampling are given in Supplementary Information.

5.3.1 Experimental Solubilities

Saturated solutions were prepared by mixing an excess of PTB7 with a small volume of each test solvent, (200 to 300)μL, and stirring for 24 h at room temperature. The saturate was filtered from the solution using a 0.45 μm PTFE filter and diluted in ortho-dichlorobenzene (oDCB) to achieve an optical density suitable for ultraviolet-visible (UV-Vis) absorption measurement. Measurements were performed at room temperature using a PerkinElmer Lambda 950 UV/Vis spectrometer.[126] Absorbance was compared to a set of standard

curves with known concentrations of PTB7 in oDCB.

5.3.2 Measurement of Persistence Length

Small angle neutron scattering (SANS) measurements were performed at the NIST Center for Neutron Research (NCNR) on the NG7 SANS instrument, and data were reduced and fit to a flexible cylinder model using software described elsewhere.[127, 128] Detailed information is provided in the Supporting Information.

5.4 Appendix

5.4.1 Free Energy Sampling

Simulations of the dimer aggregate are initialized at low density and equilibrated at 1 atm with dimers held in a stacked configuration. The collective variable sampled is the distance between the conjugated backbone center of mass for each oligomer. Steered MD is performed in SSAGES to generate snapshots required to initialize free energy sampling [129]. Free energy sampling is performed using replica exchange umbrella sampling, also with SSAGES. Umbrella sampling windows are placed from 3.0 Å to the oligomer contour length at intervals of 0.5 Å. A harmonic restraint potential of k=3 kCal/mol is used, and exchanges between neighboring replicas are proposed every 1 ps. 16 independent replicates are average for each curve, and each replica exchange window is sampled for a total of 3 ns, totaling 1.9 μs of simulation time for the shortest oligomers. A weighted histogram analysis method[130] is used to compute the free-energy surfaces of Figures 5.1 and 5.3.

5.4.2 Computational Solubility Parameters

Solubility parameters are calculated using an approach in line with previous work[131, 132], in which Equation 5.1 is directly evaluated. In the expression of Eq. 5.1, $E_{x,vap}$ and $E_{x,liq}$ are the molar potential energy contribution of x (dispersive or electrostatic potentials) in

	δ_{lit}	δ_{sim}	$\delta_{d,sim}$	$\delta_{e,sim}$	R_a	$s_{PTB7}(\frac{mg}{mL})$
PTB7		18.0	17.5	4.3	N/A	
CB	19.6[133]	19.8	19.3	4.4	3.7	> 75
DIO	18.8[133]	19.6	19.5	1.7	4.8	< 0.1
CN	20.7[133]	20.9	20.4	4.3	5.8	> 75
oDCB	20.5[134]	20.9	20.1	5.8	5.5	
Toluene	18.2[134]	18.7	18.1	4.9	1.3	

Table 5.1: Calculated solubility parameters as compared to literature, with R_a values for PTB7 and each solvent. Literature values of the Hildebrand parameter from experiment and group theory contribution are listed in column δ_{lit}. Value for DIO is calculated from group contribution theory while the remainder are determined experimentally, Values of the Hildebrand parameter as calculated in simulation are given in column δ_{sim}. δ_{sim} is decomposed into two Hansen-like solubility parameters, δ_d and δ_e, which represent dispersive and electrostatic cohesive energy densities. R_a is calculated as the geometric distance between PTB7 and each other solvent's solubility parameters. Absolute solubilities s_{PTB7} were determined as described in the text.

the vapor and liquid phases, respectively, and V_m is the molar volume of the pure solute. $E_{x,vap}$ is measured by equilibrating a single molecule in vacuum and measuring the average potential energy contribution of x. $E_{x,liq}$ is measured by equilibrating a liquid of the molecule and measuring the separate dispersive and electrostatic components. All simulations are maintained at 300 K and 1 atm, with data taken over the course of 5 ns for both liquid and vapor simulations. To measure V_m the molar volume of PTB7, a box of 80 PTB7 dimers are equilibrated at 1 atm for 5 ns, and the appropriate potential energies are measured.

$$\delta_x = \sqrt{\frac{E_{x,vap} - E_{x,liq}}{V_m}} \tag{5.1}$$

$$\delta = \sqrt{\delta_d^2 + \delta_e^2} \tag{5.2}$$

To assess the validity of this approach, we compute the solubility parameters of PTB7, CB, DIO, CN, oDCB, and toluene, and compare them to experimental values found in the literature (Table 5.4.2). Solubility parameters are computed as described in Methods.

Computed solubility parameters accurately reproduce experimentally observed Hildebrand parameters. The prediction for DIO, on the other hand, is significantly different, possibly because the value from literature is calculated from group contribution methods rather than experiment[133]. To test the ability of classical force-fields to predict the solubility parameters of conjugated polymers, PTB7's solubility parameters, $\delta_{d,sim}$ and electrostatic $\delta_{e,sim}$, are computed. To assess the accuracy of PTB7's solubility parameters, we have compute the solubility radius (R_a) of PTB7 in CB, CN, oDCB, Toluene and DIO. It is clear from Table 5.4.2 that the computed solubility radii do not accuracy describe the trends in solubility observed experimentally. Because of this generally poor performance, we adopt a more sophisticated atomistic simulation methodology to understand the structure and aggregation of PTB7 in explicit solvents. We note that this has no impact on the utility of experimentally derived solubility parameters, which have recently been applied successfully to organic semiconducting materials[135, 136, 137].

5.4.3 Small Angle Neutron Scattering (SANS) Data and Fit Results

All measurements were performed under dark conditions due to reports in the literature suggesting that the radius of gyration of a semiconducting polymer chain is reduced in the presence of illumination.[138]. Data reduction and correction to absolute intensity was performed using the NCNR macros[127] in IgorPro.[126] Measurements were performed on a special grade of PTB7 obtained from 1-Material with a manufacturer's estimated molar mass of (25 to 50) kg/mol at a concentration of 2 mg/mL in d^5-chlorobenzene. Measurements were made at 298 K and 308 K. Reduced data for the two temperatures were simultaneously fit (with the contour length and contour length polydispersity constrained to be equal for the two samples) to a flexible cylinder model in SasView using the DiffeRential Evolution Adaptive Metropolis algorithm (DREAM) fitting engine.[128]SANS Data and the fits using the flexible cylinder model for PTB7 in d^5-chlorobenzene (d^5-CB) are shown in Figure 5.5. The fit results are given in Table 5.2 below. From the contour length, the molar mass was

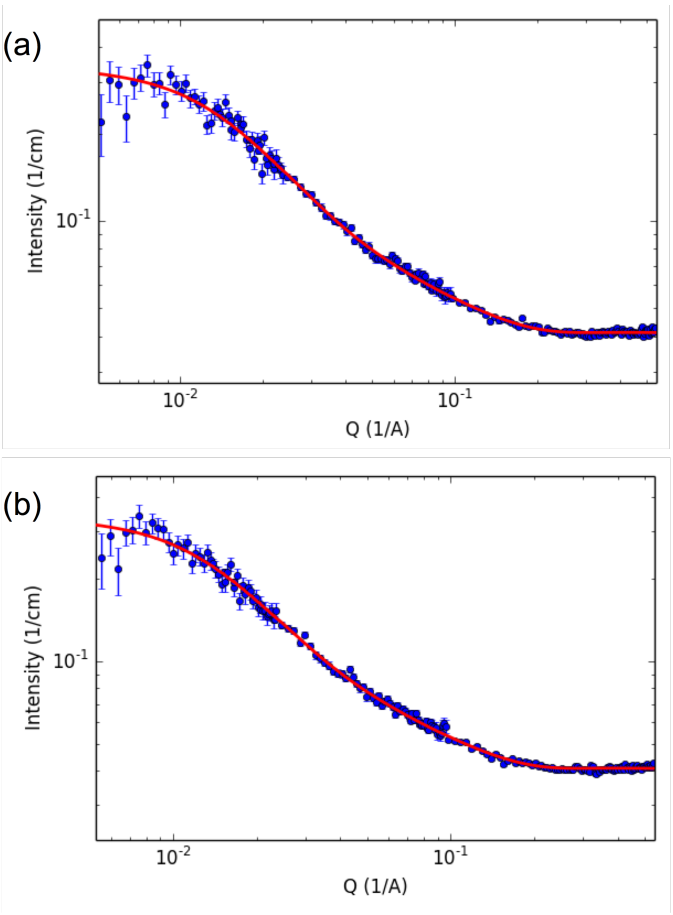

Figure 5.5: SANS Data for PTB7 in d^5-chlorobenzene (2 mg/mL) at a) 298 K and b) 308 K. Lines correspond to the best fit to the flexible cylinder model. Error bars correspond to one standard deviation in the experimental uncertainty.

estimated to be $\approx$ 35 kg/mol, which falls well within the range provided by the manufacturer - further validating the fits. The persistence length (l_p) was computed from the Kuhn length (l_k) through the following relationship: l_p=l_k/2.

Table 5.2: Parameters obtained from fits to SANS data with the flexible cylinder model. SLD is the polymer scattering length density fit parameter (not corrected by sample concentration), Radius is the cylinder radius, l_k is the Kuhn length, T is the temperature, and L_c and P.D. are the contour length and contour length polydispersities, respectively, which were forced to be equal for both fits. The scattering length density for the solvent was set to 4.909×10^{-6} as determined from the NCNR scattering length density calculator.

T (K)	L_c (nm)	l_k (nm)	$P.D.$ ratio	Radius (nm)	SLD 10^{-6} (Å)	Background (cm^{-1})
298	48 ± 2	10 ± 1	0.5 ± 0.2	1.32 ± 0.03	4.802 ± 0.002	0.041109 ± 0.00008
308		11 ± 2		1.37 ± 0.03	4.806 ± 0.002	0.040773 ± 0.00008

CHAPTER 6

MOLECULAR-LEVEL CHARACTERIZATION OF ORGANIC PHOTOVOLTAIC INTERFACES USING NMR-INFORMED SIMULATION TECHNIQUES

6.1 Introduction

In thin-film organic semiconductors, specifically bulk-heterojunction organic photovoltaics (OPVs) cells[83, 84], the development of rigorous processing-structure-function models is impaired by challenges in structural characterization techniques. While a variety of techniques exist to characterize organic electronics, few produce a molecular-level understanding of film structure. For example, electronic microscopy cannot distinguish between organic phases of similar electron density[139], a common trait in organic electronics. Scattering curves can yield ambiguous interpretations as there is typically not a unique fitting model. To address this and other issues, we introduce a new materials characterization technique which combines rotational-echo double-resonance (REDOR) NMR with molecular simulation to yield a molecular-level perspective of the bulk heterojunction in organic photovoltaics.

In recent years, REDOR NMR has emerged as a powerful technique to characterize distances between atoms with non-zero nuclear spins[140]. This technique, which measures dipolar coupling between such nuclei, has been applied widely to characterize various crystalline and molecular structures, for example in inorganic compounds[141, 142] or small organic molecules[143, 144, 145, 146]. Dipolar coupling decays with inverse distance cubed, making this technique a sensitive reporter to particle distances. More recently, this technique has been applied to the organic photovoltaic blend of electron donor poly(3-hexyl thiophene) (P3HT) and electron acceptor phenyl-C61-butyric acid methyl ester (PCBM), to study the interfacial structure within these complex devices [147]. For this system, ^{13}C -detect ^{2}H -dephase REDOR NMR is employed, where for P3HT the beta-hydrogens are 2H enriched,

and for PCBM the fullerene cage is isotopically enriched to roughly 18% ^{13}C . These modifications create dipolar couplings which relate to the distances between atoms in P3HT and PCBM, and thus to bulk phase separation and interfacial structure.

To relate REDOR measurement to physically meaningful quantities, however, the signal must be mapped to an atomic configuration. This is a daunting task, as the problem is underdetermined. In addition, rigorously calculating REDOR signals from atomic configurations is exceedingly computationally intensive[147]. Recently, approximations have been developed which allow for REDOR NMR measurements to be computed as a relatively straightforward closed-form function of atomic coordinates[147, 148, 149]. These new functional forms open the door for molecular simulation to perform this crucial mapping and uncover the molecular-level structure of organic photovoltaics.

Here, we introduce techniques to generate large-scale simulations which show specified REDOR NMR signals. Using a representative coarse-grained model, we first show that while a REDOR NMR signal does correspond to many distinct configurations, when prepared properly these configurations are indistinguishable when one studies their phase separation and interfacial behavior. We then use the techniques developed to study with atomistic models the P3HT/PCBM bulk heterojunctions which show a variety of REDOR NMR signals, including those formed in experiment. Finally, we use this technique to study the free energy of phase separation within the P3HT/PCBM system, with application to experimental formation processes. Importantly, these techniques bypass the standard timescale limitations of molecular dynamics[150, 151] by directly biasing simulations to show experimentally-relevant configurations. Taken together, this work lays out a framework for generating experimentally relevant bulk heterojunction configurations and investigating the underlying free energy surface of complex amorphous mixtures.

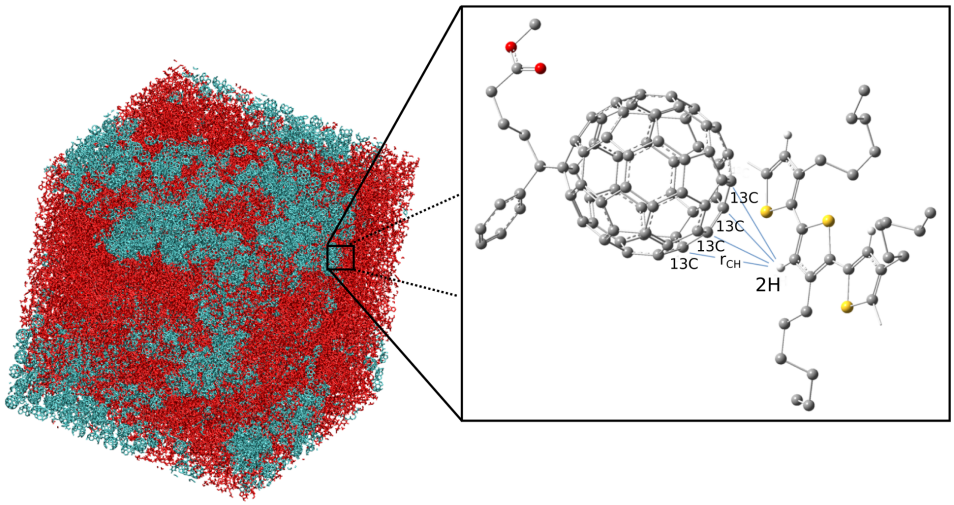

Figure 6.1: Diagram of REDOR biasing technique. On left is shown a fully-formed P3HT/PC61BM bulk heterojunction with P3HT shown in red and PC61BM in teal. This system has been biased to show an experimental REDOR signal. At right is shown a zoomed-in P3HT-PCBM pair. The single ^{2}H atom on each P3HT monomer interacts with the ^{13}C enriched fullerene cage of the PC61BM. The distances between the pairs of atoms, r_{CH}, are used in equation 6.1 to calculate the REDOR signal and apply biasing forces.

6.2 REDOR Simulation Technique

REDOR NMR is employed to study phase separation in complex organic photovoltaic materials. PC61BM is synthesized such that the fullerence cage consists of 18% ^{13}C atoms, while P3HT is synthesized with ^{2}H in the beta position. These resulting couplings between ^{2}H and ^{13}C atoms yield a REDOR signal which corresponds to interfacial structure and phase separation, with fast signal decay corresponding to smaller ^{2}H - ^{13}C distances on average, or more mixing of the two components, and slow signal decay corresponding to larger ^{2}H - ^{13}C distances on average, or less mixing. A diagram depicting a bulk heterojunction with ^{2}H - ^{13}C couplings highlighted is shown in Figure 6.1.

Recent work has demonstrated that straightforward functional forms can accurately approximate REDOR NMR signals[147]. These functional forms are closed form expressions of the relevant atoms' coordinates - those with non-zero nuclear spin. Here we briefly outline the functional forms developed by Nieuwendaal. Equation 6.1 gives the form of the dipolar

coupling, where μ_0 is the permeability of free space, the two values of γ are the gyromagnetic ratios of the two species, in this case 2H and 13C, and r_{ij} is the distance between the two atoms. Equation 6.2 describes the REDOR signal as a function of dephasing time (t) given by a single 2H/13C spin pair. A single ^{13}C with multiple ^{2}H neighbors yields the functional form given by Equation 6.3. The entire sample gives a signal which is simply the average of that given by each ^{13}C , as shown in Equation 6.4. To bias simulations to match experimental REDOR measurements, an external potential is introduced to the system as shown in Equation 6.5. A biasing force is applied to each atom given by $F_i = -\frac{\partial E}{\partial r_i}$ where i represents the i^{th} particle.

$$D_{ij}(t) = -\frac{\mu_0}{4\pi}\frac{\gamma_1\gamma_2\hbar}{r_{ij}^3} \tag{6.1}$$

$$Y_{C_iH_j}(t) = 0.67\Big(1 - exp(-(ktD_{ij})^2)\Big) \tag{6.2}$$

$$Y_{C_i}(t) = 1 - \prod_{j\in neigh}(1 - Y_{C_iH_j}(t)) \tag{6.3}$$

$$\frac{\Delta S}{S_0}(t) = \overline{Y_C(t)} \tag{6.4}$$

$$E = \sum_{t\in times} k_p\left(\frac{\Delta S}{S_0}_{exp}(t) - \frac{\Delta S}{S_0}_{sim}(t)\right)^2 \tag{6.5}$$

6.3 Results and Discussion

6.3.1 Coarse grained polymer model

The process of mapping a handful of experimental REDOR data points to a large simulation consisting of thousands of particles is a highly underdetermined problem. Here, we show that while this problem is underdetermined, a particular REDOR signal yields a unique set

a structural characteristics that is robust to a variety of material formation techniques. To demonstrate the uniqueness of the REDOR measurements, we use a coarse grained molecular dynamics model consisting of a mixture single bead molecules and bead-spring polymers with a glass transition temperature (T_g) = 26K for the 50/50 particle mass fraction used here, where each particle has a mass of 1. The Lennard-Jones parameters between the bead (a) and chain (b) types are for σ in Å: (a-a, 3), (a-b, 2.25), (b-b, 1.5) and ϵ in kCal/mol: (a-a, 0.12), (a-b, 0.096), (b-b, 0.06). The parameters are chosen to inhibit crystallization. These two molecules are analogous to PCBM and P3HT, which are used for experimental and simulation work later in the text. Bead and polymer systems are initialized in four distinct configurations: completely mixed (mixed), phase separated with polymer initialized within a sphere surrounded by beads (separated), phase separated with polymer formed in a single periodic cylinder (cylinder), and phase separated with polymer formed in four evenly spaced cylinders (multi cylinder). Simulations are initialized in these four configurations at a range of temperatures and then biased to values of $\Delta S/S_0$ corresponding to low, medium, and high degrees of phase separation. Low and high phase separation corresponds to values of $\Delta S/S_0$ reached in fully mixed and fully phase separated configurations. For each configuration, interfacial area between the polymer particles and bead particles is calculated, along with phase purity (ϕ). Here, ϕ is defined as the mean square deviation of local mass composition from the bulk composition. Results are shown in Figure 6.2. As can be seen, at temperatures increase past T_g, samples approach identical values of SA/vol and ϕ regardless of initial configuration. Samples prepared below T_g do not necessarily show the same structural features, indicating that the different systems were unable to relax to structurally similar configurations. Thus, we suggest that if the system of interest is sufficiently mobile, a given REDOR signal yields a unique structure as determined by the metrics studied here.

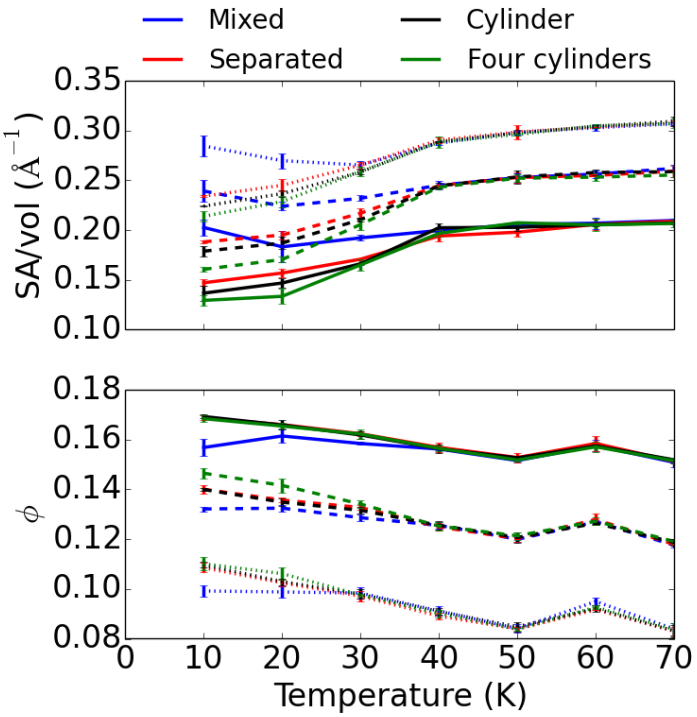

Figure 6.2: Structural metrics calculated for coarse-grained systems which have been initialized in a variety of configurations, then biased towards particular REDOR values. The four colors correspond to different initial structures as defined in the main text: 'mixed', 'separated', 'cylinder', and 'multi cylinder'. These four initial configurations are then biased to three different REDOR values, corresponding to REDOR values which are high (fully mixed, dotted lines), medium (partially mixed, dashed lines), and low (phase separated, solid lines). We then calculate SA/vol of the polymers and beads, and ϕ. As temperature increase past $T_g = 26K$, initial configurations can be biased to structurally indistinguishable final configurations based on the REDOR value, expect in the case of the fully mixed initial configuration.

6.3.2 Organic photovoltaic systems

Having established that a given dephasing curve yields systems with unique structural characteristics when prepared properly, we examine the structural features of the P3HT/PCBM bulk heterojunction. Experimental REDOR measurements are of films which are 50/50 P3HT/PCBM by mass. We create systems in simulation which match these films' experimental REDOR values by applying the external potential as shown in Equation 6.5. Experimental and simulated REDOR signals are shown in Figure 6.3. The REDOR biasing technique produces simulated configurations which closely match experimental REDOR signals. A representative configuration which shows experimental REDOR values is shown in Figure 6.1. Also shown in Figure 6.3 are REDOR data sets for simulations which have been biased to show the minimum and maximum values of $\Delta S/S_0 = 0$ and 1. These values correspond to the least and greatest achievable phase separation, respectively. While the function form of the REDOR signal allows for the values between 0 and 1, the physical constraints of the force field limits the signal to within the bounds seen in Figure 6.3.

6.3.3 Bulk heterojunction analysis

Having created materials which show experimental REDOR signals, as well as those which correspond to minimum and maximum phase separation, we now analyze the structural and composition features which result. To analyze phase purity in these systems, we calculate the local mass fraction of each of the studied systems. Mass fractions are calculated for grid cells with a side length of 1.3 nm, and are shown in Figure 6.4. For films with $\Delta S/S_0 \to 1$ regions with composition near the global value of 50/50 mass fraction appear become dominant. For experiment unannealed and $\Delta S/S_0 \to 0$ configurations, there exist many regions of near-pure P3HT, and small populations of pure PCBM. The values of ϕ for each class of film, along with the purity of each phase is reported in Table 6.1. Here, purity is defined as as the mass

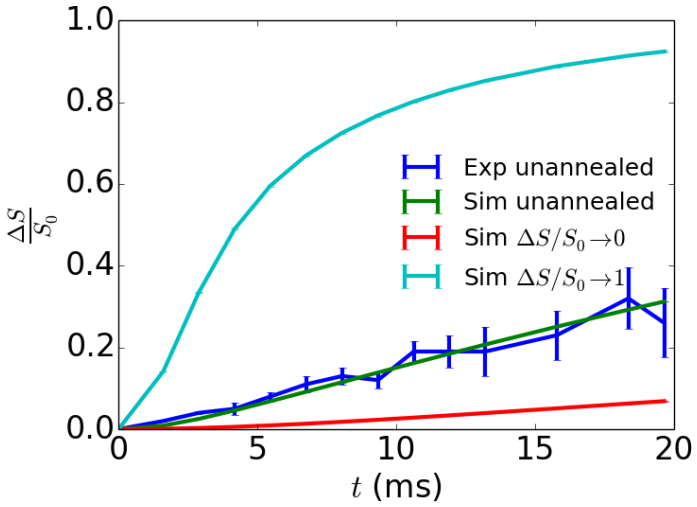

Figure 6.3: Experimental and simulated REDOR curves. The 'Exp unannealed' set shows the experimental REDOR signal for a 50/50 P3HT/PC61BM unannealed blend. The 'Sim unannealed' set shows the REDOR signal from a simulation which has been biased to show experimental REDOR data. The 'Sim $\Delta S/S_0 \to 0$ ' and 'Sim $\Delta S/S_0 \to 1$ ' sets show the REDOR signals of simulations which have been biased to show average $\Delta S/S_0$ values of 0 and 1, respectively. These sets demonstrate range of values which REDOR the signal can physically assume within this system.

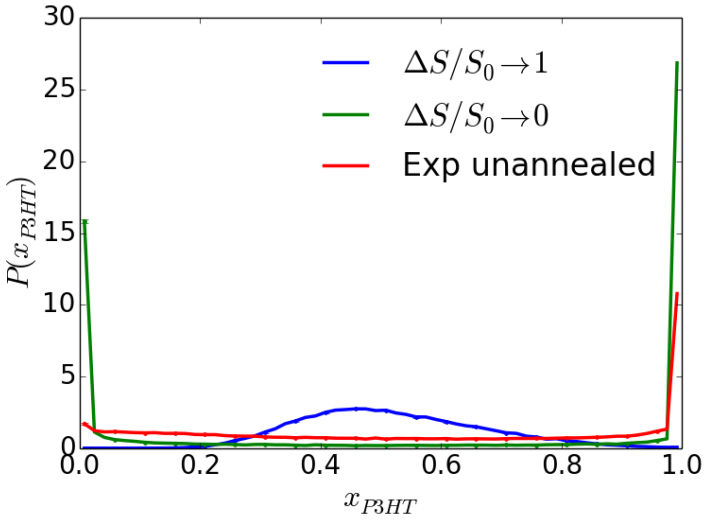

Figure 6.4: Probability distributions of local mass fraction of P3HT for P3HT/PCBM blends biased to different REDOR signals. Mass fractions are computed on a grid with a side length of 1.3nm. Error bars are 95% confidence intervals. Systems are created with a side length of 15nm to allow for large domains to form.

Table 6.1: Interfacial and phase purity statistics for bulk heterojunction simulations formed with particular REDOR values. SA/vol, ϕ, and purity of both P3HT and PC61BM phases are shown.

	$\Delta S/S_0 \to 0$	$\Delta S/S_0 \to 1$	Exp unannealed
SA/vol (Å^{-1})	$0.032 \pm 3.6 \times 10^{-4}$	$0.204 \pm 3.5 \times 10^{-4}$	$0.109 \pm 2.7 \times 10^{-4}$
ϕ	$0.204 \pm 4.2 \times 10^{-4}$	$0.023 \pm 2.1 \times 10^{-4}$	$0.122 \pm 3.8 \times 10^{-4}$
Purity P3HT	$0.933 \pm 1.1 \times 10^{-3}$	$0.651 \pm 6.1 \times 10^{-3}$	$0.841 \pm 1.6 \times 10^{-3}$
Purity PC61BM	$0.949 \pm 6.1 \times 10^{-4}$	$0.581 \pm 9.4 \times 10^{-3}$	$0.780 \pm 3.7 \times 10^{-3}$

fraction of a given component in grid cells where it is in the majority. At maximum phase separation, $\Delta S/S_0 \to 0$, the two phases are nearly pure, with P3HT and PC61BM at 93 and 95% purity, respectively. Note that even for complete phase separation, the calculated purity values will be less than 100% due to grid discretization in the calculation. For experimental films, phase purity for P3HT and PC61BM drop to 84 and 78%. This demonstrates that while experimental films show distinct phases, the domains are far from pure.

6.3.4 Free energies of phase separation

To shed further light on phase separation within the bulk heterojunction, we study the free energy of phase separation. To calculate this quantity we employ two collective variables: $\Delta S/S_0(t = 5.5ms)$ and $\Delta S/S_0(t = 19.6ms)$. We find that using these two REDOR time points as collective variables is sufficient to bias the simulation between the extremes of complete phase separation and complete mixing. We use replica exchange umbrella sampling to perform these calculations. As noted previously, simulations with an applied REDOR bias must be allowed to equilibrate above T_g. As a result, free energies of phase separation are calculated for systems above T_g. Sampling is performed with bins which sweep the diagonal of this two-dimensional collective variable space. Values of $\Delta S/S_0$ $(t = 5.5ms)$ range from 0.01 to 0.35, while those for $\Delta S/S_0$ $(t = 19.6ms)$ range from 0.08 to 0.83. These values were determined by measuring the REDOR signal of systems biased to show $\Delta S/S_0 \rightarrow 0$ and $\Delta S/S_0 \rightarrow 1$ at all time points. Sixty evenly spaced bins are created, linearly interpolating between the low and high bounds for each dephasing time. A restraint strength of $k = 5\ kCal/mol$ is used for each collective variable. The resulting free energy surface is calculated as a function of dephasing times and then re-cast as a function of ϕ.

The results for a system measured at 600K are shown in Figure 6.5. Panel a shows the free energy as a function of the two collective variables: $\Delta S/S_0$ (t=5.5ms) and $\Delta S/S_0$ (t=19.6 ms). To allow for clearer interpretation, the free energy is re-plotted in Panel b as a function of ϕ. The free energy landscape is a single minimum with a depth of roughly 80 kCal/mol from fully mixed or fully phase separated to the equilibrium state. This demonstrates that in an experimental system, there are no significant free energy barriers to reaching the equilibrium state.

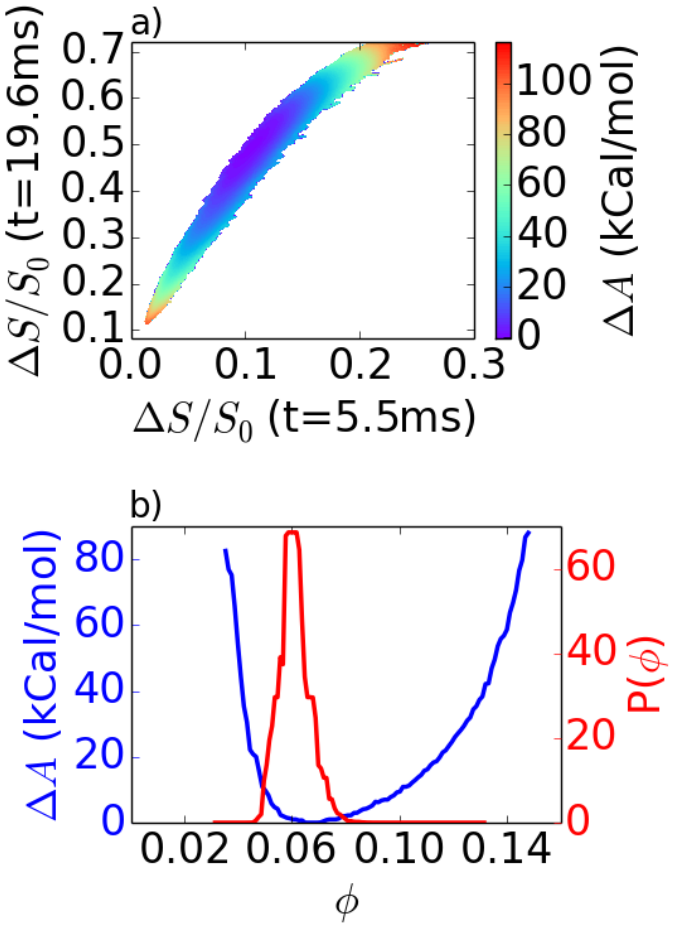

Figure 6.5: Panel a: Free energy with respect to the two sampled collective variables measured at 600K. Panel b: Free energy plotted as a function of phase separation, ϕ along with the probability distribution of ϕ. The free energy surface is smooth, indicating that there are no significant free energy barriers to achieving equilibrium.

CHAPTER 7

DASH - A GPU-ACCELERATED MOLECULAR DYNAMICS ENGINE

7.1 Introduction

In recent years, graphics processing units (GPUs) have come to the forefront of high performance computing[152, 153, 154]. In contrast to central processing units (CPUs) which have relatively few powerful processors, modern GPUs such as the GeForce Titan V contain over 5000 processors. For highly parallelizable problems, the tightly coupled cores on the GPU can yield speedups of 10 times over optimized CPU code executing on a entire node [155, 156, 157]. Molecular dynamics can be effectively parallelized on a per-bead (atom) basis, making it amenable to GPU acceleration. A number of molecular dynamics packages, such as LAMMPS[158], Gromacs[159], and NAMD[160], employ heterogeneous CPU/GPU implementations, while others such as HOOMD-Blue[161], and OpenMM[162, 163, 164] provide pure GPU implementations.

Here, we introduce DASH, a high-performance, python-driven, GPU-implemented molecular dynamics engine. DASH implements the feature set necessary for both atomistic and coarse grained molecular dynamics, as well as several novel features, which are described in this work. Among the features highlighted here are: an efficient coupling scheme between CPU-based free energy sampling software and GPU-based molecular dynamics, a highly optimized implementation of path-integral molecular dynamics, and a flexible runtime analysis technique which utilizes both CPU and GPU parallelism.

7.2 Description of Software

7.2.1 Basic Features

In addition to several novel features which are highlighted in subsequent sections, DASH includes all of the standard components and functionality required to perform molecular dynamics simulations for a variety of systems. A brief description of the features is given below; a more complete description is provided in the the user documentation.

- **Pair potentials:** Lennard-Jones, Lennard-Jones with force shift, Lennand-Jones (CHARMM variant), Weeks-Chandler-Andersen (WCA), soft sphere, damped shifted force (DSF) charge interactions, and particle-particle particle-mesh (PPPM) charge interactions. New pair potentials can be easily added. Complicated aspects such as traversing neighborlists are abstracted from the programmer and user through effective use of C++ templates.

- **Bonded potentials:** Harmonic bonds, quartic bonds, FENE bonds, harmonic angles, CHARMM angles, cosine-delta angles, OPLS dihedrals, CHARMM dihedrals, harmonic impropers, CVFF impropers. As with pair potentials, adding additional potentials requires little effort on the part of the programmer.

- **Miscellaneous potentials:** Walls (harmonic and Lennard-Jones potentials), linear momentum control, TIP3P, TIP4P, q-TIP4P/Fw, and E3B3[165] water potentials, per-particle spring restraints, as well as harmonic and quartic external potentials.

- **Thermostats, barostats:** Nosé-Hoover thermostat, Langevin thermostat, Andersen thermostat, velocity rescaling thermostat, Nosé-Hoover barostat, Berendsen barostat, Monte Carlo barostat.

- **Integrators:** Velocity Verlet, FIRE relaxation[80], gradient descent relaxation.

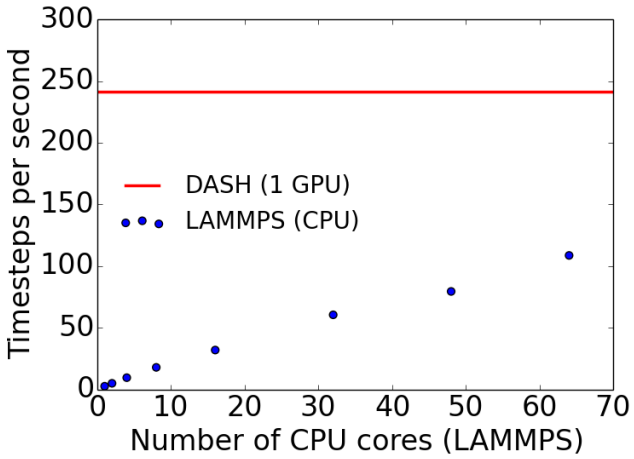

Figure 7.1: Timesteps per second for HPMC oligomer solvated in q-TIP4P/Fw water. DASH employs a single GPU in this benchmark, while LAMMPS employs up to 64 threads. DASH is run on a GeForce 1080Ti, while LAMMPS is run on tightly coupled 16 thread Sandy Bridge E5-2670 processors.

DASH also shows very strong performance. We benchmark DASH versus LAMMPS using a complex molecular system: an oligomer of hydroxymethylpropyl cellulose (HPMC) solvated in q-TIP4P/Fw water. The system consists of 20,565 atoms. This benchmark includes pair interactions, bonded potentials, short and long range electrostatics (using PPPM method), and rigid body dynamics. The performance in shown in Figure 7.1. Here, DASH uses a GeForce 1080Ti, while LAMMPS uses 16 thread Intel Xeon E5-2670 Sandy Bridge processors. Extrapolating the performance of LAMMPS, one would have to employ 146 Sandy Bridge cores in order to match the performance of DASH on a single GPU, assuming linear strong scaling for LAMMPS.

7.2.2 Efficient free energy sampling

Molecular dynamics typically achieves a 10X speedup when run on a GPU vs. a CPU-only machine. This is due to the trivial parallelizability of molecular dynamics - namely parallelizing systems on a per-particle basis as well as spatially across multiple GPUs. Free energy sampling, on the other hand, is not so easily parallelized. Free energy sampling methods

inherently rely on collective variables[166, 167, 168, 169]. These collective variables may involve particles spanning the entire system, making spatial parallelization challenging, or they may involve complex calculations which do not commute, making per-particle parallelization difficult. As a result, existing free energy sampling packages perform computations on the CPU[166, 167, 168, 169]. This presents challenges for GPU-based molecular dynamics engines, as transferring data between CPU and GPU memory is a costly process. We circumvent this issue by making the following assumption: In many free energy sampling problems, only a small fraction of particles in the system are involved in the relevant collection variables. For example, in protein simulations, solvent molecules typically comprise the vast majority of atoms, while typically only proteins are involved in biasing[170].

We design a coupling to the free energy sampling package SSAGES [168] which takes advantage of this assumption, resulting in significantly improved performance. Typical CPU-GPU coupling involves copying all particle information between the CPU and GPU at each timestep. The implementation of the DASH/SSAGES coupling involves significantly less copying between the CPU and GPU. At simulation initialization, the element of SSAGES which wraps DASH, referred to as the 'hook', establishes which particles are involved in collective variables for the free energy sampling. At each simulation timestep, the particles involved in the free energy biasing and copied to a dense array on the GPU, which is then transferred to the CPU. Forces for free energy biasing are calculated in serial on the CPU, the array is returned to the GPU, and forces are written into the active list of particles on the GPU.

Using this scheme, free energy sampling can be performed while incurring a minimal overhead. We perform benchmarks using a test system of the common conjugated polymer PTB7 solvated in chlorobenzene. The entire system consists of roughly 50,000 atoms. Umbrella sampling[171, 172] is performed on the center of mass distance between two PTB7 oligomers, which make up roughly 400 atoms in the system. Running umbrella sampling

incurs a 4% overhead versus simulations without umbrella sampling. For comparison, free energy sampling is performed using GPU acceleration in GROMMACS for a similar system, and an overhead of 103% is incurred. The sparse copying scheme implemented in the DASH/SSAGES coupling enables significant performances enhancement over traditional methods.

7.2.3 Efficient path-integral molecular dynamics

Nuclear quantum effects (NQEs)–such as zero-point energy and tunneling–are important in numerous physical and chemical processes, including enzyme catalysis, phase behavior, solvation structure, and isotope effects[173, 174, 175, 176, 177, 178, 179, 180, 181, 182, 183]. Traditionally, classical MD simulations neglect NQEs, which can result in quantitatively or even qualitatively incorrect behavior, particularly for studies that feature light nuclei or low temperatures.

Path-integral molecular dynamics (PIMD) provides an appealing framework to include NQEs in a classical simulation, by exploitation of the "classical isomorphism"[184] enabled by the Feynman path-integral formulation of quantum statistical mechanics [185]. Based on the equivalence of an exact quantum mechanical partition function with a classical configuration integral in an extended ring-polymer phase space[184], PIMD can be used to compute equilibrium properties for a quantum mechanical system by configurational sampling of an extended ring-polymer Hamiltonian. The formalism underlying PIMD is also the starting point for centroid molecular dynamics (CMD) [186, 187] and ring-polymer molecular dynamics[188, 189], which are techniques for approximating quantum time correlation functions. Although simulation studies employing PIMD are becoming more common[190], in part due to recent methodological[191, 192, 193, 194, 195, 196] and software developments[164, 197], widespread and effective use of PIMD (and related techniques) remains limited by (1) its increased computational expense relative to standard MD simulations and (2) its availability in versatile MD packages/codes. Implementation in DASH aims to address both issues by providing an

efficient, easy-to-use GPU-based platform for performing PIMD simulations.

In practice, PIMD requires simultaneous simulation of P replicas of the physical system with interactions prescribed by an effective ring-polymer Hamiltonian:

$$H_P = \sum_{j=1}^{N}\sum_{k=1}^{P}\left[\frac{|\mathbf{p}_j^{(k)}|^2}{2m_j} + \frac{1}{2}m_j\omega_P^2\big(\mathbf{r}_j^{(k)} - \mathbf{r}_j^{(k-1)}\big)^2\right] + \sum_{k=1}^{P} U(\mathbf{r}_1^{(k)}, ..., \mathbf{r}_N^{(k)}), \tag{7.1}$$

where $\mathbf{r}_j^{(k)}$ is the position of the jth atom in the kth replica, $\mathbf{p}_j^{(k)}$ is likewise for the momenta, m_j is the mass of the jth atom (treated equivalently across replicas), $U(\mathbf{r}_1^{(k)}, ..., \mathbf{r}_N^{(k)})$ is the potential energy of the kth replica, $\omega_P = P/\beta\hbar$, and cyclic boundary conditions are applied as $k = 0 = P$. In eq. 7.1, the interactions ordinarily computed in an MD simulation are augmented by harmonic forces between same-indexed atoms in adjacent replicas. Consequently, PIMD simulations are typically at least P times more expensive (with additional overhead due to communication between replicas) than a standard MD simulation. This amounts to greater than an order-of-magnitude increase in computational cost since good convergence of thermodynamic properties is practically obtained when $P \gtrsim \beta\hbar\omega_{\max}$ with $\omega_{\max}$ representing the fastest vibrational frequency in the system[193], such that simulations with $P = 16$ or $P = 32$ are common.

DASH provides basic, efficient support for conducting PIMD simulations. Both NVT and NPT conditions can be simulated using the Andersen thermostat and a Monte Carlo barostat; the number of replicas (beads in the ring-polymer) is allowed to be any power of 2 (within memory requirements); and by using the physical mass, RPMD simulations for approximate quantum dynamics are permitted. PIMD in DASH is further distinguished by several key features:

- PIMD is enabled in DASH *by default*, such that running a classical MD simulation is achieved by executing a PIMD simulation with $P = 1$ (although the user need not be aware of this). This design choice ensures that all algorithms and data structures within DASH are compatibly designed to work with $P \geq 1$ from the beginning. Importantly,

thread communication can be limited by using shared memory sensibly for kernels that depend on P in a non-trivial way, and data can be arranged to take advantage of both temporal and spatial locality. This is in contrast to naïve implementations that treat replicas independently but then require intermediate information-transfer among replicas, which limit code performance.

- Executing PIMD simulations is remarkably simple. Because PIMD is included by default, no additional packages, plug-ins, or installations are required, and a PIMD simulation can be run from an existing classical configuration with the addition of just two lines to the user's python script.

- The equations of motions are integrated using an efficient normal-mode scheme[192]. The harmonic forces between replicas, while computationally cheap, introduce high frequencies into the system that may require reduced timesteps and cause inefficient energy exchange, since the ring-polymer frequencies are well separated from the physical frequencies of the system. The normal-mode integration scheme[192] essentially takes advantage of the fact that the "free" ring-polymer Hamiltonian, which includes the spring forces between replicas, can be integrated analytically in the normal-mode representation, such that appropriate splitting of the time-evolution propagator permits timesteps that are typical for classical MD simulations.

- Non-bonded interactions are efficiently handled by performing all neighbor-listing operations with the centroids of the ring polymers and by computing long-range electrostatics via Ewald summation with ring-polymer (RP) contraction at the centroid level[193, 194]. Using RP contraction avoids the need for separate Ewald summations for each replica and reduces computational cost without sacrificing accuracy. For real-space cutoffs of 10-12 Å, the root-mean-square error associated with using RP contraction for this portion of the energy calculation is expected to be less than 0.03% [194].

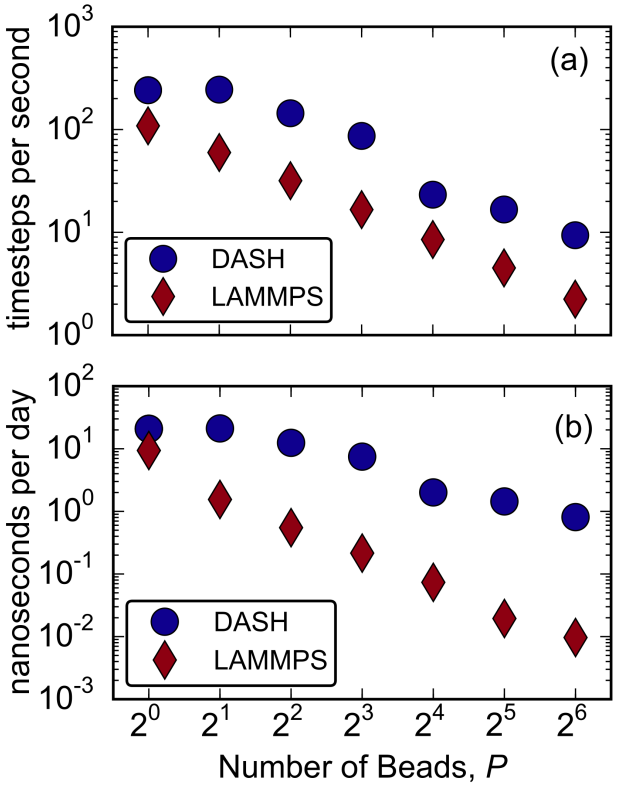

Figure 7.2: Benchmark comparison for path-integral molecular dynamics of a solvated polysaccharide oligomer using DASH and LAMMPS in terms of (a) timesteps elapsed per second and (b) nanoseconds simulated per day. The difference in relative performance reflected by the two metrics is due to a change in timestep size for stability in the LAMMPS simulations.

Support for more recent, advanced thermostats/barostats[192, 195] as well as mixed-quantum resolution systems via mixed time-slicing[191] is planned for future releases.

As a first benchmark for PIMD, we compare our implementation in DASH to an implementation in LAMMPS, which is among the most widely used MD codes available. Specifically, we simulate an oligomer of HPMC in aqueous solution using the CHARMM force field[198] for HPMC and q-TIP4P/Fw water–a flexible 4-site model parameterized for PIMD simulations[199]; a classical simulation ($P = 1$) consists of 20,565 atoms, 13,782 bonds, 7,179 angles, and 751 dihedrals, such that a simulation with $P = 64$ includes 1,316,160 particles and an additional 434,304 massless charge sites on the waters. DASH simulations were exe-

cuted using a single GeForce 1080Ti GPU card. LAMMPS simulations were executed using *fix pimd* (included in the USER-MISC package) with four tightly coupled Intel Xeon E5-2670 16-thread Sandy Bridge-EP, with $64/P$ processors allocated to each replica. The results are shown in Figure 7.2, with Figure 7.2a first indicating the metric of timesteps elapsed per second. Here, DASH begins about 2.2 times faster than LAMMPS for the conventional MD simulation, but that advantage widens to about a factor of 5, with some fluctuations, for PIMD. This performance gain is good considering the the disparity in resources (one GPU card versus 64 processors). Additionally, PIMD simulations in LAMMPS also required reduced timesteps to prevent atoms from being lost during simulation. Thus, we utilized the largest allowable timestep in increments of 0.05 fs that allowed the simulations to run error-free during benchmarking for LAMMPS; all DASH simulations were stably performed using a 1.0 fs timestep. This additional consideration is reflected in Figure 7.2b, which shows the metric of nanoseconds per day. In this case, DASH outperforms LAMMPS by at least an order of magnitude for all $P > 1$. Despite indications of a normal-mode integration scheme, LAMMPS performance was not improved when using the *nmpimd* option in this case.

As a second benchmark, we consider the performance of PIMD simulations of 1000, 2000, and 10,000 q-TIP4P/F water molecules. Using DASH on a single GeForce 1080Ti with a timestep of 0.5 fs and $P = 32$, we obtain 6.4, 3.3, and 0.67 nanoseconds per day. These numbers compare favorably to benchmarks of 1.7 and 1.2 nanoseconds per day for 1000 and 2000 molecules [200], respectively, reported using OpenMM, which provides GPU support for PIMD via its RPMD plugin, on a Nvidia GTX680. Because the GTX680 is a lower performance GPU card compared to the 1080Ti, this comparison simply illustrates that the PIMD implementation in DASH is competitive with other high-performance GPU-based codes with PIMD support.

7.2.4 Callback functionality

Flexible runtime data processing methods are essential to effective molecular simulation. Through its Python-driven interface, DASH allows for the user to inject python callbacks into the C++ runtime. These callbacks are called at user-specified intervals. DASH supports two distinct callback modes. The first, synchronous callbacks, are ideal for when data in the simulation (such as particle positions) must be modified by the callback in runtime. A schematic of this method is shown in Figure 7.3a. In this model, upon a callback being issued, computation on the GPU stops, and data is transferred to the CPU. Once complete, the user-defined python callback is called, and data is processed and transformed. Finally, data is transferred back to the GPU and the simulation resumes. This method leads to the GPU idling for a significant amount of time, which slows the simulation. However, any changes made to the simulation state are carried over to the GPU.

In more performance-critical situations or where data must only be processed, rather than modified, asynchronous callbacks are the superior choice. This method uses CPU-parallelism and GPU streams to maximize performance. A schematic of this process is shown in Figure 7.3b. At the turn where a callback must be fired, the main CPU thread copies atom data to a GPU buffer and launches a child CPU thread. This child thread creates a GPU stream which runs in parallel to the main GPU stream. This second GPU stream transfers data from the GPU buffer to the CPU. Meanwhile, the simulation continues to run. Once data transfer to the CPU is complete, the child CPU thread calls the user callback and data analysis is performed. Once complete, the child CPU thread is destroyed. This process allows for almost arbitrarily complex runtime analysis to be performed while incurring minimal performance penalties.

To demonstrate the effectiveness of this technique, we assess performance on a Lennard-Jones fluid system using two callbacks in both synchronous and asynchronous mode. The

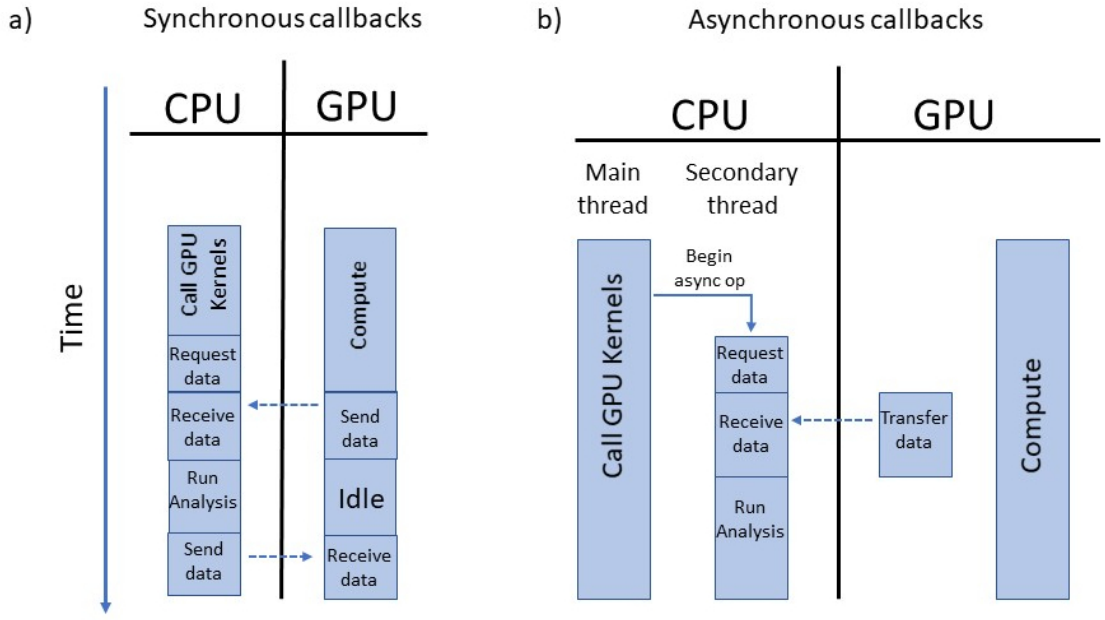

Figure 7.3: Schematic of runtime operations for a) synchronous and b) asynchronous callbacks. Synchronous callbacks can modify particle quantities during runtime, while asynchronous callbacks allow for more complex runtime computations without compromising simulation speed.

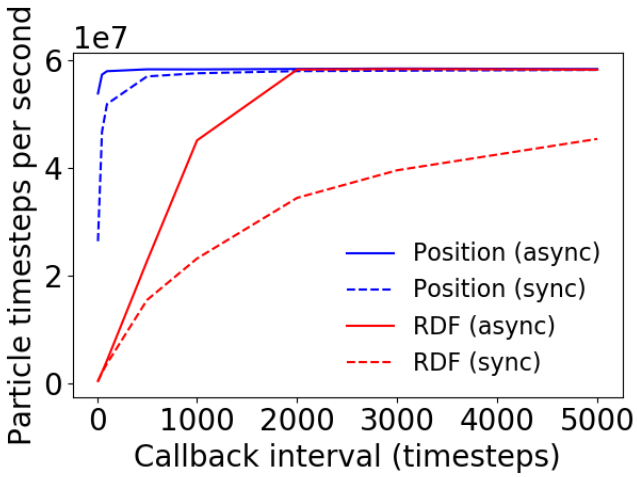

Figure 7.4: Particle timesteps per second versus callback frequency for simple and complex callback operations in synchronous and asynchronous mode. The simple call back (Position) records the position of a single particle, while the complex callback (RDF) computes the radial distribution function for several particles. Asynchronous callbacks allow for significantly accelerated simulations while computing complex quantities.

first callback simply records the position of a single particle, while the second computes a radial distribution function for several particles - a much more computationally demanding task. These two functions stand in for generic simple or complex functions which a user may define on runtime. The results are shown in Figure 7.4. As can be seen, asynchronous callbacks allow for significantly improved performance even in computationally intensive applications. This is because the GPU idle time is eliminated in the asynchronous callback structure. With sufficiently short intervals, performance decreases even for asynchronous callbacks. This is because in the current implementation, only one asynchronous thread may be running at once. The simulation must wait until one callback has finished before beginning a second.

7.3 Conclusion

To conclude, DASH offers a flexible, high-performance framework for performing molecular dynamics on both atomistic and coarse-grained systems. Being purely implemented on the

GPU, DASH makes good use of the otherwise-idle CPU to perform free energy sampling or runtime callbacks. In addition, DASH offers an efficient implementation of path integral molecular dynamics, which takes advantage of the spatial locality of particles in a given ring polymer. These features, together with the overall high performance of the engine, make DASH an effective and easy-to-use molecular dynamics engine.

CHAPTER 8

CONCLUSION

In this work, we have introduced a variety of techniques which make possible or enhance the design and study of amorphous materials. Casting disordered materials as mechanical metamaterials, we show that through a variety of pruning and optimization schemes, materials can be developed which show Poisson's ratios near the lower mechanical limit. These techniques create an extensible framework for designing tailor-made metamaterials. In the future, such concepts will likely be applied to creating three-dimensional analogues in experiment. Other avenues could also be explored, such as creating materials which show tuned acoustic or thermal properties. While the fabrication of such devices in three dimensions will no doubt be challenging, 3D printing technology is rapidly advancing, and with any luck will enabled these advances in simulation to be translated into reality.

Physical vapor deposition provides another appealing method of tuning disordered materials, in this case glasses. The findings in this work provide valuable insight into the underlying nature of these materials. Employing the findings in this work, a variety of useful extrapolations become valid. Trends based on liquid-cooled glass data such as those describing density, moduli, or transition temperatures, can now be applied to vapor deposited glasses based on extrapolations from the liquid-cooled analogues.

Organic photovoltaics, a perennially challenging area for practitioners of both simulation and experiment, are perhaps the most complicated system studied here. The alphabet soup of semiconducting organic materials combined with their rich phase behavior yields innumerable parameters which an experimentalist must explore. Here, our simulations provide valuable tools to make this task more tractable. By pre-screening and designing materials for solubility, an entire dimension in an experimentalist's search space is removed. Furthermore, by employing the REDOR NMR-based biasing technique developed in this work, new insight can be gained into the fine-grain detail of the complex yet important interfaces between electron donors and acceptors in organic photovoltaics.

Ultimately, all of this work is powered by software. In our molecular simulation engine, DASH, we seek to enhance the state of simulation software by providing a high-performance, easy-to-use, and flexible software package. Combined with its unique features such as an efficient path integral molecular dynamics scheme and efficient coupling to free energy sampling software, DASH is a useful addition to the simulation community's library of software.

REFERENCES

[1] C. P. Goodrich, A. J. Liu, and S. R. Nagel, "The principle of independent bond-level response: Tuning by pruning to exploit disorder for global behavior," *Physical review letters*, vol. 114, no. 22, p. 225501, 2015.

[2] K. Evans, "The design of doubly curved sandwich panels with honeycomb cores," *Composite Structures*, vol. 17, no. 2, pp. 95–111, 1991.

[3] W. Miller, C. Smith, and K. Evans, "Honeycomb cores with enhanced buckling strength," *Composite Structures*, vol. 93, no. 3, pp. 1072–1077, 2011.

[4] K. Evans, J. Donoghue, and K. Alderson, "The design, matching and manufacture of auxetic carbon fibre laminates," *Journal of composite materials*, vol. 38, no. 2, pp. 95–106, 2004.

[5] K. Alderson, A. Pickles, P. Neale, and K. Evans, "Auxetic polyethylene: the effect of a negative poisson's ratio on hardness," *Acta Metallurgica et Materialia*, vol. 42, no. 7, pp. 2261–2266, 1994.

[6] M. Sanami, N. Ravirala, K. Alderson, and A. Alderson, "Auxetic materials for sports applications," *Procedia Engineering*, vol. 72, pp. 453–458, 2014.

[7] A. Alderson, J. Rasburn, S. Ameer-Beg, P. G. Mullarkey, W. Perrie, and K. E. Evans, "An auxetic filter: a tuneable filter displaying enhanced size selectivity or defouling properties," *Industrial & engineering chemistry research*, vol. 39, no. 3, pp. 654–665, 2000.

[8] A. Alderson, J. Rasburn, K. Evans, and J. Grima, "Auxetic polymeric filters display enhanced de-fouling and pressure compensation properties," *Membrane Technology*, vol. 2001, no. 137, pp. 6–8, 2001.

[9] K. Alderson, A. Alderson, S. Anand, V. Simkins, S. Nazare, and N. Ravirala, "Auxetic warp knit textile structures," *physica status solidi (b)*, vol. 249, no. 7, pp. 1322–1329, 2012.

[10] H. Hu, Z. Wang, and S. Liu, "Development of auxetic fabrics using flat knitting technology," *Textile Research Journal*, p. 0040517511404594, 2011.

[11] S. R. Nagel, "Experimental soft-matter science," *Rev. Mod. Phys.*, vol. 89, p. 025002, Apr 2017.

[12] R. Lakes, "Foam structures with a negative poisson's ratio," *Science*, vol. 235, no. 4792, pp. 1038–1040, 1987.

[13] B. Caddock and K. Evans, "Microporous materials with negative poisson's ratios. i. microstructure and mechanical properties," *Journal of Physics D: Applied Physics*, vol. 22, no. 12, p. 1877, 1989.

[14] N. Chan and K. Evans, "Fabrication methods for auxetic foams," *Journal of Materials Science*, vol. 32, no. 22, pp. 5945–5953, 1997.

[15] N. Ravirala, K. L. Alderson, P. J. Davies, V. R. Simkins, and A. Alderson, "Negative poissons ratio polyester fibers," *Textile research journal*, vol. 76, no. 7, pp. 540–546, 2006.

[16] A. Pickles, R. Webber, K. Alderson, P. Neale, and K. Evans, "The effect of the processing parameters on the fabrication of auxetic polyethylene," *Journal of materials science*, vol. 30, no. 16, pp. 4059–4068, 1995.

[17] N. Chan and K. Evans, "Microscopic examination of the microstructure and deformation of conventional and auxetic foams," *Journal of Materials Science*, vol. 32, no. 21, pp. 5725–5736, 1997.

[18] S. Timoshenko and J. Goodier, "Theory of elasticity 3rd ed., 1970."

[19] U. D. Larsen, O. Signund, and S. Bouwsta, "Design and fabrication of compliant micromechanisms and structures with negative poisson's ratio," *Journal of Microelectromechanical Systems*, vol. 6, no. 2, pp. 99–106, 1997.

[20] P. Theocaris, G. Stavroulakis, and P. Panagiotopoulos, "Negative poisson's ratios in composites with star-shaped inclusions: a numerical homogenization approach," *Archive of Applied Mechanics*, vol. 67, no. 4, pp. 274–286, 1997.

[21] L. Gibson, M. Ashby, G. Schajer, and C. Robertson, "The mechanics of two-dimensional cellular materials," *Proceedings of the Royal Society of London A: Mathematical, Physical and Engineering Sciences*, vol. 382, no. 1782, pp. 25–42, 1982.

[22] T. L. Warren, "Negative poissons ratio in a transversely isotropic foam structure," *Journal of applied physics*, vol. 67, no. 12, pp. 7591–7594, 1990.

[23] B. Florijn, C. Coulais, and M. van Hecke, "Programmable mechanical metamaterials," *Physical review letters*, vol. 113, no. 17, p. 175503, 2014.

[24] D. Hexner, A. J. Liu, and S. R. Nagel, "Role of local response in manipulating the elastic properties of disordered solids by bond removal," *arXiv preprint arXiv:1708.07207*, 2017.

[25] D. Hexner, A. J. Liu, and S. R. Nagel, "Linking microscopic and macroscopic response in disordered solids," *arXiv preprint arXiv:1706.06153*, 2017.

[26] J. W. Rocks, N. Pashine, I. Bischofberger, C. P. Goodrich, A. J. Liu, and S. R. Nagel, "Designing allostery-inspired response in mechanical networks," *Proceedings of the National Academy of Sciences*, vol. 114, no. 10, pp. 2520–2525, 2017.

[27] A. J. Liu and S. R. Nagel, "The jamming transition and the marginally jammed solid," *Annu. Rev. Condens. Matter Phys.*, vol. 1, no. 1, pp. 347–369, 2010.

[28] D. M. Sussman, C. P. Goodrich, and A. J. Liu, "Spatial structure of states of self stress in jammed systems," *Soft matter*, vol. 12, no. 17, pp. 3982–3990, 2016.

[29] M. M. Driscoll, B. G.-g. Chen, T. H. Beuman, S. Ulrich, S. R. Nagel, and V. Vitelli, "The role of rigidity in controlling material failure," *Proceedings of the National Academy of Sciences*, vol. 113, no. 39, pp. 10813–10817, 2016.

[30] J. M. Wozniak, T. G. Armstrong, M. Wilde, D. S. Katz, E. Lusk, and I. T. Foster, "Swift/t: Large-scale application composition via distributed-memory dataflow processing," in *Cluster, Cloud and Grid Computing (CCGrid), 2013 13th IEEE/ACM International Symposium on*, pp. 95–102, IEEE, 2013.

[31] A. Zaccone and E. M. Terentjev, "Short-range correlations control the g/k and poisson ratios of amorphous solids and metallic glasses," *Journal of Applied Physics*, vol. 115, no. 3, p. 033510, 2014.

[32] Q. Liu, "Literature review: materials with negative poisson's ratios and potential applications to aerospace and defense," tech. rep., Defense Science and Technology Organization Victoria (Australia) Air Vehicles Division, 2006.

[33] A. Alderson and K. Alderson, "Auxetic materials," *Proceedings of the Institution of Mechanical Engineers, Part G: Journal of Aerospace Engineering*, vol. 221, no. 4, pp. 565–575, 2007.

[34] J. Schwerdtfeger, F. Wein, G. Leugering, R. Singer, C. Körner, M. Stingl, and F. Schury, "Design of auxetic structures via mathematical optimization," *Advanced materials*, vol. 23, no. 22-23, pp. 2650–2654, 2011.

[35] S. Shan, S. H. Kang, Z. Zhao, L. Fang, and K. Bertoldi, "Design of planar isotropic negative poissons ratio structures," *Extreme Mechanics Letters*, vol. 4, pp. 96–102, 2015.

[36] D. Prall and R. Lakes, "Properties of a chiral honeycomb with a poisson's ratio of1," *International Journal of Mechanical Sciences*, vol. 39, no. 3, pp. 305–314, 1997.

[37] E. Friis, R. Lakes, and J. Park, "Negative poisson's ratio polymeric and metallic foams," *Journal of Materials Science*, vol. 23, no. 12, pp. 4406–4414, 1988.

[38] C. W. Smith, J. Grima, and K. Evans, "A novel mechanism for generating auxetic behaviour in reticulated foams: missing rib foam model," *Acta materialia*, vol. 48, no. 17, pp. 4349–4356, 2000.

[39] F. Robert, "An isotropic three-dimensional structure with poisson's ratio-1," *Journal of Elasticity*, vol. 15, pp. 427–430, 1985.

[40] D. R. Reid, N. Pashine, J. M. Wozniak, H. M. Jaeger, A. J. Liu, S. R. Nagel, and J. J. de Pablo, "Auxetic metamaterials from disordered networks," *arXiv preprint arXiv:1710.02493*, 2017.

[41] K. Yoshimoto, T. S. Jain, K. Van Workum, P. F. Nealey, and J. J. de Pablo, "Mechanical heterogeneities in model polymer glasses at small length scales," *Physical review letters*, vol. 93, no. 17, p. 175501, 2004.

[42] C. A. Mirkin, R. L. Letsinger, R. C. Mucic, and J. J. Storhoff, "A dna-based method for rationally assembling nanoparticles into macroscopic materials," *Nature*, vol. 382, no. 6592, pp. 607–609, 1996.

[43] J. Lequieu, A. Cordoba, D. Hinckley, and J. J. de Pablo, "Mechanical response of dna–nanoparticle crystals to controlled deformation," *ACS central science*, vol. 2, no. 9, pp. 614–620, 2016.

[44] L. W. Antony, N. E. Jackson, I. Lyubimov, V. Vishwanath, M. D. Ediger, and J. J. de Pablo, "Influence of vapor deposition on structural and charge transport properties of ethylbenzene films," *ACS central science*, vol. 3, no. 5, pp. 415–424, 2017.

[45] D. R. Reid, I. Lyubimov, M. Ediger, and J. J. De Pablo, "Age and structure of a model vapour-deposited glass," *Nature communications*, vol. 7, 2016.

[46] S. Singh, M. Ediger, and J. J. De Pablo, "Ultrastable glasses from in silico vapour deposition," *Nature materials*, vol. 12, no. 2, pp. 139–144, 2013.

[47] K. Sun, T.-S. Wei, B. Y. Ahn, J. Y. Seo, S. J. Dillon, and J. A. Lewis, "3d printing of interdigitated li-ion microbattery architectures," *Advanced Materials*, vol. 25, no. 33, pp. 4539–4543, 2013.

[48] C. A. Angell, "Formation of glasses from liquids and biopolymers," *Science*, vol. 267, no. 5206, pp. 1924–1935, 1995.

[49] R. L. Jack, L. O. Hedges, J. P. Garrahan, and D. Chandler, "Preparation and relaxation of very stable glassy states of a simulated liquid," *Physical review letters*, vol. 107, no. 27, p. 275702, 2011.

[50] S. F. Swallen, K. L. Kearns, M. K. Mapes, Y. S. Kim, R. J. McMahon, M. D. Ediger, T. Wu, L. Yu, and S. Satija, "Organic glasses with exceptional thermodynamic and kinetic stability," *Science*, vol. 315, no. 5810, pp. 353–356, 2007.

[51] K. L. Kearns, T. Still, G. Fytas, and M. Ediger, "High-modulus organic glasses prepared by physical vapor deposition," *Advanced Materials*, vol. 22, no. 1, pp. 39–42, 2010.

[52] S. L. L. Ramos, M. Oguni, K. Ishii, and H. Nakayama, "Character of devitrification, viewed from enthalpic paths, of the vapor-deposited ethylbenzene glasses," *The Journal of Physical Chemistry B*, vol. 115, no. 49, pp. 14327–14332, 2011.

[53] L. Zhu and L. Yu, "Generality of forming stable organic glasses by vapor deposition," *Chemical Physics Letters*, vol. 499, no. 1, pp. 62–65, 2010.

[54] L. Yu, "Amorphous pharmaceutical solids: preparation, characterization and stabilization," *Advanced drug delivery reviews*, vol. 48, no. 1, pp. 27–42, 2001.

[55] K. L. Kearns, S. F. Swallen, M. Ediger, T. Wu, and L. Yu, "Influence of substrate temperature on the stability of glasses prepared by vapor deposition," *The Journal of chemical physics*, vol. 127, no. 15, p. 154702, 2007.

[56] Z. Yang, Y. Fujii, F. K. Lee, C.-H. Lam, and O. K. Tsui, "Glass transition dynamics and surface layer mobility in unentangled polystyrene films," *Science*, vol. 328, no. 5986, pp. 1676–1679, 2010.

[57] L. Zhu, C. Brian, S. Swallen, P. Straus, M. Ediger, and L. Yu, "Surface self-diffusion of an organic glass," *Physical Review Letters*, vol. 106, no. 25, p. 256103, 2011.

[58] S. Singh and J. J. de Pablo, "A molecular view of vapor deposited glasses," *The Journal of chemical physics*, vol. 134, no. 19, p. 194903, 2011.

[59] S. S. Dalal, D. M. Walters, I. Lyubimov, J. J. de Pablo, and M. Ediger, "Tunable molecular orientation and elevated thermal stability of vapor-deposited organic semiconductors," *Proceedings of the National Academy of Sciences*, vol. 112, no. 14, pp. 4227–4232, 2015.

[60] G. M. Hocky, L. Berthier, and D. R. Reichman, "Equilibrium ultrastable glasses produced by random pinning," *The Journal of chemical physics*, vol. 141, no. 22, p. 224503, 2014.

[61] P. Pieranski, "Two-dimensional interfacial colloidal crystals," *Physical Review Letters*, vol. 45, no. 7, p. 569, 1980.

[62] N. Denkov, O. Velev, P. Kralchevski, I. Ivanov, H. Yoshimura, and K. Nagayama, "Mechanism of formation of two-dimensional crystals from latex particles on substrates," *Langmuir*, vol. 8, no. 12, pp. 3183–3190, 1992.

[63] E. R. Weeks, J. C. Crocker, A. C. Levitt, A. Schofield, and D. A. Weitz, "Three-dimensional direct imaging of structural relaxation near the colloidal glass transition," *Science*, vol. 287, no. 5453, pp. 627–631, 2000.

[64] F. Ebert, P. Keim, and G. Maret, "Local crystalline order in a 2d colloidal glass former," *The European Physical Journal E*, vol. 26, no. 1-2, pp. 161–168, 2008.

[65] P. Y. Huang, S. Kurasch, A. Srivastava, V. Skakalova, J. Kotakoski, A. V. Krasheninnikov, R. Hovden, Q. Mao, J. C. Meyer, J. Smet, *et al.*, "Direct imaging of a two-dimensional silica glass on graphene," *Nano letters*, vol. 12, no. 2, pp. 1081–1086, 2012.

[66] Z. Zheng, F. Wang, Y. Han, *et al.*, "Glass transitions in quasi-two-dimensional suspensions of colloidal ellipsoids," *Physical review letters*, vol. 107, no. 6, p. 065702, 2011.

[67] P. J. Steinhardt, D. R. Nelson, and M. Ronchetti, "Bond-orientational order in liquids and glasses," *Physical Review B*, vol. 28, no. 2, p. 784, 1983.

[68] Z. Shi, P. G. Debenedetti, and F. H. Stillinger, "Properties of model atomic free-standing thin films," *The Journal of chemical physics*, vol. 134, no. 11, p. 114524, 2011.

[69] P. G. Debenedetti and F. H. Stillinger, "Supercooled liquids and the glass transition," *Nature*, vol. 410, no. 6825, p. 259, 2001.

[70] K. L. Kearns, S. F. Swallen, M. D. Ediger, T. Wu, Y. Sun, and L. Yu, "Hiking down the energy landscape: Progress toward the kauzmann temperature via vapor deposition," *The Journal of Physical Chemistry B*, vol. 112, no. 16, pp. 4934–4942, 2008.

[71] H.-B. Yu, Y. Luo, and K. Samwer, "Ultrastable metallic glass," *Advanced Materials*, vol. 25, no. 41, pp. 5904–5908, 2013.

[72] I. Lyubimov, M. D. Ediger, and J. J. de Pablo, "Model vapor-deposited glasses: Growth front and composition effects," *The Journal of chemical physics*, vol. 139, no. 14, p. 144505, 2013.

[73] K. Dawson, L. Zhu, L. A. Kopff, R. J. McMahon, L. Yu, and M. D. Ediger, "Highly stable vapor-deposited glasses of four tris-naphthylbenzene isomers," *The Journal of Physical Chemistry Letters*, vol. 2, no. 21, pp. 2683–2687, 2011.

[74] C. Rodríguez-Tinoco, M. Gonzalez-Silveira, J. Rafols-Ribe, A. F. Lopeandía, M. T. Clavaguera-Mora, and J. Rodríguez-Viejo, "Evaluation of growth front velocity in ultrastable glasses of indomethacin over a wide temperature interval," *The Journal of Physical Chemistry B*, vol. 118, no. 36, pp. 10795–10801, 2014.

[75] H. Heinz, R. Vaia, B. Farmer, and R. Naik, "Accurate simulation of surfaces and interfaces of face-centered cubic metals using 12- 6 and 9- 6 lennard-jones potentials," *The Journal of Physical Chemistry C*, vol. 112, no. 44, pp. 17281–17290, 2008.

[76] C. W. Brian and L. Yu, "Surface self-diffusion of organic glasses," *The Journal of Physical Chemistry A*, vol. 117, no. 50, pp. 13303–13309, 2013.

[77] C. Donati, J. F. Douglas, W. Kob, S. J. Plimpton, P. H. Poole, and S. C. Glotzer, "Stringlike cooperative motion in a supercooled liquid," *Physical review letters*, vol. 80, no. 11, p. 2338, 1998.

[78] H. Shintani and H. Tanaka, "Frustration on the way to crystallization in glass," *Nature Physics*, vol. 2, no. 3, pp. 200–206, 2006.

[79] G. J. Martyna, M. L. Klein, and M. Tuckerman, "Nosé–hoover chains: the canonical ensemble via continuous dynamics," *The Journal of chemical physics*, vol. 97, no. 4, pp. 2635–2643, 1992.

[80] E. Bitzek, P. Koskinen, F. Gähler, M. Moseler, and P. Gumbsch, "Structural relaxation made simple," *Physical review letters*, vol. 97, no. 17, p. 170201, 2006.

[81] S. Plimpton, "Fast parallel algorithms for short-range molecular dynamics," *Journal of computational physics*, vol. 117, no. 1, pp. 1–19, 1995.

[82] J. D. Hunter, "Matplotlib: A 2d graphics environment," *Computing In Science & Engineering*, vol. 9, no. 3, pp. 90–95, 2007.

[83] L. Dou, J. You, Z. Hong, Z. Xu, G. Li, R. A. Street, and Y. Yang, "25th Anniversary Article: A Decade of Organic/Polymeric Photovoltaic Research," *Advanced Materials*, vol. 25, no. 46, pp. 6642–6671, 2013.

[84] A. J. Heeger, "25th anniversary article: Bulk heterojunction solar cells: understanding the mechanism of operation.," *Advanced materials (Deerfield Beach, Fla.)*, vol. 26, pp. 10–27, jan 2014.

[85] J. Rivnay, S. C. Mannsfeld, C. E. Miller, A. Salleo, and M. F. Toney, "Quantitative Determination of Organic Semiconductor Microstructure from the Molecular to Device Scale," *Chem. Rev.*, vol. 112, no. 10, pp. 5488–5519, 2012.

[86] N. E. Jackson, B. M. Savoie, T. J. Marks, L. X. Chen, and M. A. Ratner, "The Next Breakthrough for Organic Photovoltaics?," *Journal of Physical Chemistry Letters*, vol. 6, pp. 77–84, 2015.

[87] J. Zhao, A. Swinnen, G. V. Assche, J. Manca, D. Vanderzande, and B. V. Mele, "Phase Diagram of P3HT / PCBM Blends and Its Implication for the Stability of Morphology," *J Phys Chem B*, vol. 113, pp. 1587–1591, 2009.

[88] J. Liu, T.-f. Guo, and Y. Yang, "Effects of thermal annealing on the performance of polymer light emitting diodes," *Journal of Applied Physics*, vol. 91, no. 3, pp. 1595–1600, 2002.

[89] R. Kroon, R. Gehlhaar, T. T. Steckler, P. Henriksson, M. Christian, J. Bergqvist, A. Hadipour, P. Heremans, and M. R. Andersson, "Solar Energy Materials & Solar Cells New quinoxaline and pyridopyrazine-based polymers for solution-processable photovoltaics," *Solar Energy Materials and Solar Cells*, vol. 105, pp. 280–286, 2012.

[90] T.-y. Chu, J. Lu, S. Beaupré, Y. Zhang, J.-r. Pouliot, J. Zhou, A. Najari, M. Leclerc, and Y. Tao, "Effects of the Molecular Weight and the Side-Chain Length on the Photovoltaic Performance of Dithienosilole / Thienopyrrolodione Copolymers," *Advanced Functional Materials*, vol. 22, pp. 2345–2351, 2012.

[91] J. A. Bartelt, J. D. Douglas, W. R. Mateker, A. E. Labban, C. J. Tasone, M. F. Toney, J. M. Frechet, P. M. Beaujuge, and M. D. McGehee, "Controlling solution-phase polymer aggregation with molecular weight and solvent additives to optimize polymer-fullerene bulk heterojunction solar cells," *Advanced Energy Materials*, vol. 4, no. 9, pp. 1–11, 2014.

[92] R. Steyrleuthner, M. Schubert, I. Howard, B. Klaumu, K. Schilling, Z. Chen, and P. Saalfrank, "Aggregation in a High-Mobility n Type Low-Bandgap Copolymer with Implications on Semicrystalline Morphology," *J Am Chem Soc*, vol. 134, no. 44, pp. 18303–18317, 2012.

[93] Y.-Q. Zheng, Z.-F. Yao, T. Lei, J.-H. Dou, C.-Y. Yang, L. Zou, X. Meng, W. Ma, J.-Y. Wang, and J. Pei, "Understanding the Solution-State Supramoleular Structure of Donor-Acceptor Polymers and their Influence on Solid-State Morphology and Charge-Transport Properties," *Adv. Mater.*, vol. 29, p. 1701072, 2017.

[94] T.-Q. Nguyen, R. Yee, and B. Schwartz, "Solution Processing of Conjugated Polymers: The Effects of Polymer Solubility on the Morphology and Electronic Properties of Semiconducting Polymer Films," *J. Photochem. Photobio.*, vol. 144, pp. 21–30, 2001.

[95] T.-Q. Nguyen, V. DOan, and B. Schwartz, "Conjugated Polymer aggregates in solution: Control of Interchain Interactions," *J. Chem. Phys*, vol. 110, pp. 4068–4078, 1999.

[96] L.-H. Zhao, R.-Q. Ping, J.-M. Zhuo, L.-Y. Wong, J.-C. Tang, Y.-S. Su, and L.-L. Chua, "Role of Borderline Solvents to Induce Pronounced Extended-Chain Lamellar Order in pi-Stackable Polymers," *Macromolecules*, vol. 44, pp. 9692–9702, 2011.

[97] Y. Huang, H. Cheng, and C. C. Han, "Temperature Induced Structure Evolution of Regioregular Poly(3-hexylthiophene) in Dilute Solution and its Influence on Thin Film Morphology," *Macromolecules*, vol. 43, pp. 10031–10037, 2010.

[98] Y. Diao, L. Shaw, Z. Bao, and S. C. Mannsfeld *Energy Environ. Sci.*

[99] P. Cheng, C. Yan, Y. Li, W. Ma, and X. Zhan *Energy Environ. Sci.*

[100] T. Eder, T. Stangl, M. Gmelch, K. Remmerssen, D. Laux, S. Hoger, J. M. Lupton, and J. Vogelsang, "Switching between H- and J-type electronic coupling in single conjugated polymer aggregates," *Nat. Comm.*, vol. 8, p. 1641, 2018.

[101] S. Wang, S. Fabiano, S. Himmelberger, S. Puzinas, X. Crispin, A. Salleo, and M. Berggren, "Experimental Evidence That Short-Range Intermolecular Aggregation is Sufficient for Efficient Charge Transport in Conjugated Polymers," *Proc. Natl. Acad. Sci. U.S.A.*, vol. 112, pp. 10599–10604, 2015.

[102] Y. Liu, J. Zhao, Z. Li, C. Mu, W. Ma, H. Hu, K. Jiang, H. Lin, H. Ade, and H. Yan, "Multiple Cases of High-Efficiency Polymer Solar Cells," *Nature Communications*, vol. 5, no. 9, pp. 1–8, 2014.

[103] Y. D. Park, J. K. Park, J. H. Seo, J. D. Yuen, W. H. Lee, K. Cho, and G. C. Bazan, "Solubility-Controlled Structural Ordering of Narrow Bandgap Conjugated Polymers," *Adv. Energy Mater.*, vol. 1, no. 1, pp. 63–67, 2010.

[104] M. S. Chen, O. P. Lee, J. R. Niskala, A. T. Yiu, C. J. Tassone, K. Schmidt, P. M. Beaujuge, S. S. Onishi, M. F. Toney, A. Zettl, and J. M. Frechet, "Enhanced Solid-State Order and Field-E ff ect Hole Mobility through Control of Nanoscale Polymer Aggregation," *J Am Chem Soc*, vol. 135, no. 51, pp. 19229–19236, 2013.

[105] A. Luzio, L. Criante, and M. Caironi, "Control of charge transport in a semiconducting copolymer by solvent-induced long-range order," *Scientific Reports*, vol. 3, no. 3425, pp. 1–6, 2013.

[106] D. Wang, Y. Yuan, Y. Mardiyati, C. Bubeck, and K. Koynov, "From single chains to aggregates, how conjugated polymers behave in dilute solutions," *Macromolecules*, vol. 46, no. 15, pp. 6217–6224, 2013.

[107] T. J. Fauvell, T. Zheng, N. E. Jackson, M. A. Ratner, L. Yu, and L. X. Chen, "Photophysical and Morphological Implications of Single-Strand Conjugated Polymer Folding in Solution," *Chem. Mater.*, vol. 28, no. 8, pp. 2814–2822, 2016.

[108] Z. Hu, J. Liu, L. Simon-Bower, L. Zhai, and A. J. Gesquiere, "Influence of Backbone Rigidness on Single Chain Conformation of Thiophene-Based Conjugated Polymers," *J. Phys. Chem. B*, vol. 117, pp. 4461–4467, 2012.

[109] M. C. Traub, K. H. Dubay, S. E. Ingle, X. Zhu, K. N. Plunkett, D. R. Reichman, and D. A. V. Bout, "Chromophore-controlled self-assembly of highly ordered polymer nanostructures," *Journal of Physical Chemistry Letters*, vol. 4, no. 15, pp. 2520–2524, 2013.

[110] J. Mei and Z. Bao *Chem. Mater.*

[111] B. McCulloch, V. Ho, M. Hoarfrost, C. Stanely, C. Do, W. T. Heller, and R. A. Segalman *Macromolecules*.

[112] J. Aime, F. Bargain, M. Schott, H. Eckhardt, G. Miller, and R. Elsenbaumer *Phys. Rev. Lett.*

[113] B. Kuei and E. D. Gomez *Soft Matter*.

[114] N. E. Jackson, K. L. Kohlstedt, B. M. Savoie, M. O. de la Cruz, G. C. Schatz, L. X. Chen, and M. A. Ratner, "Conformational Order in Aggregates of Conjugated Polymers.," *Journal of the American Chemical Society*, vol. 137, no. 19, pp. 6254–6262, 2015.

[115] S. E. Root, N. E. Jackson, S. Savagatrup, G. Arya, and D. J. Lipomi, "Modelling the morphology and thermomechanical behaviour of low-bandgap conjugated polymers and bulk heterojunction films," *Energy Environ. Sci.*, vol. 10, pp. 558–569, 2017.

[116] C. K. Lee, C. C. Hua, and S. A. Chen, "Hybrid Solvents Incubated pi-pi Stacking in Quenched Conjugated Polymer Resolved by Multiscale Computation," *Macromolecules*, vol. 44, pp. 320–324, 2011.

[117] Z. Hu, T. Adachi, Y.-G. Lee, R. T. Haws, B. Hanson, R. J. Ono, C. Biewlawski, V. Ganesan, P. J. Rossky, and D. A. V. Bout, "Effect of the Side-Chain-Distribution Density on the Single-Conjugated-Polymer-Chain Conformation," *Chem. Phys. Chem.*, vol. 14, pp. 4143–4148, 2015.

[118] F. L. Lee, A. B. Farimani, K. L. Gu, H. Yan, M. F. Toney, Z. Bao, and V. S. Pande, "Solution-Phase Conformation and Dynamics of Conjugated Isoindigo-Based Donor-Acceptor Polymer Single Chains," *J. Phys. Chem. Lett*, vol. 8, pp. 5479–5486, 2017.

[119] H. L. Yi, C. H. Wu, C. I. Wang, and C. C. Hua, "Solvent-Regulated Mesoscale Aggregation Properties of Dilute PBTTT-C14 Solutions," *Macromolecules*, vol. 50, pp. 5498–5509, 2017.

[120] D. Hu, J. Yu, K. Wong, B. Bagchi, P. J. Rossky, and P. F. Barbara *Nature*.

[121] C. K. Lee, C. C. Hua, and S. A. Chen, "An ellipsoid-chain model for conjugated polymer solutions," *J. Chem. Phys*, vol. 136, p. 084901, 2012.

[122] S. C. Shie, C. K. Lee, C. C. Hua, and S. A. Chen, "A Predictive Coarse-Grained Model for Semiflexible Polymers in Specific Solvents," *Macromol. Thory Simul.*, vol. 19, pp. 179–189, 2012.

[123] M. Doi and S. F. Edwards, *The theory of polymer dynamics*, vol. 73. oxford university press, 1988.

[124] W. L. Jorgensen, D. S. Maxwell, and J. Tirado-Rives, "Development and Testing of the OLPS All-Atom Force Field on Conformational Energetics and Properties of Organic Liquids," *Journal of the American Chemical Society*, vol. 118, no. 15, pp. 11225–11236, 1996.

[125] "DASH: A GPU-Accelerated Molecular Dynamics Engine."

[126] *Certain commercial equipment, instruments, or materials are identified in this paper in order to specify the experimental procedure adequately. Such identification is not intended to imply recommendation or endorsement by the National Institute of Standards and Technology, nor is it intended to imply that the materials or equipment identified are necessarily the best available for the purpose.*

[127] S. Kline, "Reduction and analysis of SANS and USANS data using IGOR Pro," *Journal of Applied Crystallography*, vol. 39, no. 6, pp. 895–900, 2006.

[128] *This work benefited from the use of the SasView application, originally developed under NSF award DMR-0520547. SasView contains code developed with funding from the European Union's Horizon 2020 research and innovation programme under the SINE2020 project, grant agreement No 654000. http://www.sasview.org/.*

[129] H. Sidkey, Y. Colon, J. Helfferich, B. J. Sikora, C. Bezik, W. Chu, F. Giberti, A. Guo, X. Jiang, J. Lequieu, J. Li, J. Moller, M. Quevillon, M. Rahimi, H. Ramezani-Dakhel, V. Rathee, D. Reid, E. Sevgen, V. Thapar, M. Webb, J. Whitmer, and J. de Pablo,

"SSAGES: Software Suite for Advanced General Ensemble Simulations," *J. Chem. Phys.*, vol. 148, p. 044104, 2018.

[130] B. Roux, "The calculation of the potential of mean force using computer simulations," *Computer Physics Communications*, vol. 91, no. 1-3, pp. 275–282, 1995.

[131] M. Belmares, M. Blanco, W. G. III, R. Ross, G. Caldwell, S. Chou, J. Pham, P. Olofson, and C. Thomas, "Hildebrand and Hansen Solubility Parameters from Molecular Dynamics with Applications to Electronic Nose Polymer Sensors," *J. Comput. Chem.*, vol. 25, pp. 1814–1826, 2014.

[132] N. E. Jackson, L. X. Chen, and M. A. Ratner, "Solubility of Non-Electrolytes: A First-Principles Computational Approach," *J. Phys. Chem. B*, vol. 118, no. 19, pp. 5194–5202, 2014.

[133] K. R. Graham, P. M. Wieruszewski, R. Stalder, M. J. Hartel, J. Mei, F. So, and J. R. Reynolds, "Improved performance of molecular bulk-heterojunction photovoltaic cells through predictable selection of solvent additives," *Advanced Functional Materials*, vol. 22, no. 22, pp. 4801–4813, 2012.

[134] C. M. Hansen and A. L. Smith, "Using hansen solubility parameters to correlate solubility of c 60 fullerene in organic solvents and in polymers," *Carbon*, vol. 42, no. 8, pp. 1591–1597, 2004.

[135] F. Machui, S. Abbott, D. Waller, M. Koppe, and C. J. Brabec *Macromolec. Chem. Phys.*

[136] D. T. Duong, B. Walker, J. Lin, C. Kim, J. Love, B. Purushothaman, J. E. Anthony, and T.-Q. Nguyen *J. Polym. Sci. B Polym. Phys.*

[137] I. Burgues-Ceballos, F. Machui, J. Min, T. Ameri, M. M. Voigt, Y. N. Luponosov, S. A. Ponomarenko, P. D. Lacharmoise, M. Campoy-Quiles, and C. J. Brabec *Adv. Func. Mater.*

[138] B. Morgan and M. D. Dadmun, "The importance of solvent quality on the modification of conjugated polymer conformation and thermodynamics with illumination," *Soft Matter*, vol. 13, pp. 2773–2780, 2017.

[139] R. C. Burghardt and R. Droleskey, "Transmission electron microscopy," *Current protocols in microbiology*, pp. 2B–1, 2006.

[140] T. Gullion, "Rotational-echo, double-resonance nmr," in *Modern Magnetic Resonance*, pp. 713–718, Springer, 2008.

[141] J. C. Chan and H. Eckert, "Dipolar coupling information in multispin systems: application of a compensated redor nmr approach to inorganic phosphates," *Journal of Magnetic Resonance*, vol. 147, no. 2, pp. 170–178, 2000.

[142] S. Ganapathy, M. Fournier, J. Paul, L. Delevoye, M. Guelton, and J. Amoureux, "Location of protons in anhydrous keggin heteropolyacids h3pmo12o40 and h3pw12o40 by 1h {31P}/31p {1H} redor nmr and dft quantum chemical calculations," *Journal of the American Chemical Society*, vol. 124, no. 26, pp. 7821–7828, 2002.

[143] G. R. Marshall, D. D. Beusen, K. Kociolek, A. S. Redlinski, M. T. Leplawy, Y. Pan, and J. Schaefer, "Determination of a precise interatomic distance in a helical peptide by redor nmr," *Journal of the American Chemical Society*, vol. 112, no. 3, pp. 963–966, 1990.

[144] A. Naito, K. Nishimura, S. Tuzi, and H. Saito, "Inter-and intra-molecular contributions of neighboring dipolar pairs to the precise determination of interatomic distances in a simple [13c, 15n]-peptide by 13c, 15n-redor nmr spectroscopy," *Chemical physics letters*, vol. 229, no. 4-5, pp. 506–511, 1994.

[145] Y. Li, B. Poliks, L. Cegelski, M. Poliks, Z. Gryczynski, G. Piszczek, P. G. Jagtap, D. R. Studelska, D. G. Kingston, J. Schaefer, *et al.*, "Conformation of microtubule-bound paclitaxel determined by fluorescence spectroscopy and redor nmr," *Biochemistry*, vol. 39, no. 2, pp. 281–291, 2000.

[146] J. R. Garbow and C. A. McWherter, "Determination of the molecular conformation of melanostatin using carbon-13, nitrogen-15 redor nmr spectroscopy," *Journal of the American Chemical Society*, vol. 115, no. 1, pp. 238–244, 1993.

[147] R. C. Nieuwendaal, D. M. DeLongchamp, L. J. Richter, R. L. Jones, S. Engmann, *et al.*, "Characterization of interfacial structure in polymer-fullerene bulk heterojunctions via 13c 2h rotational echo double resonance nmr," *Physical Review Letters (In review)*.

[148] M. Bertmer and H. Eckert, "Dephasing of spin echoes by multiple heteronuclear dipolar interactions in rotational echo double resonance nmr experiments," *Solid State Nuclear Magnetic Resonance*, vol. 15, no. 3, pp. 139–152, 1999.

[149] E. Hughes, T. Gullion, A. Goldbourt, S. Vega, and A. J. Vega, "Internuclear distance determination of s= 1, i= 1/2 spin pairs using reapdor nmr," *Journal of Magnetic Resonance*, vol. 156, no. 2, pp. 230–241, 2002.

[150] J. L. Klepeis, K. Lindorff-Larsen, R. O. Dror, and D. E. Shaw, "Long-timescale molecular dynamics simulations of protein structure and function," *Current opinion in structural biology*, vol. 19, no. 2, pp. 120–127, 2009.

[151] L. C. Pierce, R. Salomon-Ferrer, C. Augusto F. de Oliveira, J. A. McCammon, and R. C. Walker, "Routine access to millisecond time scale events with accelerated molecular dynamics," *Journal of chemical theory and computation*, vol. 8, no. 9, pp. 2997–3002, 2012.

[152] J. D. Owens, D. Luebke, N. Govindaraju, M. Harris, J. Krüger, A. E. Lefohn, and T. J. Purcell, "A survey of general-purpose computation on graphics hardware," in *Computer graphics forum*, vol. 26, pp. 80–113, Wiley Online Library, 2007.

[153] J. D. Owens, M. Houston, D. Luebke, S. Green, J. E. Stone, and J. C. Phillips, "Gpu computing," *Proceedings of the IEEE*, vol. 96, no. 5, pp. 879–899, 2008.

[154] M. Harvey and G. De Fabritiis, "A survey of computational molecular science using graphics processing units," *Wiley Interdisciplinary Reviews: Computational Molecular Science*, vol. 2, no. 5, pp. 734–742, 2012.

[155] F. Wang, C.-Q. Yang, Y.-F. Du, J. Chen, H.-Z. Yi, and W.-X. Xu, "Optimizing linpack benchmark on gpu-accelerated petascale supercomputer," *Journal of Computer Science and Technology*, vol. 26, no. 5, p. 854, 2011.

[156] V. Volkov and J. W. Demmel, "Benchmarking gpus to tune dense linear algebra," in *High Performance Computing, Networking, Storage and Analysis, 2008. SC 2008. International Conference for*, pp. 1–11, IEEE, 2008.

[157] J. Bergstra, O. Breuleux, F. Bastien, P. Lamblin, R. Pascanu, G. Desjardins, J. Turian, D. Warde-Farley, and Y. Bengio, "Theano: A cpu and gpu math compiler in python," in *Proc. 9th Python in Science Conf*, vol. 1, 2010.

[158] W. M. Brown, P. Wang, S. J. Plimpton, and A. N. Tharrington, "Implementing molecular dynamics on hybrid high performance computers–short range forces," *Computer Physics Communications*, vol. 182, no. 4, pp. 898–911, 2011.

[159] S. Pall, M. J. Abraham, C. Kutzner, B. Hess, and E. Lindahl, "Tackling exascale software challenges in molecular dynamics simulations with gromacs," in *International Conference on Exascale Applications and Software*, pp. 3–27, Springer, 2014.

[160] J. C. Phillips, R. Braun, W. Wang, J. Gumbart, E. Tajkhorshid, E. Villa, C. Chipot, R. D. Skeel, L. Kale, and K. Schulten, "Scalable molecular dynamics with namd," *Journal of computational chemistry*, vol. 26, no. 16, pp. 1781–1802, 2005.

[161] J. A. Anderson, C. D. Lorenz, and A. Travesset, "General purpose molecular dynamics simulations fully implemented on graphics processing units," *Journal of Computational Physics*, vol. 227, no. 10, pp. 5342–5359, 2008.

[162] P. Eastman and V. S. Pande, "Efficient nonbonded interactions for molecular dynamics on a graphics processing unit," *Journal of computational chemistry*, vol. 31, no. 6, pp. 1268–1272, 2010.

[163] P. Eastman, M. S. Friedrichs, J. D. Chodera, R. J. Radmer, C. M. Bruns, J. P. Ku, K. A. Beauchamp, T. J. Lane, L.-P. Wang, D. Shukla, *et al.*, "Openmm 4: a reusable, extensible, hardware independent library for high performance molecular simulation," *Journal of chemical theory and computation*, vol. 9, no. 1, pp. 461–469, 2012.

[164] P. Eastman, J. Swails, J. D. Chodera, R. T. McGibbon, Y. Zhao, K. A. Beauchamp, L.-P. Wang, A. C. Simmonett, M. P. Harrigan, C. D. Stern, R. P. Wiewiora, B. R. Brooks, and V. S. Pande, "Openmm 7: Rapid development of high performance algorithms for molecular dynamics," *PLOS Computational Biology*, vol. 13, pp. 1–17, 07 2017.

[165] C. J. Tainter, L. Shi, and J. L. Skinner, "Reparametrized e3b (explicit three-body) water model using the tip4p/2005 model as a reference," *Journal of chemical theory and computation*, vol. 11, no. 5, pp. 2268–2277, 2015.

[166] M. Bonomi, D. Branduardi, G. Bussi, C. Camilloni, D. Provasi, P. Raiteri, D. Donadio, F. Marinelli, F. Pietrucci, R. A. Broglia, *et al.*, "Plumed: A portable plugin for free-energy calculations with molecular dynamics," *Computer Physics Communications*, vol. 180, no. 10, pp. 1961–1972, 2009.

[167] G. A. Tribello, M. Bonomi, D. Branduardi, C. Camilloni, and G. Bussi, "Plumed 2: New feathers for an old bird," *Computer Physics Communications*, vol. 185, no. 2, pp. 604–613, 2014.

[168] H. Sidky, Y. J. Colón, J. Helfferich, B. J. Sikora, C. Bezik, W. Chu, F. Giberti, A. Z. Guo, X. Jiang, J. Lequieu, *et al.*, "Ssages: Software suite for advanced general ensemble simulations," *The Journal of chemical physics*, vol. 148, no. 4, p. 044104, 2018.

[169] G. Fiorin, M. L. Klein, and J. Hénin, "Using collective variables to drive molecular dynamics simulations," *Molecular Physics*, vol. 111, no. 22-23, pp. 3345–3362, 2013.

[170] A. Martel, L. Antony, Y. Gerelli, L. Porcar, A. Fluitt, K. Hoffmann, I. Kiesel, M. Vivaudou, G. Fragneto, and J. J. De Pablo, "Membrane permeation versus amyloidogenicity: A multitechnique study of islet amyloid polypeptide interaction with model membranes," *Journal of the American Chemical Society*, vol. 139, no. 1, pp. 137–148, 2016.

[171] G. M. Torrie and J. P. Valleau, "Nonphysical sampling distributions in monte carlo free-energy estimation: Umbrella sampling," *Journal of Computational Physics*, vol. 23, no. 2, pp. 187–199, 1977.

[172] M. Souaille and B. Roux, "Extension to the weighted histogram analysis method: combining umbrella sampling with free energy calculations," *Computer physics communications*, vol. 135, no. 1, pp. 40–57, 2001.

[173] D. Marx, M. E. Tuckerman, and M. Parrinello, "Solvated excess protons in water: quantum effects on the hydration structure," *Journal of Physics: Condensed Matter*, vol. 12, no. 8A, p. A153, 2000.

[174] M. Wolfsberg, W. A. Hook, P. Paneth, and L. P. N. Rebelo, *Isotope Effects in the Chemical, Geological and Bio Sciences*. Springer Netherlands, 2009.

[175] Y. Cha, C. Murray, and J. Klinman, "Hydrogen tunneling in enzyme reactions," *Science*, vol. 243, no. 4896, pp. 1325–1330, 1989.

[176] M. Ceriotti, W. Fang, P. G. Kusalik, R. H. McKenzie, A. Michaelides, M. A. Morales, and T. E. Markland, "Nuclear quantum effects in water and aqueous systems: Experiment, theory, and current challenges," *Chemical Reviews*, vol. 116, no. 13, pp. 7529–7550, 2016. PMID: 27049513.

[177] X.-Z. Li, B. Walker, and A. Michaelides, "Quantum nature of the hydrogen bond," *Proceedings of the National Academy of Sciences*, 2011.

[178] J. Chen, X.-Z. Li, Q. Zhang, M. I. J. Probert, C. J. Pickard, R. J. Needs, A. Michaelides, and E. Wang, "Quantum simulation of low-temperature metallic liquid hydrogen," *Nature Communications*, vol. 4, pp. 2064 EP –, 06 2013.

[179] M. Ceriotti, J. Cuny, M. Parrinello, and D. E. Manolopoulos, "Nuclear quantum effects and hydrogen bond fluctuations in water," *Proceedings of the National Academy of Sciences*, vol. 110, no. 39, pp. 15591–15596, 2013.

[180] J. P. Klinman and A. Kohen, "Hydrogen tunneling links protein dynamics to enzyme catalysis," *Annual Review of Biochemistry*, vol. 82, no. 1, pp. 471–496, 2013. PMID: 23746260.

[181] Y. Cho, L. B. Sagle, S. Iimura, Y. Zhang, J. Kherb, A. Chilkoti, J. M. Scholtz, and P. S. Cremer, "Hydrogen bonding of -turn structure is stabilized in d2o," *Journal of the American Chemical Society*, vol. 131, no. 42, pp. 15188–15193, 2009. PMID: 19919159.

[182] M. A. Webb and T. F. Miller, III, "Position-specific and clumped stable isotope studies: Comparison of the urey and path-integral approaches for carbon dioxide, nitrous oxide, methane, and propane," *Journal of Physical Chemistry A*, vol. 118, no. 2, pp. 467–474, 2014.

[183] Y. Feng, J. Chen, D. Alfè, X.-Z. Li, and E. Wang, "Nuclear quantum effects on the high pressure melting of dense lithium," *The Journal of Chemical Physics*, vol. 142, no. 6, p. 064506, 2015.

[184] D. Chandler and P. G. Wolynes, "Exploiting the isomorphism between quantum theory and classical statistical mechanics of polyatomic fluids," *The Journal of Chemical Physics*, vol. 74, no. 7, pp. 4078–4095, 1981.

[185] R. P. Feynman and A. R. Hibbs, *Quantum Mechanics and Path Integrals*. McGraw-Hill Companies, 1965.

[186] J. Cao and G. A. Voth, "The formulation of quantum statistical mechanics based on the feynman path centroid density. ii. dynamical properties," *The Journal of Chemical Physics*, vol. 100, no. 7, pp. 5106–5117, 1994.

[187] S. Jang and G. A. Voth, "A derivation of centroid molecular dynamics and other approximate time evolution methods for path integral centroid variables," *The Journal of Chemical Physics*, vol. 111, no. 6, pp. 2371–2384, 1999.

[188] I. R. Craig and D. E. Manolopoulos, "Quantum statistics and classical mechanics: Real time correlation functions from ring polymer molecular dynamics," *The Journal of Chemical Physics*, vol. 121, no. 8, pp. 3368–3373, 2004.

[189] S. Habershon, D. E. Manolopoulos, T. E. Markland, and T. F. Miller, III, "Ring-Polymer Molecular Dynamics: Quantum Effects in Chemical Dynamics from Classical Trajectories in an Extended Phase Space," in *ANNUAL REVIEW OF PHYSICAL CHEMISTRY, VOL 64* (Johnson, MA and Martinez, TJ, ed.), vol. 64 of *Annual Review of Physical Chemistry*, pp. 387–413, 2013.

[190] T. E. Markland and M. Ceriotti, "Nuclear quantum effects enter the mainstream," *Nature Reviews Chemistry*, vol. 2, MAR 2018.

[191] R. P. Steele, J. Zwickl, P. Shushkov, and J. C. Tully, "Mixed time slicing in path integral simulations," *The Journal of Chemical Physics*, vol. 134, no. 7, p. 074112, 2011.

[192] M. Ceriotti, M. Parrinello, T. E. Markland, and D. E. Manolopoulos, "Efficient stochastic thermostatting of path integral molecular dynamics," *The Journal of Chemical Physics*, vol. 133, no. 12, p. 124104, 2010.

[193] T. E. Markland and D. E. Manolopoulos, "An efficient ring polymer contraction scheme for imaginary time path integral simulations," *The Journal of Chemical Physics*, vol. 129, no. 2, p. 024105, 2008.

[194] T. E. Markland and D. E. Manolopoulos, "A refined ring polymer contraction scheme for systems with electrostatic interactions," *Chemical Physics Letters*, vol. 464, no. 4, pp. 256 – 261, 2008.

[195] M. Ceriotti, D. E. Manolopoulos, and M. Parrinello, "Accelerating the convergence of path integral dynamics with a generalized langevin equation," *The Journal of Chemical Physics*, vol. 134, no. 8, p. 084104, 2011.

[196] V. Kapil, J. Behler, and M. Ceriotti, "High order path integrals made easy," *The Journal of Chemical Physics*, vol. 145, no. 23, p. 234103, 2016.

[197] M. Ceriotti, J. More, and D. E. Manolopoulos, "i-pi: A python interface for ab initio path integral molecular dynamics simulations," *Computer Physics Communications*, vol. 185, no. 3, pp. 1019 – 1026, 2014.

[198] O. Guvench, S. S. Mallajosyula, E. P. Raman, E. Hatcher, K. Vanommeslaeghe, T. J. Foster, F. W. Jamison, and A. D. MacKerell, "Charmm additive all-atom force field for carbohydrate derivatives and its utility in polysaccharide and carbohydrate–protein modeling," *Journal of Chemical Theory and Computation*, vol. 7, no. 10, pp. 3162–3180, 2011. PMID: 22125473.

[199] S. Habershon, T. E. Markland, and D. E. Manolopoulos, "Competing quantum effects in the dynamics of a flexible water model," *The Journal of Chemical Physics*, vol. 131, no. 2, p. 024501, 2009.

[200] T. E. Markland, "web.stanford.edu/group/markland/software.html."